PERFORMANCE OF NOVEL DIGITAL HADRON CALORIMETER USING GAS ELECTRON MULTIPLIER (GEM) AND THE ENERGY FLOW ALGORITHM DEVELOPMENT

The members of the Committee approve the master's thesis of Venkatesh Kaushik

Jaehoon Yu
Supervising Professor _____

Kaushik De _____

Andrew Brandt _____

Alexander Weiss _____

PERFORMANCE OF NOVEL DIGITAL HADRON CALORIMETER USING GAS ELECTRON MULTIPLIER (GEM) AND THE ENERGY FLOW ALGORITHM DEVELOPMENT

by

VENKATESH KAUSHIK

Presented to the Faculty of the Graduate School of

The University of Texas at Arlington in Partial Fulfillment

of the Requirements for the Degree of

MASTER OF SCIENCE IN PHYSICS

THE UNIVERSITY OF TEXAS AT ARLINGTON

May 2004

ACKNOWLEDGEMENTS

Working with Dr. Jaehoon Yu, who is my thesis advisor has been a distinct honor and rewarding experience for me in many ways. I have learnt the rigors of doing collaborative research, the value of timeliness of research deliverables, and have had many illuminating discussions with him over two years of doing research under him. He emphasized on enthusiasm for quality research work, orderly presentation of research work for the common benefit of audience and the community. I also learnt the innards of healthy student-advisor communication, and gained confidence in giving talks at various levels since I was given many opportunities. To learn from one's own mistakes and that of others is common to research of any kind and I would like to thank him for correcting mistakes by being a guide and relentlessly stressing the need for a good student advisor relationship.

Our weekly GEM detector group meetings with Dr. Jaehoon Yu, Dr. Andrew White, Dr. Jia Li and Dr. Andrew Brandt, were very essential and proved to be invaluable, since we checked our progress on a weekly basis as they offered ways to improve results, suggested a change of approach where it was needed and verified the results.

I also had many discussions on a personal level with Dr. Mark Sosebee who is tremendously knowledgeable and proficient in calorimetry and providing useful hints and suggestions on the algorithm development and for sanity checks from time to time.

Dr. Sosebee was always available to help me out by fixing unforeseen problems with software/hardware to carry out research in a timely manner.

I would like to thank Dr. Kaushik De in particular for believing in me and encouraging me constantly in times of stress and help me grow up to his expectations and those of his peers. I would also like to thank Dr. Alex Weiss for agreeing to be on my graduate committee and for his inquisitive questions and valuable suggestions.

It would not have been possible for me to write this thesis without the help of many friends and colleagues. In particular, I would like to thank Dr. Chang-Hi Hahn, Barry Spurlock, Shahnoor Habib, Jeremy Johnson and Jacob Smith for proof reading the thesis document and for their valuable suggestions on the content and grammar. Barry was kind enough to let me refer books from his library and also to offered help with his critical observation of my research from time to time.

Last, but not the least, I would like to thank my family – my parents (Mr. Srinivasa Murthy and Mrs. Laxmi Murthy), my brother (Srikanth) and my fiancée (Daria) for all their support and encouragement.

April 29, 2004

ABSTRACT

PERFORMANCE OF NOVEL DIGITAL HADRON CALORIMETER USING GAS ELECTRON MULTIPLIER (GEM) AND THE ENERGY FLOW ALGORITHM DEVELOPMENT

Publication No. _____

Venkatesh Kaushik, MS (Physics)

The University of Texas at Arlington, 2004

Supervising Professor: Jaehoon Yu

The physics goals at a future linear particle collider demand high particle cluster (called the particle jet) energy resolution. Digital hadron calorimetry holds significant promise for achieving the excellent energy resolution required at a linear collider, while containing subsystem costs at a manageable level. The use of Gas Electron Multipliers (GEM) in the sensitive gap of a Digital Hadron Calorimeter is being explored by UTA High Energy Physics group. Using an unprecedented small size of calorimeter cells of $1\times1\text{cm}^2$ area, it is possible to track charged particles in the calorimeter and associate energy depositions with the corresponding tracks measured in the tracking system. After removal of this “charged energy”, the remaining neutral energy is measured using the

digital information from the neutral clusters (those without associated incoming charged track). This can be achieved by the use of the Energy Flow Algorithm (EFA). The success of EFA depends significantly on higher granularity of hadronic calorimeters. The higher granularity requires large number of readout channels that could potentially drive the cost of such a calorimeter prohibitively high. The use of GEM as a sensitive detector is a solution to keep the cost of such a calorimeter reasonable.

Simulation studies were carried out to determine the performance of the GEM hadron calorimeter in the analog mode [46] by Ms. Shahnoor Habib previously. We present the results from performance studies of the calorimeter in digital and analog techniques, using simulated data. The analog performance study is complimentary to the earlier study and differs from the earlier approach in improved statistics for simulated data and a use of systematic errors to measure calorimeter performance. In addition, the calorimeter performances in the digital mode is also carried out with and without threshold applied and results are discussed in this thesis. We also present preliminary results from Energy Flow Algorithm development.

TABLE OF CONTENTS

LIST OF ILLUSTRATIONS

LIST OF TABLES

CHAPTER 1

INTRODUCTION

1.1 Introduction to the Thesis

This thesis is a continuation from the previous study [46] undertaken to evaluate the performance of a hadron calorimeter in digital and analog modes. The earlier study aimed at the performance study in the analog mode. The present study improves on the analog performance and a new study is carried out to evaluate the calorimeter performance in digital mode with and without the threshold applied. A preliminary Energy Flow Algorithm is also developed and the study results are presented.

1.2 The Standard Model

High energy physics is the study of the fundamental constituents of matter and the nature of the interactions between them. The high energy physics community has arrived at a picture of the microscopic physical universe, called "The Standard Model," [1] which provides a theoretical framework for these fundamental building blocks of the universe. The fundamental particles in Standard Model are listed, arranged by electric charge and by mass in Table 1.1.

Table 1.1 Constituents of matter - quarks and leptons and their corresponding neutrinos

QUARKS			
electric charge	lightest (I)	heavier (II)	heaviest (III)
+2/3 e -1/3 e	up (*u*) down (*d*)	charm (*c*) strange (*s*)	top (*t*) bottom (*b*)
LEPTONS			
electric charge	lightest (I)	heavier (II)	heaviest (III)
-1 e 0 e	electron (*e*) *e*-neutrino (ν_e)	muon (μ) μ-neutrino (ν_μ)	tau (τ) τ-neutrino (ν_τ)

According to the theory of the Standard Model, there are two general classes of particles: 1) the fundamental fermions with half-integer spin[1] ($\frac{1}{2}\hbar, \frac{3}{2}\hbar, \frac{5}{2}\hbar$ etc.) and the gauge bosons with integer spin ($0, \hbar, 2\hbar, 3\hbar$ etc.) where $\hbar$ is the modified Plank's constant[2]. Fermions obey the Pauli exclusion principle and the Fermi-Dirac [2] statistics and make up what is usually considered "matter". They are further subdivided into two types of particles, the quarks and the leptons. Leptons exist singly and can have either electric charge 0 or ±e, where e, the unit electric charge is 1.6×10^{-19} Coulombs. At present there is no evidence for substructure in leptons, and hence they are regarded as point-like objects. Quarks, by contrast, are always observed in combination with other quarks in hadronic matter. Unlike leptons, quarks possess fractional electric charge and are distinct in that they possess an internal degree of freedom called color, which can take on three possible values. Antimatter is also observed, made up of antiparticles (antileptons and antiquarks).

[1] Quantum number associated with one of the components of the angular momentum of the particle.
[2] The constant of proportionality relating the energy (E) of a photon to its frequency (ν) E=hν;h = 6.626 x 10^{-34} Js. $\hbar$ = h/2π

An antiparticle shares many of its characteristics with its particle counterpart, but when it differs, it has the opposite property. For example, the electron and antielectron (or the positron) are antiparticles; they have the same mass, but opposite electric charge. The twelve antiparticles are not listed in Table 1.1. The nucleons (protons and neutrons) are the most common hadrons. Two types of quark (q) combination constitute hadrons:

Baryons with three quarks (qqq)

Mesons with a quark anti-quark pair ($q\bar{q}$)

Examples of mesons are the pions, ($\pi^{\pm}$ with $u\bar{d}$ and $d\bar{u}$ quark pairs respectively) and the kaons ($K^{\pm}$, with $u\bar{s}$ and $s\bar{u}$ quark pairs respectively) among others. The most common baryons are the proton (*uud*) and the neutron (*udd*), which are collectively called nucleons.

Physicists have recognized four fundamental forces: gravity, electromagnetism, the weak force, and the strong force. They have also discovered that the rules that describe the everyday phenomena, known as the classical physics, fails to describe interactions involving one, two, or a few elementary particles. A new set of theories known as quantum theories was developed in the early 1920's and continues to be the basis of our understanding of the fundamental forces. At the quantum level, the forces are transmitted through the exchange of the intermediate particles. One particle exerts a force on the other by emitting one of these intermediate carriers, which is then absorbed

by the other particle. Each force is unique in its carrier and in the rules for which exchanges are allowed or forbidden.

Gravity is a well-known force, which was described by Galileo and Newton in the seventeenth century but its role in the interaction of elementary particles is negligible because the force is proportional to the masses of the interacting particles, which are very small (nearly zero) implying small forces even at the small relative distance between them. Electromagnetism, the union of electricity and magnetism in classical physics, is also a familiar force. Maxwell described this force very well in the nineteenth century. The quantum theory, Quantum electrodynamics (QED) was developed in the 1940's and has been tested to extremely high precision. All electrically charged particles participate in electromagnetic interaction mediated by the exchange of photons. The strength of this force is proportional to the charges on both interacting particles and follows the inverse square law.

The weak force is responsible for most radioactive decays and for all neutrino interactions. The earliest description of this force was by Fermi in 1934 who explained the interactions by a four-particle contact force [3]. Weinberg, Salaam and Glashow developed the electroweak gauge theory in 1967-68, which not only explained the weak interaction but also unified it with electromagnetism [4]. This theory predicted the existence of a neutral channel of weak interactions in addition to the charged current channel. The subsequent observation of neutral currents [5, 6] and the observation of the intermediate vector bosons for both these channels was the ultimate triumph of this theory [7, 8, 9, 10].

The strong force is the force, which holds the quarks that make up the nucleons. Quantum Chromodynamics (QCD), the theory of strong interactions, is a gauge theory similar to QED, but differs in the self-coupling of its force carrier, the gluon. This property leads to a force whose strength grows with increasing distances up to the scale of the size of a nucleus. This prevents the observation of single, free quarks outside of the nucleon. One can observe the quarks inside the nucleon only with a high energy probe. Table 1.2 summarizes the four forces in the order of their strengths. The Standard Model combines these two gauge theories[3] of particle physics into a single framework to describe all interactions of subatomic particles, except those involving gravity.

Table 1.2 The Fundamental forces and their relative strengths

Force	Relative Strength	Intermediate Bosons
strong	1	gluons (g)
electromagnetism	1/137	photon (γ)
weak	10^{-5}	$W^{\pm}$, Z^0
gravity	10^{-40}	[graviton] (G)?]

1.3 Particle Accelerators

Experimental research in high energy physics is carried out primarily with high energy particle accelerators [11] and the associated detection apparatus. Particle accelerators are devices used to accelerate charged particles or ions to extremely high energies. These machines accelerate charged particles, eventually colliding a beam of these particles with a stationary target (fixed target experiment) or another particle beam

[3] QED and the QCD gauge theories.

(collider experiment). Both hadron-hadron and electron-positron colliders are used as important probing instruments.

The design of accelerators varies greatly depending on the purpose for which they will be used. Accelerators can be loosely classified as low, medium and high energy. Low-energy accelerators are used to produce beams in the 10–100 MeV range, often for scattering studies. Medium-energy accelerators operate in the range 100–1000 MeV. High-energy accelerators produce beams of 1 GeV (1000 MeV) and above. Higher energies are required to probe deeper into the structure of particles and for the production[4] of particles. The spatial resolution that can be achieved by studying the scattering of one particle off another at a given energy is limited by the de-Broglie wavelength λ of their relative motion: $\lambda = 2\pi/k$ where k is their relative momentum. To probe small distances requires large k values, which imply high energy in the center-of-mass frame. Some of the high-energy accelerators include the Tevatron (FNAL, at Batavia, Illinois), SLAC Linear Collider (SLC) at Stanford and Large Electron Positron collider (LEP) at CERN, Switzerland. Existing particle physics experiments can be classified into two groups: fixed target experiments and collider experiments. The SLC is a linear accelerator (or linac) and the Tevatron is a circular accelerator. The schematic diagram and aerial view of the Fermilab Tevatron are shown in Figs. 1.2 (a) and (b) respectively.

[4] Particles are produced when there is sufficient energy available in the center-of-mass frame of collision.

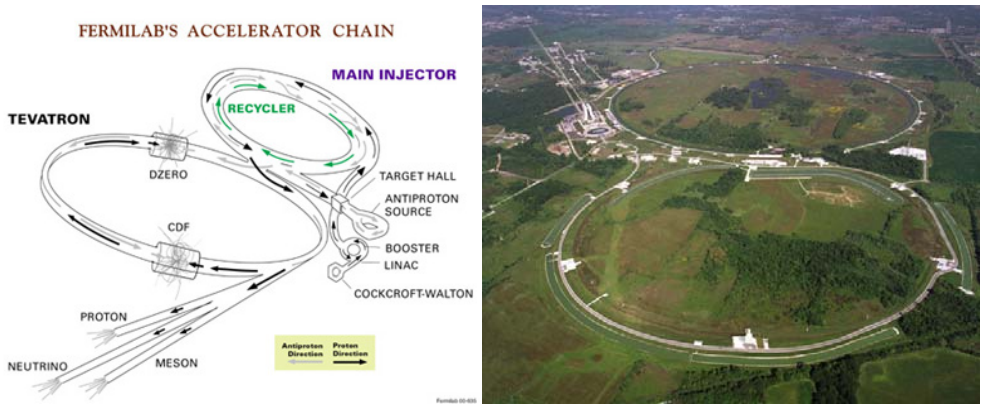

Fig. 1.1 (a) Schematic diagram of the Fermilab Tevatron (b) Aerial view of the accelerator facility. Courtesy of FNAL public pages [12]

1.3.1 Linear Colliders

Physicists believe that major discoveries expanding the standard model paradigm will occur at the next generation of accelerators. The Linear Collider (LC) is one such accelerator that will extend discoveries which can potentially be made at the Large Hadron Collider (LHC, at CERN that is currently being built) and provide a wealth of measurements that are essential for giving deeper understanding of their meaning [13]. Electrons and positrons are thought to be fundamental particles. Accelerating electrons in a circular ring will require large radius due to their high synchrotron radiation. An e^+e^- LC can virtually eliminate this radiation, allowing high acceleration. Experiments over the past two decades using accelerators at CERN, SLAC and Fermilab discovered the W and Z bosons, demonstrated their close connection to the photon, and firmly established the unified electroweak interaction. The LC is capable of precision measurements that are crucial for revealing the character of the Higgs boson associated with the electroweak symmetry breaking mechanism [14].

These measurements, together with new very precise studies of the W and Z bosons and the top quark are possible at the LC.

1.4 Particle Detectors

The detection and identification of elementary particles and nuclei is of primary importance in high energy physics. The basic idea of particle detection is to use the outcomes resulting from the interactions of particles and radiation in matter as a guiding principle or an idea to build a detector. The aim of detection is to reconstruct "events" and study the data that are obtained from them. The properties of a particle are unique and distinguish it from other particles in the way it is affected by the fundamental interactions. These properties include charge, mass, spin, lifetime, decay, branching ratios[5] and magnetic moment. Identification involves the determination of these properties.

Detectors typically are placed downstream of a fixed target or surrounding the collision point of colliding beams. Detection of particles depends on the transfer of energy in the medium they traverse via the ionization and excitation of constituent atoms. The interaction usually creates an analog signal of some kind, which is measured or converted into standardized pulses using electronics. The detector system required for most experiments include:

Tracking chambers

Muon Spectrometer

Calorimeters

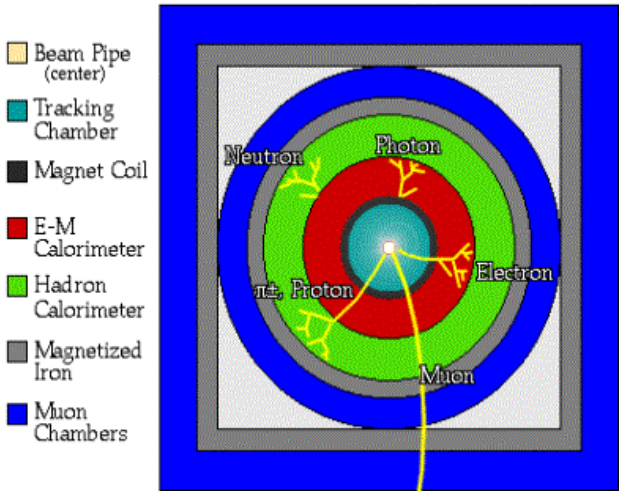

Fig. 1.2 Schematic diagram a of detector cross-section showing particle paths

Tracking involves the determination of trajectories of particles by measuring the spatial location of interactions along with intrinsic time of interaction between the particle and the detector. Muon identification is possible because muons are the only charged particles that can penetrate large amounts of material. Muons, due to their large mass relative to the electron, interact negligibly in the material. The method for detecting muons is to place charged particle detectors behind a large amount of shielding material. The schematic diagram of a typical detector is shown in Fig. 1.2. The particle paths through the detector are also illustrated for various particles.

[5] The ratio of the probability of decay of a particle by a given mode to the probability of decay by any mode

1.5 Thesis Outline

Powerful simulation tools exist for generation of high energy physics events, i.e. for the description of collisions at high energies between elementary particles such as e^+e^-, $p\bar{p}$ in various combinations and to study the passage of particles through matter. Analysis is done on the data that is obtained from simulation. These simulation tools are explained in Chapter 2. Chapter 3 is organized into two sections. One section deals with calorimetry in greater detail, especially with hadron calorimetry, which is important in understanding the Energy Flow Algorithm (EFA). EFA for a digital hadron calorimeter is currently under development and the principles of EFA are explained in the next section. The study of single particles is important to understand the behavior of the detector and energy response and resolution of calorimeter. The performance study using charged pions as single particles are presented in Chapter 4 for the analog mode and Chapter 5 for the digital mode. The algorithm development effort for jet energy resolution is explained in Chapter 6 followed by Conclusions in Chapter 7.

CHAPTER 2

SIMULATION TOOLS

2.1 Monte Carlo Simulation

Monte Carlo (MC) methods are a type of numerical calculation [15]. They can be described as statistical simulations utilizing sequences of random numbers to perform the simulation. MC techniques are used extensively in high energy physics experiments, where experimental data describing the physics of the interactions and their expected behavior in the detector are modeled and studied. Some of the tools used in the simulations are event generators (e.g., Pythia [16]), and simulation of passage of particles through detectors by describing their geometry, material composition and response, (e.g., GEANT [17]). Tools are also available for visualization of events (e.g., GEANT, WIRED [18], DAWN [19] etc.), and for data analysis and histograming (e.g., ROOT [20], JAS [21]), which are described in subsequent sections of this chapter.

2.2 Event Generators

Event generators are software packages used to simulate high energy physics interactions. An event is a set of outgoing particles produced in interactions between two incoming particle beams. The behavior of particles in a physical process can be simulated in event generators by the use of MC techniques. The output of an event generator should have the similar average behavior and statistical fluctuations as the

actual data resulting from colliding particle beams. The primary objective of an event generator is to generate events as similar in detail as possible to those observed in the actual detector. The other objective is to provide an accurate representation of event properties for a wide range of interactions, based on a specific physical model, for example, QCD. Various models are put forth to describe the physics processes. To the first approximation, all physics processes have a simple structure at the level of interactions between the fundamental particles, i.e., quarks, leptons and the gauge bosons. For example, a simple skeleton process like the electron-positron interaction indicated in Eq. 2.1 helps us understand the structure of hadronic events:

$$e^+e^- \rightarrow \quad Z^0 \rightarrow \quad q\bar{q} \tag{2.1.}$$

To describe the process and to identify the final state particles, starting from the simple skeleton process of Eq. 2.1 is considerably more complex. The accurate representation of these processes is one of the goals of the event generator. Some corrections are necessary for this simple picture, such as bremsstrahlung i.e., the emission of additional final state particles via the reaction given by Eq. 2.2.

$$e \rightarrow e\gamma \; or \; q \rightarrow qg \tag{2.2.}$$

Higher order corrections are needed to cancel some divergences. For the quarks and gluons, in addition to the short distance interactions, one must describe the structure of the incoming hadrons and the hadronization process of the final state partons, wherein the colored partons are transformed into jets of colorless hadrons, photons, and

leptons. The hadronization can be further divided into fragmentation[6] and decays. So the event generation is based on available collider related issues, analytical results and various QCD based models to describe strong interactions. The hard process is used as input to generate bremsstrahlung corrections and the result of this exercise is left to hadronize.

2.2.1 Event Generators for Linear Colliders

Experiments at linear colliders pose special problems for event generation. In addition to the problems of generating parton-level events and then making the transition to the hadron level, other features of the physics should be taken into account. Electron, and the positron beams at linear colliders can be polarized, and the polarization-dependence is an extremely useful tool in experiments. Since detectors for e^+e^- colliders typically see all final jets and leptons, spin correlations in the final states can be measured, and these also contain valuable information. For many of the processes of interest in linear collider physics, it is possible to obtain the full set of these effects by combining a number of available simulation programs:

- CIRCE [22] for beam effects,
- Pythia [16] or HERWIG [23] for the core processes and hadronization,
- TAUOLA [24] to treat special cases such as τ decays.

[6] Fragmentation is the term used to describe the way the creation of quark-antiquark pairs can breakup a high-mass system into a lower-mass system.

2.2.2 Pythia Event Generator and the Pandora Interface

Pandora-pythia is one such package that combines the available simulation programs transparently into a single package [25]. This program provides a simple, unified framework for event generation for future linear colliders. Using this package, it is possible to produce event samples for the basic processes of linear collider physics taking full account of beam and polarization effects. Beam and parton-scattering cross sections are used to produce parton-level events, passing the results to PYTHIA and TAUOLA to create the final state particles through fragmentation and hadronization mechanism. The program has an intrinsic modular structure. It is easy to modify the parton-level physics or even to include new processes.

2.2.3 Output format of Pandora-pythia

The currently available event generation packages (including the ones listed in section 2.2.1) were written primarily in FORTRAN and each supports different output format. The need to accommodate such packages with the modern detector simulation programs written in C++, led the high energy physics community to develop a common standard for events called the HEPEvt [26] standard. The default output format for Pandora-pythia is a HEPEvt binary file [28]. The GEANT detector simulation package provides the ASCII interface to accommodate the output of these event generators interfaced to Pandora-pythia [27]. It is possible modify the Pandora-pythia program, to take advantage of this ASCII file interface. This ASCII interface enables the user to choose GEANT (also referred to as Geant4 subsequently) for detector simulation. For this thesis, the modification of Pandora-pythia was implemented to convert the output

from HEPEvt binary format to HEPEvt ASCII format. Refer to Appendix A for more detailed information on the quantities listed in HEPEvt common block and subroutine used thereof.

2.3 Detector Simulation

2.3.1 Geant4

Geant4 is a freely available software package composed of tools that can be used to accurately simulate the passage of particles through matter. All aspects of the simulation process have been included in the toolkit such as:

- the geometry of the system and the materials involved
- the fundamental particles of interest
- the tracking of particles through materials and electromagnetic fields
- the physics processes governing particle interactions
- the response of sensitive detector components, the generation of event data
- the storage of events and tracks, the visualization of the detector and particle trajectories

Geant4 based full detector simulation is used in this analysis. The end user runs the simulation program by controlling run time parameters input through command lines and/or macros. For this analysis, a readily available application toolkit, called the Mokka [29] is used, which is described in the section 2.3.2.

2.3.2 Mokka Interface to Geant4

Mokka [29] is a complete toolkit for linear collider detector simulation using the Geant4 package with an interactive command line interface and the macro-based system for batch processing. It provides a detailed description of the detector geometry for a future linear collider. The basic model is proposed for the TESLA [30] project, and is described in detail in the TESLA Technical Design Report (TDR) [31]. Mokka is geometry data driven and enables the user to simulate several detector or prototype models from its geometry database. Mokka simulates in detail the TESLA Electromagnetic calorimeter (Ecal), the hadronic calorimeter (Hcal), and other detector components such as the Vertex Detector (VXD), the Silicon Intermediate Tracker (SIT), the Forward Tracking Disks (FTD), the Time Projection Chamber (TPC) and Forward Tracking Chamber (FCH), Coil and Yoke (primarily dead material), and implementation of a magnetic field inside the solenoid zone and in the barrel yoke proposed in the TESLA TDR detector. Several modifications to the existing geometry definition of the hadronic calorimeter are implemented in this thesis. The modifications of the geometry relevant to the current simulation study are described in Chapter 4.

2.4 Analysis Tools

2.4.1 ROOT

ROOT [20] is an objected oriented framework[7] that was developed to meet the challenges of present day analyses in High Energy Physics. The ROOT system provides a set of Object Oriented frameworks with all the functionality needed to handle and analyze large amounts of data in a very efficient manner. Figure 2.1 illustrates the basic idea of such a framework. Data is defined as a set of objects; specialized storage methods are used to provide direct access to the various attributes of the selected objects, without having to analyze the bulk of the data.

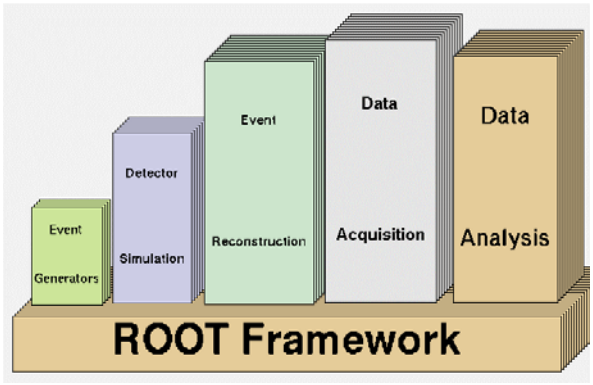

Fig. 2.1 ROOT Framework

Histograming methods in one, two and three dimensions, curve fitting, function evaluation, minimization, graphics and visualization classes allow the straightforward setup of an analysis system. This framework can query and process the data interactively or in batch mode. ROOT is used as the primary analysis tool for this thesis.

[7] A term used in software engineering to describe basic utilities and services like I/O, graphics, and also histogram and fitting routines, in the case of ROOT.

2.4.2 Java Analysis Studio (JAS)

Java Analysis Studio [21] includes a rich set of classes for filling and operating on histograms, as part of the High Energy Physics analysis package. These classes have been carefully designed for ease of use, while at the same time providing a host of capabilities for advanced users as well as allowing users to extend the built-in functionality by writing their own Java classes that inherit from the built-in classes. The classes facilitate the creation and filling of histograms. In the current version of Java Analysis Studio display of histograms as well as fitting is done using a Graphical User Interface (GUI). This tool is used wherever relevant and is not a primary tool for analysis in the thesis.

CHAPTER 3

CALORIMETRY AND ENERGY FLOW TECHNIQUE

3.1 Calorimetry

3.1.1 Introduction to Calorimetry

The term calorimetry, in nuclear and particle physics refers to the detection of particles and measurement of their properties, through total absorption in a block of matter, called a calorimeter. The common feature of all calorimeters is the measurement of the particle properties through a destructive technique. As a result of this technique the particle is no longer available for inspection by other devices after it passes through the calorimeter. The only exceptions to this rule are the muons and neutrinos, which can penetrate substantial amounts of matter in the calorimeter without being destroyed. In the process of absorption, all of the particle's energy is converted into heat, hence the term calorimetry. The units of energy in this process are very different from the thermodynamic ones. For example, some of the most energetic particles in the modern accelerator experiments are measured in units of TeV (1 TeV = 10^{12} eV $\approx 40.\ 10^{-9}$ calorie). The rise in temperature of the block that absorbs the particle is practically negligible. Sophisticated methods in calorimetry are therefore needed to identify the particles and measure their properties. Some of the important aspects of calorimetry that are used in this thesis are introduced in the subsequent sections.

3.2 Energy Response of Calorimeters

The Energy Response of a calorimeter is defined as the ratio of average energy deposit measured as an electrical signal in the calorimeter to the energy of the particle that caused it. For example, if a calorimeter measures the energy of electrons, the average signal for the detection of electrons is proportional to the electron energy. The calorimeter response increases linearly as a function of the incident particle energy. Such a calorimeter is said to be linear for detection of that particle. Linearity of a calorimeter response is an important property of the device.

3.2.1 Sampling Calorimeters

In a sampling calorimeter, the particle absorption and signal generation take place in different materials called the passive and active medium, respectively. The passive medium is generally a high-density material such as iron, lead, or uranium that causes the particle to interact. The active medium measures the deposited energy in the form of light or electrical charge, which forms the basis for the signals from such a calorimeter.

A few typical examples of Sampling Calorimeters and their active material are given in Fig. 3.1. In a total absorption calorimeter, as opposed to sampling calorimeters, the entire detector volume is sensitive to the particles and contributes to the signal it generates.

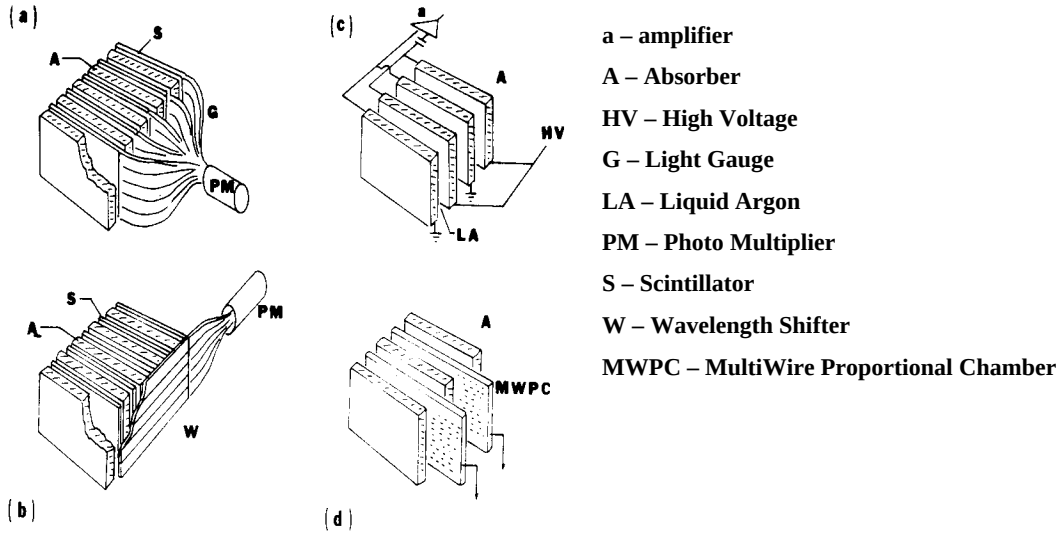

Fig. 3.1. Active and Passive Layers in a Sampling Calorimeter. (a) Lead-scintillator sandwich (b) lead-scintillator sandwich with wavelength shifter bars (c) Liquid Argon ionization chamber and (d) lead-MWPC sandwich [32]

Since this thesis is based on the simulation of a sampling calorimeter, the discussion is limited to sampling calorimeters in the current and subsequent chapters. The calorimeter response can be broadly classified into electromagnetic (EM) response and the response to hadrons (or hadronic response). The response of a calorimeter to electrons and photons is different from that due to hadrons. The response to muons also differs considerably from the EM or hadronic response, since its interaction with the material of the detector is minimal.

3.2.2 Response to Minimum Ionizing Particles (mips)

The term minimum ionizing particle (mip) is used in calorimetry to describe particles that traverse the medium of the calorimeter material with minimum loss in ionization energy. The energy loss of a particle (whether it is electromagnetic or hadronic) is primarily due to the ionization of atoms in the medium due to the passage of the particle. Muons behave like mips at energies below 100 GeV, and the mean energy loss in the detector material is ionization for all absorber materials. For muons with energies above 100 GeV, the average amount of energy loss in the calorimeter increases with energy [33]. The mean energy loss of charged particles per unit length $\langle dE/dx \rangle$ in a medium is described by the Bethe-Bloch formula [34]

$$-\langle dE/dx \rangle = Kz^2 \frac{Z}{A}\frac{1}{\beta^2}\left\{\frac{1}{2}\ln\frac{2m_e c^2\beta^2\gamma^2 T_{\max}}{I^2} - \beta^2 - \frac{\delta}{2}\right\} \qquad 3.1.$$

The quantity $\langle dE/dx \rangle$ is called the stopping power (or specific ionization). The specific ionization has an energy dependence, which is governed by the product of the velocity (β) and Lorentz factor (γ) of the particles as shown in Eq. 3.1. T_{max} represents the maximum kinetic energy that can be imparted to an electron in a single collision, *I* is the mean excitation energy of the absorber material and δ is a correction term describing the *density effect* [34], and the proportionality constant *K* equals $4\pi N_A r_e^2 m_e c^2$. For relativistic muons, $\langle dE/dx \rangle$ falls rapidly with increasing β, reaches a

minimum at $\beta = 0.96$ and then undergoes a relativistic rise to level off at values of 1-2 MeV cm^2/g [34]. Muons cause the absorber material to lose energetic knock-on electrons (δ rays), which are responsible for this relativistic rise. For this reason, it takes substantial amounts of material to absorb high energy muons. Therefore muons (or other charged particles) with an energy corresponding to a value, at which the $\langle dE/dx \rangle$ curve reaches a minimum, are called minimum ionizing particles (mips). The stopping power as a function of the muon momentum for various media is shown in Fig. 3.2.

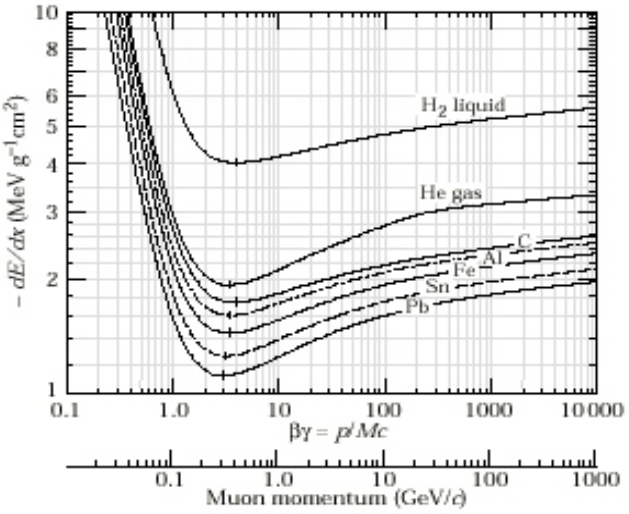

Fig. 3.2 Plot of the stopping power as a function of the muon momentum for various materials.

3.2.3 Electromagnetic Response

Because of the similarity between the energy deposit mechanisms, the responses to mips and EM showers are similar. This is expressed as e/mip, where e and mip

denote the calorimeter responses to EM showers and mips respectively. For a homogeneous calorimeter e/mip = 1 [35], except for minor deviations due to shower fluctuations. For a sampling calorimeter, however, e/mip is less than 1 and this value is also material dependent. In high-density materials (uranium, Z=92; lead, Z=82; tungsten, Z=74 etc.), the signal from an electron or photon absorbed in the sampling calorimeter is the ionization or excitation of the active layers by all shower electrons and positrons that traverse these layers [36, 37, 38 39]. In high Z absorber materials, however a significant amount of energy is carried by low-energy photons ($E_\gamma < 1$ MeV) that have a short range in the sampling layers, thus suppressing the energy response. This effect is called the transition effect [39]. The soft γs responsible for the suppression of the EM calorimeter response in high-Z sampling calorimeters interact overwhelmingly in the absorber layers. The γs produced in these interactions only contribute to the calorimeter signal if the interaction occurs in a thin region, with an effective thickness δ, near the boundary between the active and passive layers. To increase the fraction of shower γs that interact in the δ region, the sampling frequency[8] can be increased. By making the absorber layers thinner, the transition effects can be overcome and the e/mip ratio can be improved to have values closer to 1 [40].

[8] A term used to denote the number of active layers per radiation length of a sampling calorimeter.

3.2.4 Response to Hadrons

When a high energy hadron penetrates the layers of a sampling calorimeter, the hadron may lose energy either by ionizing the medium, or undergoing nuclear interactions. When the hadron is charged, its energy loss through the medium is much like a muon of the same energy. However, the charged hadron may encounter and interact strongly with an atomic nucleus in its depth. Nuclear interactions cause the hadron to change its identity dramatically. For example, several hadrons may be produced due to such an interaction along with neutrons and protons produced from the struck nucleus, which may decay by emitting γ rays. Neutral hadrons do not ionize the traversed medium, and lose energy primarily through nuclear interactions.

At lower energies, well below 1GeV, the hadrons lose energy by ionizing the medium, like mips [41]. As the energy of the incident hadron increases, nuclear interactions are much more prominent with the production of π^0s and ηs (π^0, $\eta \rightarrow \gamma\gamma$) which form the EM component of the showers and the response of the calorimeter to hadron showers is similar to the one from EM showers. At higher energies (100-200 GeV) of the incident hadron, the response can be non-linear due to the highly non-EM components of hadronic showers, which include

- Ionization by spallation[9] protons that form the non-relativistic shower component.
- Ionization by charged pions, which form the relativistic shower component.
- Kinetic energy carried by evaporation[10] neutrons, which form the non-EM shower component.
- The energy used to release protons and neutrons from the calorimeter nuclei and the kinetic energy carried by the recoil nuclei, which do not form the calorimeter signal. This energy represents the invisible fraction of the non-EM shower energy [41].

Jets consist of a mixture of γs and hadrons. The calorimeter signal generated by this mixture is the sum of the signals from all the particles the jet is composed of. Jets are not always well-defined identities in particle physics experiments. Particles not associated with the jet may happen to travel in the same direction as the jet. For jets produced at large angles with the beam axis in collider experiments, many soft particles may travel at large angles with respect to the direction of the fragmenting object, because of the transverse momentum acquired in the fragmentation process. There are many jet finding algorithms that deal with identifying a jet.

[9] Spallation is a two-stage process in which a struck nucleus breaks up into a cascade of nucleons, which go into the calorimeter, followed by the de-excitation of the remainder of the nucleus by emission of α and γ rays.

3.3 Calorimeter Performance

The energy response of a calorimeter is usually in the form of a calorimeter signal as explained in section 3.2.1. The calorimeter signal is used to measure the kinematical properties of the particle that produced it, such as its energy. To be able to do so, one has to know the relationship between the measured electrical calorimeter signal and actual energy deposited (i.e., the detector calibration) and the precision with which the particle energy is measured. These are generally the measures used to indicate the calorimeter performance.

3.3.1 Energy Resolution

The energy resolution is defined as the precision with which the unknown energy of the particle is measured. A particle of known energy is usually allowed to shower in the calorimeter and the energy is measured by the calorimeter. The precision with which the known energy can be reproduced by detector, then, is the energy resolution of the calorimeter. The energy resolution is considered as the most important performance characteristic of a calorimeter for this study.

3.3.2 Measure of Energy Resolution

The basic phenomena in showers are statistical processes, hence the intrinsic limiting accuracy, expressed as a fraction of total energy, improves with increasing energy as shown in Eq. 3.2.

---

[10] Soft neutrons that carry significant fraction of the hadronic shower energy.

$$\left(\frac{\sigma}{E}\right)_{fluct} \propto \frac{1}{\sqrt{E}} \qquad 3.2.$$

where E is the energy of incident particle (in GeV) and σ is the standard deviation of energy measurement [42]. The total number of shower particles is proportional to the energy of the incident particle, E. This term (also known as sampling term) dominates the energy fluctuation over the useful range of energy measurement in a calorimeter. There are contributions other than statistics due to instrumental effects which are rather energy-independent (e.g., noise, pedestal). Their relative contribution decreases with E as shown in Eq. 3.3.

$$\left(\frac{\sigma}{E}\right)_{instr} \propto \frac{1}{E} \qquad 3.3.$$

This component may limit the low-energy performance of calorimeters. A third component is due to calibration errors, non-uniformities and non-linearities in photomultipliers, proportional counters, ADC's, etc [43]. This contribution is energy-independent as shown in Eq. 3.4.

$$\left(\frac{\sigma}{E}\right)_{syst} \propto const. \qquad 3.4.$$

This component sets the limit for the performance at very high energies.

Thus the energy resolution of a calorimeter can be expressed as in Eq. 3.5:

$$\left(\frac{\sigma}{E}\right)_{Total} = \frac{A\%}{\sqrt{E}} + \frac{B\%}{E} + C\% \qquad 3.5.$$

where A, B and C are fixed for a given calorimeter and uniquely determine its energy resolution and are usually expressed in percent. The units of energy are usually in GeV.

3.4 Practical Considerations in Calorimetry

Calorimetry is the art of compromising between conflicting requirements; the principal requirements [44] are usually formulated in terms of resolution in energy, position and time, in triggering capabilities, in radiation hardness of the materials used, and in electronics parameters like dynamic range, and signal extraction (for high-frequency colliders). In nearly all cases, cost is the most critical limiting parameter. Depending on the physics goals, the energy range that has to be considered and the accelerator characteristics, some capabilities will be favored over others. The range of possible technologies for calorimeters is much wider than for tracking devices [42], and imaginative experimental teams have found quite ingenious solutions over the past two decades, since calorimeters became key components of particle detectors.

3.5 Energy Flow Technique

To improve the jet energy resolution of the calorimeter, the ALEPH [52] collaboration at Large Electron Positron (LEP) experiment developed an “Energy Flow” (EF) technique, which takes advantage of the low particle multiplicity in electron-positron (e^+e^-) collisions [13]. The EF technique requires a precise tracking system that

can measure the trajectories and momenta of charged particles. The essence of the technique is to associate a charged track with an energy cluster in the calorimeter and replace the calorimeter energy with the better measured track momentum. The energy clusters associated with tracks are then eliminated from the calorimeter energy sums. The remaining energy is associated with the energy deposited by neutral particles. Since typically the momenta measured by tracking systems are of higher precision than the energy measurement from calorimeters, and on average about 65% of hadronic jet energy is carried by charged particles, this technique naturally improves jet energy resolution.

The EF method requires high calorimeter granularity to isolate tracks associated with energy clusters. The tracking volume must be large or have a strong magnetic field to permit spatial separation of particles at the calorimeter. Given the energy regime of a future linear collider, it is necessary to cover a large volume, resulting in a significant increase in the number of readout channels. Due to the cost of the readout system, the overall price of a hadronic calorimeter compatible with the EF technique is likely to be expensive using conventional analog readout.

CHAPTER 4

GEM ANALOG CALORIMETER PERFORMANCE STUDY

4.1 Introduction

A simulation study of Gas Electron Multiplier (GEM) [45] based Digital Hadronic Calorimeter (DHCal) was performed. The energy response and resolution of the calorimeter were evaluated, and the results looked encouraging [46]. The simulation study performed as a part of this thesis, aims at gaining a deeper understanding of the response of a calorimeter and its performance using two different approaches - analog and digital. The analog approach was performed in an earlier study [46]. The study also investigates techniques to remedy several shortcomings of the earlier an approach [46], which include improved statistics for analysis, a better understanding of systematic effects and an improved fitting procedure. Single charged pions are chosen for the study to simplify the analysis since the study of pion response provides much information on detector performance. The pion interaction with a nucleus in the calorimeter medium produces secondary hadrons, which interact with other calorimeter nuclei. This results in the development of hadron particle avalanche (showers), which deposit majority of their energy in the Hadronic calorimeter (for detailed explanation see section 3.2.4). The results of the single pion performance study and the underlying procedure are presented in this chapter.

4.2 Calorimeter Geometry

4.2.1 Electromagnetic Calorimeter - geometry

The electromagnetic calorimeter (Ecal) used in the simulation for TESLA Technical Design Report (TDR) [31] consists of a barrel closed at each end by an end-cap. The barrel is divided into eight staves, with each stave subdivided into five modules. Each module is placed 1700 mm radially from the beam axis (Z). It has forty layers of tungsten/silicon sandwiched plates.

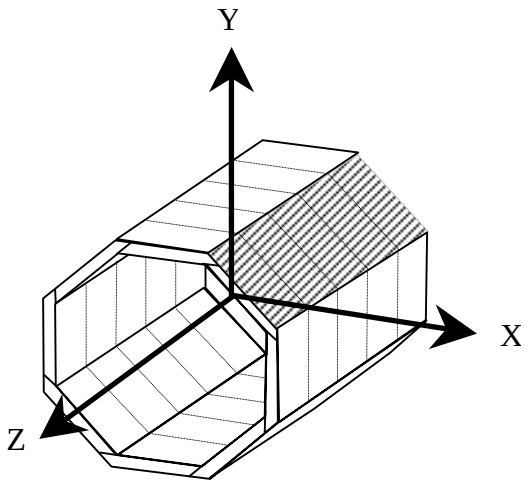

Fig. 4.1 Electromagnetic section of the calorimeter. Barrel with the five modules in a stave is shown shaded. Staves are arranged as an octagon surrounding the beam axis.

For all layers the silicon (Si) plate is 0.5 mm thick and is embedded in two G10 plates (typically 60% SiO_2 and 40% epoxy) of 0.8 mm each. For the first thirty layers the tungsten is 1.4 mm thick and for the last ten layers, 4.2 mm. Data is collected as hits only in the Si plates, in cells of approximately 1 cm^2 area. To ensure that all cells have

the same surface, the Si plate horizontal dimensions are always multiples of 10 mm and the Si plate placements are left adjusted inside the module. Each end-cap has four modules. Each module has the same layer structure and thickness as for the barrel but the plates are perpendicular to the Z-axis. The end-caps are placed 2800 mm (along Z direction) away from the detector collision point.

4.2.2 Hadronic Calorimeter - geometry

The Hadronic calorimeter (Hcal) consists of a barrel surrounding the Ecal, closed at each end by an end-cap. Like in Ecal, the barrel of the Hcal is also divided into eight staves, each stave being divided into five modules. Each module has forty layers, each layer with plates of 18 mm of Fe and 6.5 mm of sensitive material. The Hcal hits are collected in cells of size approximately 1 cm^2.

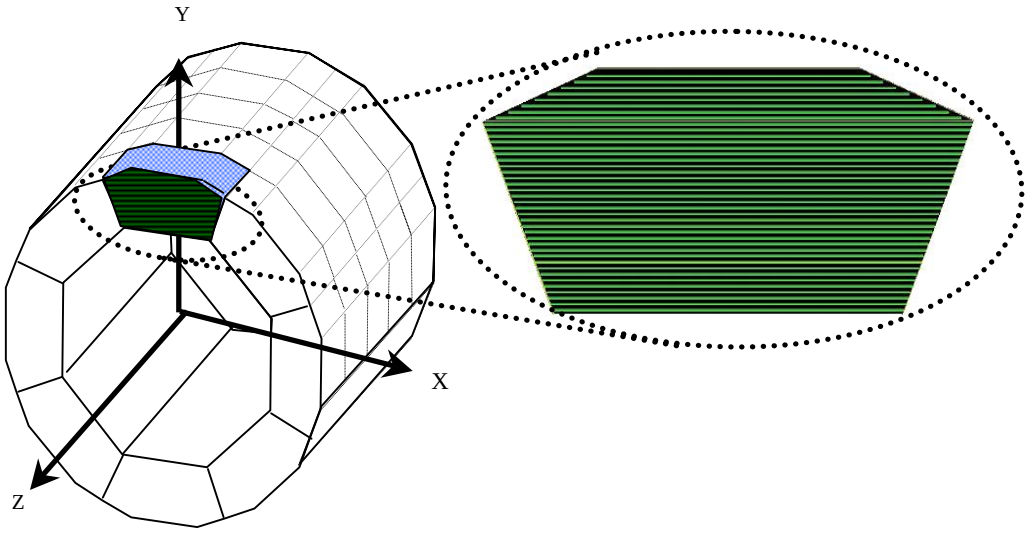

Fig. 4.2. Hadronic section of the sampling calorimeter. The Barrel is composed of eight staves and each stave consists of five modules. One of the modules is shown shaded. The inset shows the layered structure of a module, which consists of forty alternating layers of active and passive medium.

4.2.2.1 Gas Electron Multiplier (GEM) Sensitive Gap - geometry

The Gas Electron Multiplier (GEM) [4.1, 4.2, and 4.3] consists of a thin, copper clad polymer foil (typically, made of kapton), chemically pierced by a high density of holes (typically 50 to 100 per mm^2). The foil is enclosed in a gas (for this study and for the prototype, a mixture Argon, Ar and Carbon-dioxide, CO_2, in the ratio 70:30 by volume), and is the active medium in the sampling calorimeter. When shower particles pass through the active medium, they ionize the gas (see section 3.4.1). A suitable voltage (400 V for this study) is applied across the GEM foil will cause the electrons produced by ionization to drift into the high electric field in the holes and multiply. Each hole acts as an individual proportional counter. The schematic diagram of the structure of two-layer GEM cascade (or double GEM) is shown in Fig. 4.3. In the double GEM detector three different electron drift regions are defined: the radiation conversion region, where the primary ionization electrons are created, the transfer region between successive layers of GEM and the induction region between the last GEM and the anode.

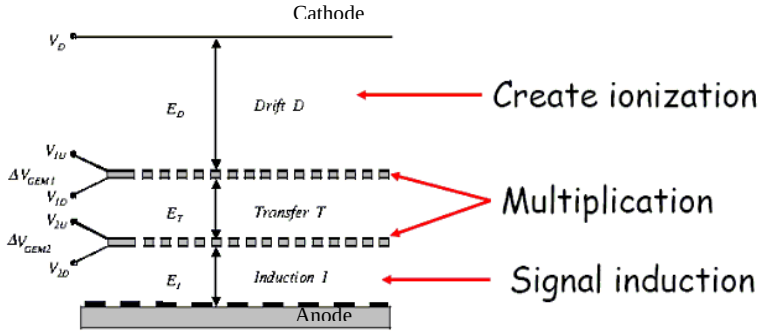

Fig. 4.3 Double GEM Schematic (S.Bachmann et al CERN-EP 2000-151)

The TESLA TDR geometry for the Hcal consists of 6.5 mm of polystyrene scintillator as the active medium. This medium is replaced with GEM for the analysis of this thesis (details of how to replace the active gap can be found in Appendix B). The detailed double GEM geometry is shown in Fig. 4.4 a). The gas composition and the materials that make up the double GEM are implemented for the Hcal simulation using Mokka [29]. The live energy deposited in Hcal by a 75 GeV pion for a thousand event samples is shown in Fig. 4.4 b). The GEM intrinsic gain obtained in the energy is not considered here. The CPU time required for simulation of detailed GEM is 43.7 s/event (see Appendix B).

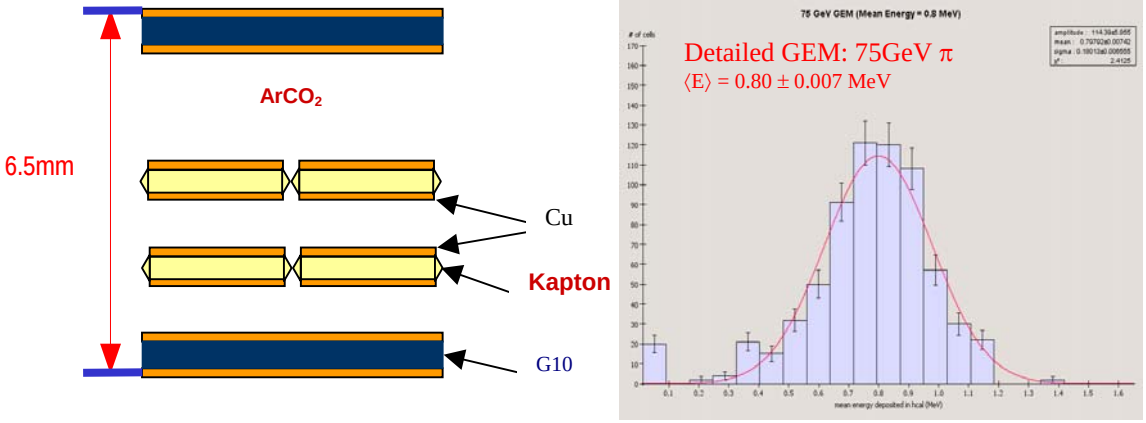

Fig. 4.4 a) Detailed GEM Geometry b) Live Energy for 75 GeV Pion

Given the large processing time for the detailed GEM geometry, we also developed a simple GEM simulation. This replaces the solid material of the double GEM with a uniform material of equivalent average density, called simple GEM. This newly defined material, along with the gas is expected to reproduce the same average behavior as the detailed GEM.

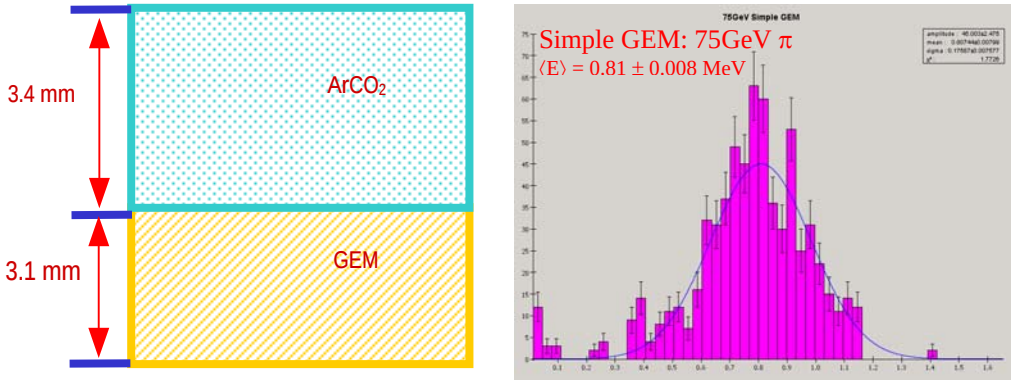

Fig. 4.5 a) Simple GEM Geometry b) Live Energy for a 75 GeV Pion

The simple GEM schematic is shown in Fig. 4.5 a) and is implemented using Mokka [29]. One thousand events were simulated with simple GEM with 75 GeV pions. The live energy distribution (without considering the GEM intrinsic gain) is shown in Fig. 4.5 b). The average values of the live energy for detailed GEM and simple GEM are virtually identical. This gives us the confidence to use simple GEM in further studies without compromising any performance. The advantage of implementing simple GEM geometry is the CPU time required to simulate an event, which is measured to be 25.2 s/event. This is about half the CPU time required for the detailed GEM. For the remainder of the analysis in this thesis, simple GEM is used.

4.2.3 Tracking Detector - geometry

The physics goals of the linear collider requires that the detector have excellent momentum resolution ($\Delta(1/p) = 5 \cdot 10^{-5} (GeV/c)^{-1}$) in the central region, very high b- and c-tagging efficiency to identify multi-b final states like ZHH and $t\bar{t}H$ and to separate

$H \to c\bar{c}$ events from $H \to b\bar{b}$ decay. One of the components of a tracking detector that has been optimized to fulfill these requirements is the Time Projection Chamber (TPC) [58].

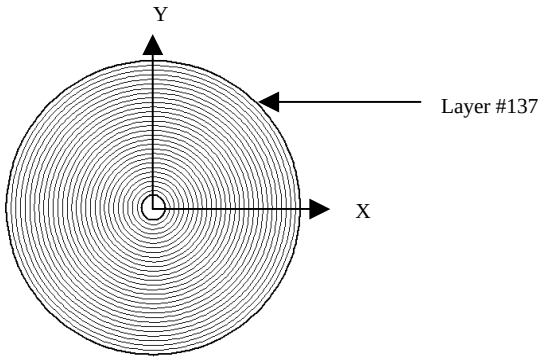

Fig. 4.6. Cross sectional view of the tracking detector used in simulation.
It is made of 137 Ar rings placed in concentric circles
in between the inner and outer Al rings

The geometry of such a detector is built into the Mokka framework and the tracking information is stored in the tracking hits format. Figure 4.6 shows the tracking detector (TPC), which consists of several Argon (Ar) rings inside the inner and outer Aluminum (Al) TPC walls.

4.3 Event Statistics

The evaluation of the performance of the Hcal calorimeter requires simulation of many events to obtain the required precision. The statistical sampling fluctuation in the data is governed by the rules of Poisson statistics. Let us suppose, that in a sampling calorimeter simulation we choose (N = 50000) events with charged pions traversing the active calorimeter layers. The signal obtained is the sum of all the signals obtained by

individual shower particles produced by the charged primary particle. The standard deviation in sampling fluctuations (σ_{stat}) is given by Eq. 4.1.

$$\sigma_{stat} \propto \frac{1}{\sqrt{N}} \approx \frac{1}{\sqrt{50000}} \approx 0.45\% \qquad 4.1.$$

If no other fluctuations other than statistical contribute significantly, then the sampling error is 0.5%. The incident pion energies used in the simulation were 5, 10, 15, 20, 25, 35, 50, 75 and 100 GeV with 50,000 events for each energy value.

4.4 Simulation Output Format

The Mokka [29] simulation generates one output file for each event for each detector piece, in addition to a log file, a control file, event kinematics, primary trajectories and tracking information. All the files are in ASCII data format. The Ecal and Hcal output data files have information regarding the primary and secondary particles that traversed the detectors, the energy deposited by them in each cell and the co-ordinates of the cells that were hit. Output file data format for an event for Ecal and the Hcal are shown in Table 4.1.

Table 4.1 Mokka output- Hits format for Ecal and Hcal calorimeters

P	S	M	I	J	K	X	Y	Z	E	PID	PDG
2	1	3	33	54	1	-361.75	1702.75	0	**1.51E-01**	1	-211
2	1	3	33	54	2	-357.85	1706.65	0	**1.43E-01**	1	-211
2	1	3	32	54	3	-363.95	1710.55	0	**1.33E-01**	1	-211
2	1	3	32	54	4	-360.05	1714.45	0	**1.29E-01**	1	-211

P: Detector Piece Number

1- Ecal End Cap in -Z Direction

2- Ecal Barrel

3- Ecal End Cap in +Z Direction

4- Hcal End Cap in -Z Direction

5- Hcal Barrel

6- Hcal End Cap in +Z Direction

S: Stave Number (1-8 for barrel, 1-4 for end caps)

M: Module Number in a Stave (1-5 for barrel, 1 for end caps)

I and J: Cell Coordinates in the Cells Matrix (I, J >= 0)

K: Sensitive (Si or Scintillator) Layer Number (K >= 1)

X, Y and Z: Cell Center in World Coordinates

E: Total Energy Deposited in the Cell by the PID Particle and its Secondaries.

PID: Primary Particle ID in the Pythia file.

PDG: Particle Type (electron, positron, etc.,)

Output file data format for an event for tracker is shown in Table 4.2. Hits information consists of particle position, momentum and the total deposited energy when crossing a ring. The hits information is stored in ASCII format for each event.

Table 4.2 Hits format for the tracking detector.

Layer	X	Y	Z	Px	Py	Pz	PID	PDG	E
1	23.89	325.31	0.07	368.83	7627.3	3.43	2	-211	1.92E-03
2	24.29	335.36	0.07	356.89	7627.9	3.49	2	-211	1.48E-03
3	24.68	345.41	0.08	345.02	7628.4	3.43	2	-211	1.85E-03
4	25.07	355.46	0.08	333.1	7629	3.36	2	-211	2.53E-03

- Layer: the layer number
- X, Y, Z: hit point (the layer middle point when crossing)
- Px, Py, Pz: the particle momentum
- PID: primary Particle ID in the Pythia input file
- PDG: particle type (electron, positron, etc), it can be not the primary type if its one of its secondaries.
- E: the total energy deposited by the PID particle or one of its secondaries.

4.5 Determination of Energy from Hits Information – Measured Energy

The total energy deposited by a charged pion in a calorimeter is measured as the sum of the energy deposited in each cell in the Ecal and Hcal. Since the Ecal and Hcal modules have many layers and many cells in each layer, it is convenient to represent the total energy measured in the calorimeter as the sum of energy measured in each cell $\sum E_j$. The subscript j refers to a summation over all the calorimeter cells that have energy deposited in a given event (it also represents the number of entries in the hits output file). The Hcal modules consist of a similar layered structure with cells, but for each cell, there is an intrinsic gain factor (G) that is used to scale the measured energy in Hcal. The gain factor is fixed by the choice of double GEM and is given as an input

parameter. So, if we represent Ecal and Hcal separately, and take into account the intrinsic gain of the Hcal, the total energy measured in both the calorimeters can be summed up to represent the measured energy of the charged pion. If $\sum_j E_{EM/j}$ represents the total energy deposited in the Ecal and $\sum_j G \cdot E_{HAD/j}$ represents the total energy deposited in the Hcal, Total live energy measured per event is given by Eq. 4.2.

$$E_{LIVE} = \sum_j E_{EM/j} + \sum_j G \cdot E_{HAD/j} \qquad 4.2.$$

4.6 Determination of Weighting Factor

The material composition of Ecal and Hcal are different. Owing to the differences in the active media, the calorimeter responses are different. The total energy measured by both the calorimeters for a given incident energy pion is non-gaussian. Fig. 4.7 illustrates this fact with total energy measured for a 50 GeV Pion. The distribution shows non-gaussian behavior with two distinct peaks. Hence a method is needed to compensate for the differences in responses. The weighting factor (W) is introduced to compensate for the differences in the response of Ecal and Hcal.

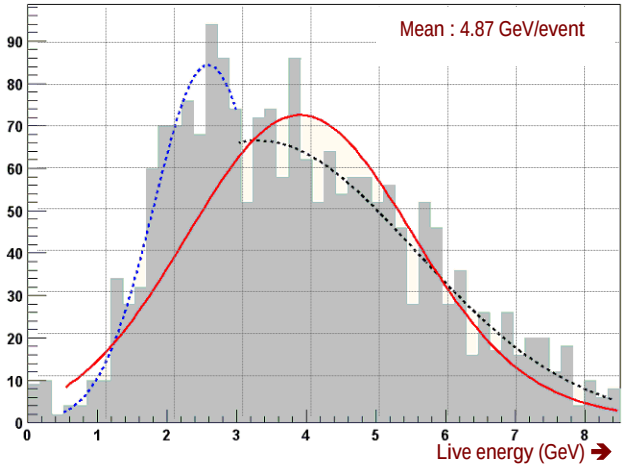

Fig. 4.7 Total Energy of a 50 GeV pion showing double peaked structure. Ecal response is shown blue dotted line black dotted line shows the Hcal response. The red solid line indicates the gaussian fit to the Total Energy measured.

If we represent the total energy measured as the sum of the energies measured in the Ecal and Hcal, then we can define the corrected-live energy or corrected energy as given in Eq. 4.3.

$$E_{CORR} = \sum_{j} E_{EM\,/\,j} + W \sum_{j} G \cdot E_{HAD\,/\,j} \qquad 4.3.$$

To determine W we have to obtain the gaussian fit to events that predominantly Electromagnetic (EM) and events that are predominantly Hadronic (HAD). If the fraction of total live energy measured in Ecal is more than, say 85% of the total live energy, then the event is considered predominantly EM. This fraction is called the electromagnetic fraction (f_{EM}) denoted by Eq. 4.4. The hadronic fraction f_{HAD} can be defined as in Eq. 4.5. If hadronic fraction is greater than 85%, then the event is considered as predominantly hadronic.

$$f_{EM} = \frac{\sum_j E_{EM/j}}{\sum_j E_{EM/j} + \sum_j G \cdot E_{HAD/j}} \qquad 4.4.$$

$$f_{HAD} = \frac{\sum_j G \cdot E_{HAD/j}}{\sum_j E_{EM/j} + \sum_j G \cdot E_{HAD/j}} \qquad 4.5.$$

Events with $f_{EM} \geq 0.85$ are selected to measure Ecal response and events with $f_{HAD} \geq 0.85$ are selected to measure Hcal response. The events that do not satisfy both these criteria are not considered for this analysis.

4.6.1 Determination of Statistical and Systematic Errors

The energy deposition in a single layer of Ecal shows a Landau type statistical distribution. In the Ecal, the average value of Z for tungsten (passive medium) is more than that of silicon (active medium); the response to electromagnetic showers is smaller than the response to minimum ionizing particles (see section 3.2.3) [36, 37 38 39]. In summing the energy over all the layers in the Ecal, however, the contribution form Landau type energy distributions add up and in the limit where there are infinitely many sampling layers, approach a gaussian. In addition, the sampling fluctuations obey Landau statistics, and in the limit when the number of events becomes sufficiently large, these fluctuations show a gaussian behavior. Since there are a finite number of sampling layers in Ecal and Hcal, and the event-by-event statistical fluctuations is Landau-like, the sum of gaussian and Landau fit is chosen for parameterization of

energy distribution in the Ecal and the Hcal. The Landau fit is defined using three parameters, the most probable value (MPV), the Landau width and the amplitude. The gaussian fit is defined by three parameters, the gaussian mean, width and the amplitude. In the analysis, the sum of Landau and gaussian fits is therefore described by six parameters, with the appropriate values of the amplitude. We would expect the amplitude of the Landau part to approach zero in the limit that the number of events becomes large.

The gaussian mean of the combined fit is chosen as the central value of the measured energy, with the appropriate error on mean as the statistical error. The systematic errors are estimated using a constrained gaussian fit. The difference in the mean value of the constrained fit and the mean value corresponding to the combined fit is chosen as the systematic error. The total error is obtained by adding the statistical error on the central value and the systematic error in quadrature.

A sample calculation underlined below will make this procedure clear. The mean value of measured energy obtained for a charged pion with an incident energy of 5 GeV for the combined fit is (107.80 ± 1.08) MeV and the corresponding value for the constrained gaussian fit is (117.71 ± 0.39). If we denote the systematic error by ΔE_{sys} and the statistical error by ΔE_{stat}, the total error is given by Eqs. 4.6 – 4.8.

$$\Delta E_{sys} = (117.71\text{-}107.80)\ \text{MeV} = 9.91\ \text{MeV} \qquad 4.6.$$

$$\Delta E_{stat} = 1.08\ \text{MeV} \qquad 4.7.$$

$$\Delta E_{total} = \Delta E_{sys} \oplus \Delta E_{stat} = \sqrt{\Delta E_{sys}^2 + \Delta E_{stat}^2} = 9.96 \text{ MeV} \qquad 4.8.$$

The live energy deposition in Ecal and Hcal for various values of incident pion energies is illustrated in Figs. 4.8 and 4.9 respectively.

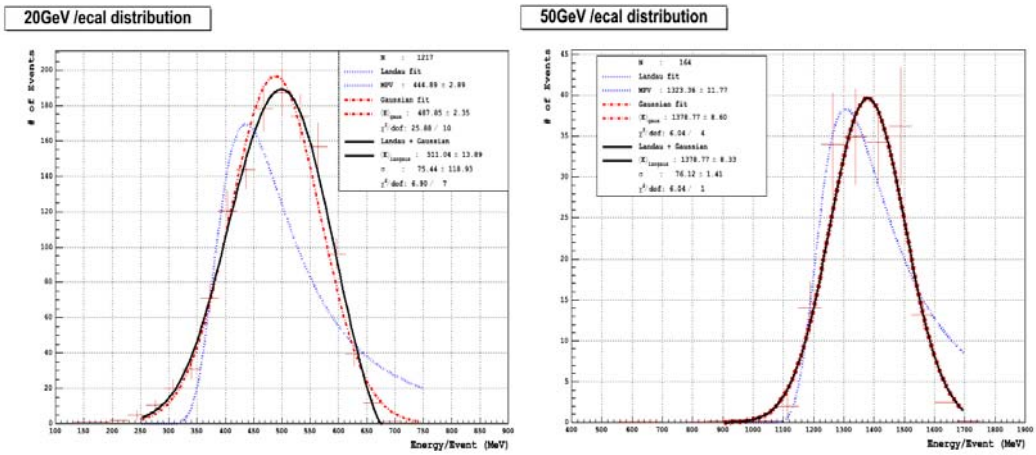

Fig. 4.8 EM response for 20 and 50 GeV pions. The energy distribution is fit with Landau (blue dotted line) and gaussian (red solid line) and the sum of the Landau and gaussian (black solid line).

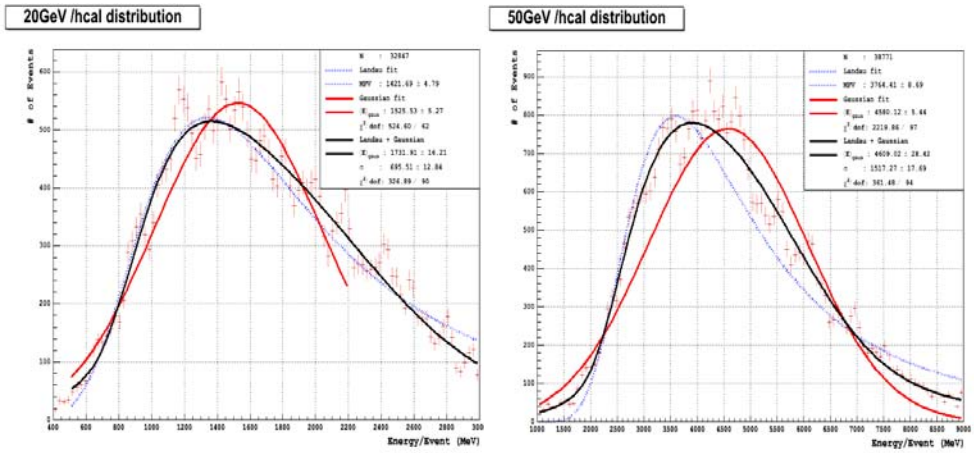

Fig. 4.9 Hadronic response for 20 and 50 GeV pions. The fits to the raw distributions are shown. The distributions show a greater fluctuation (longer Landau tail shown in blue dotted line)

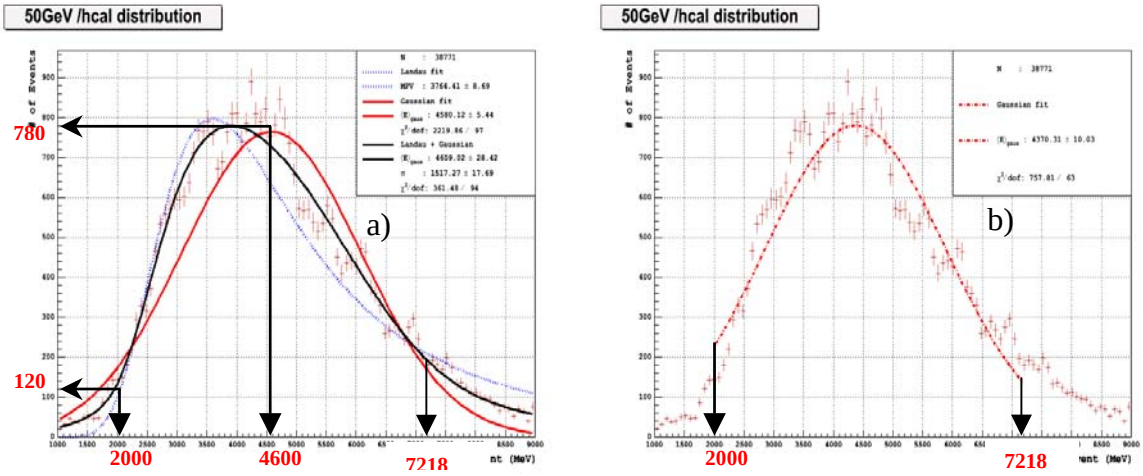

Fig. 4.10 a) and b) Illustration of fitting procedure. Combined Landau and gaussian fit is shown on the left (black solid). The gaussian fit that corresponds to 15% of the peak of the combined fit is shown on the right (red dotted).

The determination of the fit parameters for the constrained gaussian fit for both Ecal and Hcal is shown with the following example. Figure 4.10 a) shows that the gaussian mean of the combined fit is ≈ 4609 MeV. The interval in which this value is located ≈ 780 events. So (15% of 780 ≈ 120) events correspond to 2000 MeV. The length of half the fit interval is (4609-2000) MeV = 2609 MeV. Therefore the fit interval is 2000 MeV to (4609+2609) MeV = 7218 MeV. The constrained fit is shown in Fig. 4.10 b). In a similar way the systematic errors on the measured energy are estimated for every incident energy of the pion. Figures 4.11 and 4.12 show the constrained fit on the live energy distribution for Ecal and Hcal respectively.

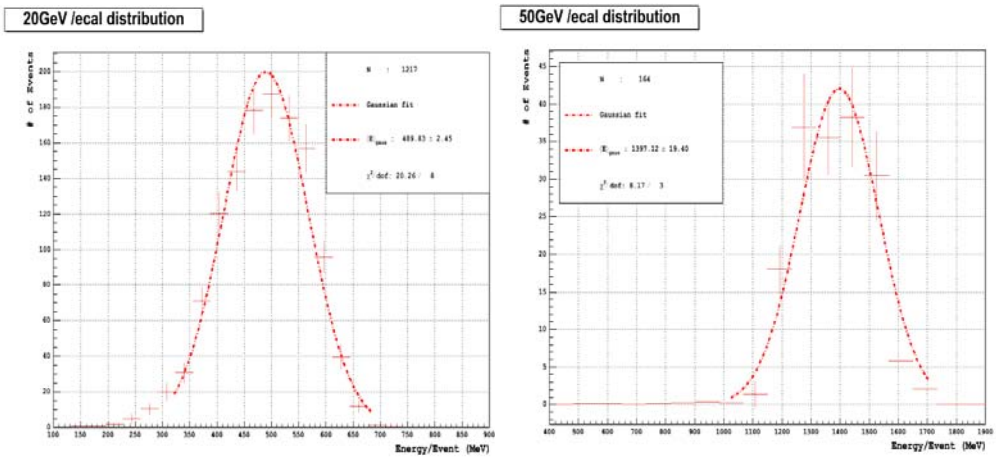

Fig. 4.11 EM response for 20 and 50 GeV pions with constrained gaussian fits.

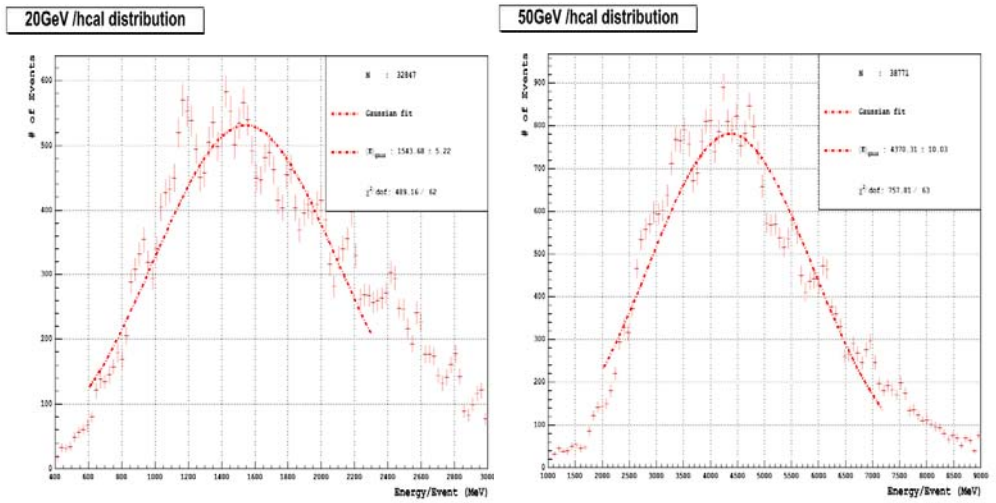

Fig. 4.12 Hadronic response for 20 and 50 GeV pions with constrained gaussian fits.

4.6.2 Punch through Effects

Hadronic shower development is based on nuclear interactions, and therefore the shower dimensions are governed by the interaction length, λ_{int}. The pion may travel

through the calorimeter for a distance z without undergoing nuclear interaction with a finite probability, given by Eq. 4.9.

$$P = e^{-z/\lambda_{\text{int}}} \qquad 4.9.$$

The simple calculation (see Appendix C) shows that the Hcal size in the longitudinal direction is about $5\lambda_{\text{int}}$. Therefore the probability of pion punch through is $P = e^{-5\lambda_{\text{int}}/\lambda_{\text{int}}} = e^{-5} \approx 0.673\ \%$. For a 50 GeV pion, out of 50000 events, we expect to see about 336 such events. Figure 4.13 illustrates the punch-through events for a 50 GeV pion through Hcal.

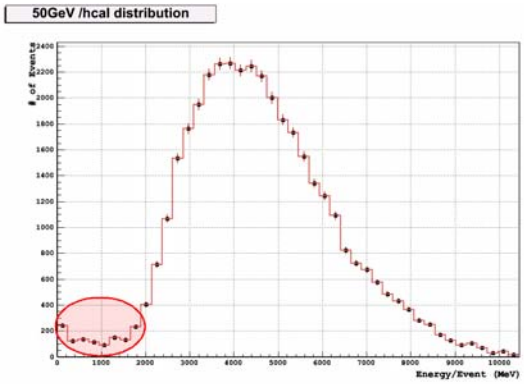

Fig. 4.13 Inset shows the punch-through events in Hcal for 50 GeV pions. The lower end energy deposition is dominated by punch-through events.

The results obtained from the simulation showed 323 events where a pion passed through both the Ecal and Hcal without undergoing nuclear interaction. This is in excellent agreement with the expected value. Such events are ignored in evaluating the energy response of the calorimeters.

4.6.3 Electromagnetic Calorimeter Response

It is desirable that the EM response be intrinsically linear for EM shower detection because the kinetic energy of the showering electrons or photons is proportional the calorimeter signal. If we denote the calorimeter signal by $E_{live/EM}$ and the energy of the incident pion by E_π, and M_{em} as the sampling fraction and ignore the noise term of the calorimeter, the relationship between these quantities can be expressed in the form of Eq. 4.10.

$$\left(E \pm \Delta E\right)_{live/EM} = \left(M_{em} \pm \Delta M_{em}\right) \cdot E_\pi \qquad 4.10.$$

Figure 4.14 shows the EM response to charged pions of different incident energies. The response data is described with a linear fit and the sampling fraction obtained as the slope of the line. It is given by Eq. 4.11.

$$M_{em} \pm \Delta M_{em} = 28.32 \pm 0.4567 \text{ MeV/GeV} \qquad 4.11.$$

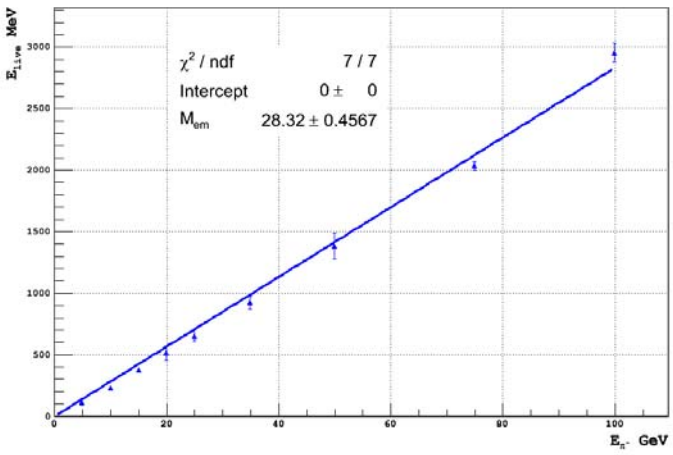

Fig 4.14 Ecal response for different incident pion energies. The response is linear and is constrained to have zero constant term.

4.6.4 Hadronic Calorimeter Response

Hadronic response is obtained in a similar manner as the EM response. The relationship between the measured energy in the Hcal ($E_{live/HCAL}$), the incident energy of the pion (E_π) and the sampling term (M_{hcal}) is given by Eq. 4.12. Equation 4.13 gives the sampling fraction.

$$(E \pm \Delta E)_{live/HCAL} = (M_{hcal} \pm \Delta M_{hcal}) \cdot E_\pi \qquad 4.12.$$

$$M_{hcal} \pm \Delta M_{hcal} = 90.85 \pm 1.047 \text{ MeV/GeV} \qquad 4.13.$$

Figure 4.15 shows the linear Hcal response. The fit is constrained (constant term is zero, meaning that there is no noise) and linear.

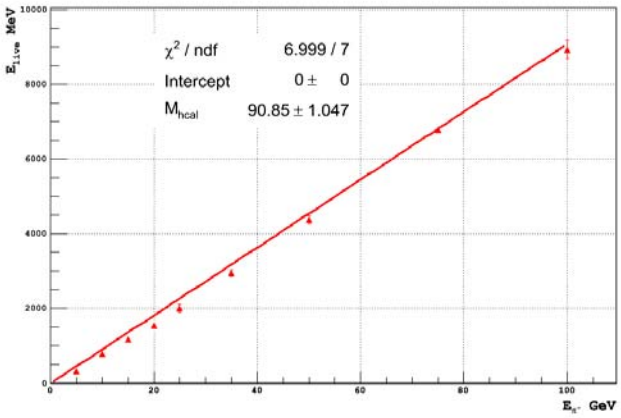

Fig 4.15 Hcal response for different incident pion energies. The response is linear and is constrained to have zero constant term.

The Ecal and Hcal responses are different and hence have different sampling fractions. Figure 4.16 illustrates this fact, where both Ecal and Hcal responses are plotted on the same plot. On the abscissa, the incident pion energy (E_π) is represented in units of GeV

and on the ordinate; the measured pion energy (also called live energy, E_{live}) is represented in units of MeV. The weighting factor is defined as the ratio of the sampling fraction of Ecal to that of Hcal and is used to normalize the Ecal and Hcal detector responses. The weighting factor ($W \pm \Delta W$) is determined by Eqs. 4.14 and 4.15.

$$W = \frac{M_{EM}}{M_{hcal}} = \frac{28.32}{90.85} = 0.3117 \qquad 4.14.$$

$$\Delta W = W \cdot \sqrt{\left(\frac{\Delta M_{em}}{M_{em}}\right)^2 + \left(\frac{\Delta M_{hcal}}{M_{hcal}}\right)^2} \qquad 4.15.$$

$$= 0.31 \cdot \sqrt{\left(\frac{0.46}{28.32}\right)^2 + \left(\frac{1.05}{90.85}\right)^2} = 0.0198$$

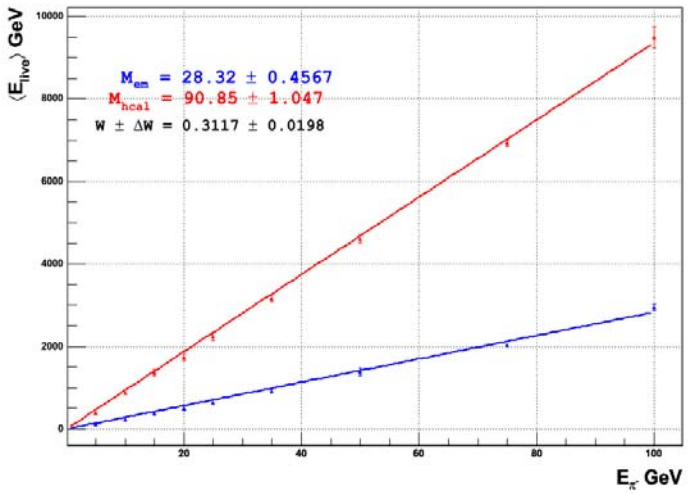

Fig. 4.16 Ecal and Hcal responses are shown in the same plot and the weighting factor is obtained as the ratio of the slopes of Ecal and Hcal.

4.7 Determination of Corrected Energy

Once the weighting factor is determined, the corrected energy can be computed using Eq. 4.3. The corrected energy distribution is then obtained as combined Ecal and Hcal response, or the Calorimeter Response. The corrected energy distribution removes the double peaked structure found in the live energy distribution. A similar approach is followed to determine the systematic and statistical errors, as was for the Ecal and Hcal responses. The corrected energy distribution for the combined Landau and gaussian fit is shown for various energies in Fig. 4.17 and the constrained gaussian fit is shown in Fig. 4.18.

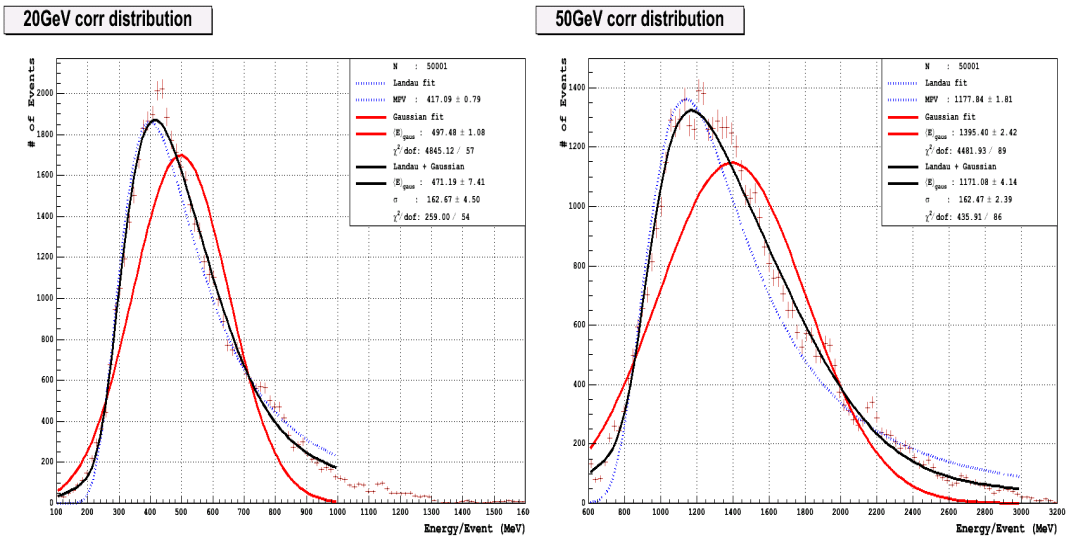

Fig. 4.17 Corrected energy deposit for different incident energies. The Landau fit is shown in blue dotted line, the red solid line indicates the gaussian fit and the black solid line indicates the sum of Landau and gaussian fit.

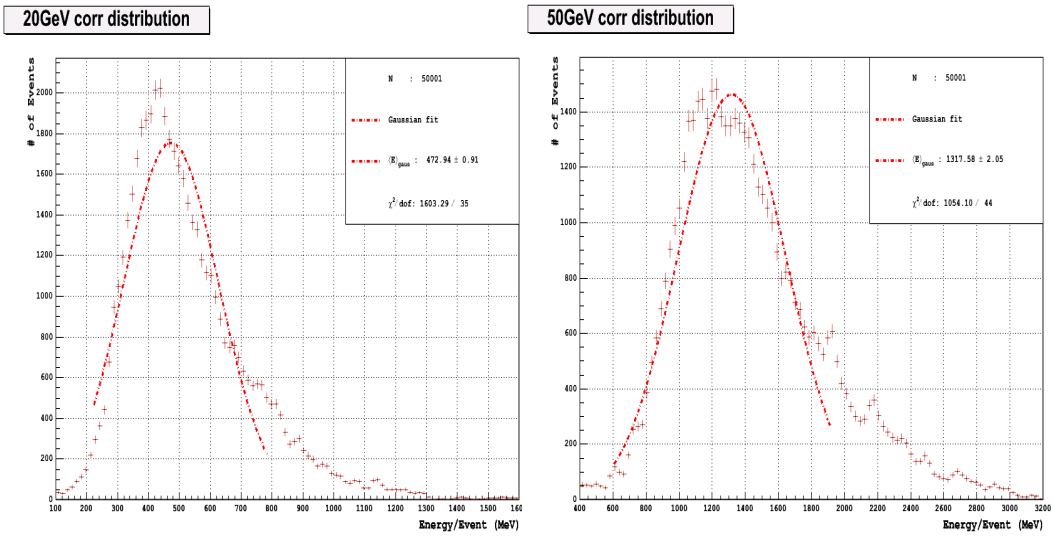

Fig. 4.18 Corrected energy for 20 and 50 GeV pions, with constrained gaussian fits.

The next step is to obtain the true response of the calorimeter and the corrected sampling fraction of the calorimeter. The mean value of the energy for each energy bin is considered as the central value and the difference in the mean from the constrained gaussian fit is considered as the systematic uncertainty. The corrected response is shown in Fig. 4.19. The sampling term is obtained in the same manner as the Ecal and Hcal. It is summarized in Eqs. 4.16 and 4.17.

$$\left(E \pm \Delta E\right)_{CORR} = \left(M_{corr} \pm \Delta M_{hcal}\right) \cdot E_{\pi} \qquad 4.16.$$

$$M_{corr} \pm \Delta M_{corr} = 27.67 \pm 0.74 \text{ MeV/GeV} \qquad 4.17.$$

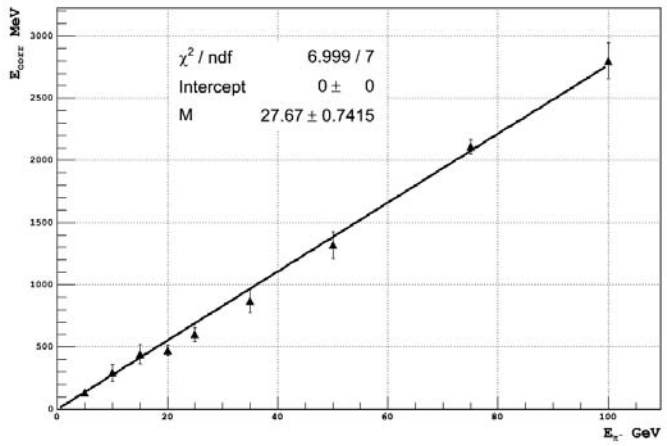

Fig. 4.19 Corrected energy response for various incident pion energies. The slope is the sampling fraction.

4.8 Energy Resolution

The corrected response obtained for the calorimeter is then used to compute the energy resolution to determine the performance of the calorimeter. The converted energy should theoretically be identical to the incident energy of the pion. The converted energy is represented in Eq. 4.18:

$$\left(E \pm \Delta E\right)_{CONV} = \left(M_{corr} \pm \Delta M_{corr}\right) \cdot \left(E \pm \Delta E\right)_{CORR} \qquad 4.18.$$

The converted energy distributions with the combined gaussian and Landau fit are shown in Fig. 4.20 for various incident pion energies. The constrained gaussian fit for the same energy bins are shown in Fig. 4.21. The functional form for the energy resolution of a calorimeter can be expressed as given in Eq. 3.5.

For the study, only the statistical and systematic effects are considered in evaluating the energy resolution and instrumental effects like electronic noise, pedestal etc. are ignored. Hence, the second term in Eq. 3.5 can be considered as zero and the energy resolution can be expressed as in Eq. 4.19.

$$\left(\frac{\sigma}{E}\right)_{Total} = \frac{A\%}{\sqrt{E}} + C\% \qquad 4.19.$$

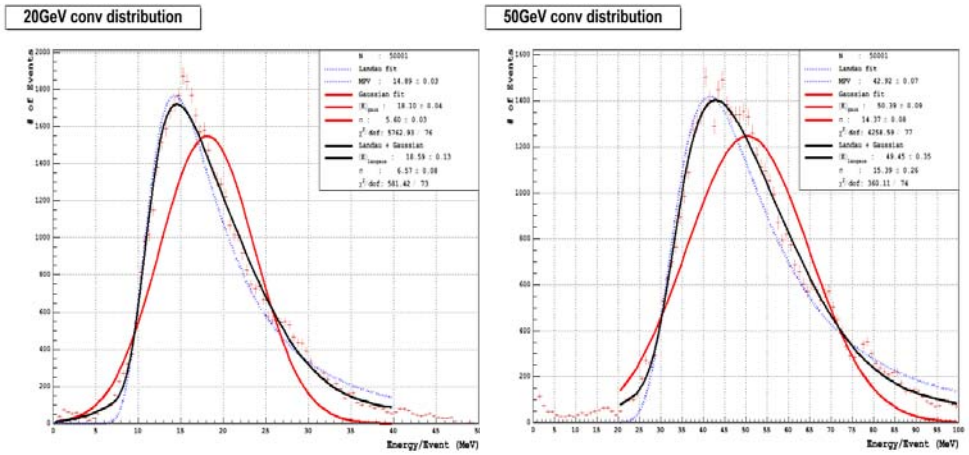

Fig 4.20 Converted energy for 20 and 50 GeV pions after the sampling fraction is applied. Combined fits (Landau in blue dotted, gaussian in red dotted and sum of the two in black solid) are shown for different incident pion energies.

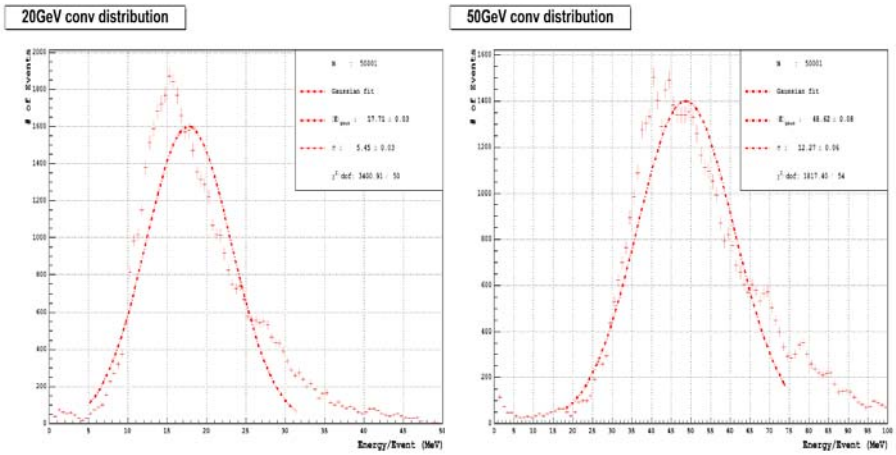

Fig 4.21 Converted energy with constrained gaussian fits for 20 and 50 GeV pions.

The energy resolution is plotted in Fig. 4.22. The functional form given in Eq. 4.19 is used in fitting the resolution data. The functional form obtained for the fit is given in Eq. 4.20. The calculation of errors for this functional form is given in Appendix D.

$$\frac{\sigma}{E} = \frac{(39.67 \pm 1.53)\%}{\sqrt{E}} + (20.71 \pm 0.33)\% \qquad 4.20.$$

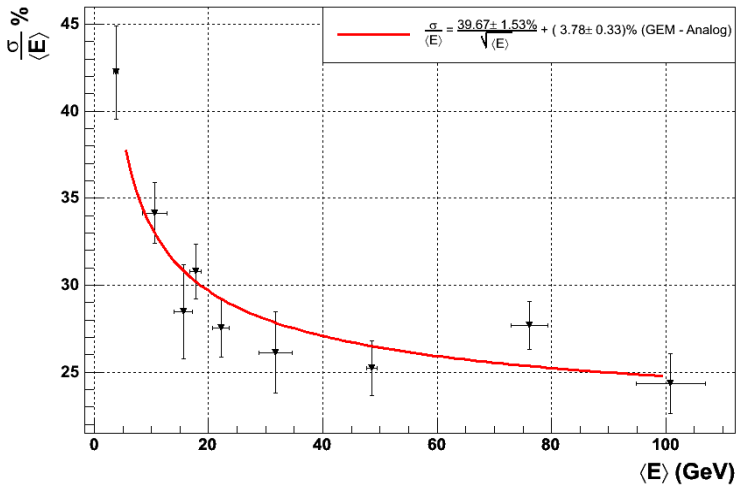

Fig. 4.22 Energy Resolution for the calorimeter in analog mode is shown with fit.

The results are summarized in Tables 4.3, 4.4, 4.5 and 4.6. The first column in each table indicates the incident energy of the pion (E_π in GeV). In Tables 4.3-4.6 the second column indicates the mean value, $\langle E_{langaus} \rangle$ of the energy obtained from the combined Landau and gaussian fit. In Tables 4.3 and 4.4 it is the measured energy (in MeV) in the Ecal and Hcal respectively. In Table 4.5 it is the corrected energy (in MeV) and in Table 4.6 it denotes the converted energy (in GeV). The third column indicates

the mean value of the energy, $\langle E_{gaus} \rangle$ obtained from the constrained gaussian fit. In Tables 4.3 and 4.4 it is the measured energy in the Ecal and Hcal respectively (in MeV). In Table 4.5 it is the corrected energy (in MeV) and in Table 4.6 it denotes the converted energy (in GeV). The fourth column in each table denotes the statistical error on the mean ($\Delta E_{langaus}$) of the combined fit. The fifth and sixth column indicate the chi-square (χ^2) and the degrees of freedom (dof) from the combined fit. The seventh column in Tables 4.3-4.5 is the total error ΔE_{total}, which is computed with the statistical and systematic errors added in quadrature using Eq. 4.8. The eighth column in Tables 4.3-4.5 indicates the modified total error $\Delta E'_{total}$, which is given by Eq. 4. 21.

$$\Delta E'_{total} = \Delta E_{total} \cdot \sqrt{\frac{\chi^2}{dof}} \quad \text{.....Eq. 4.21}$$

The seventh and eighth column in Table 4.6 is the gaussian width $\sigma_{<E/langaus>}$ and the error on sigma ($\Delta\sigma_{<E/langaus>}$, the statistical error) of the combined fit for the converted energy. The ninth column is the gaussian width $\sigma_{<E/gaus>}$ of the constrained gaussian fit for the converted energy.

Table 4.3 Ecal response (live energy, error on mean and chi-square) – analog mode

E_π	$\langle E_{langaus} \rangle$	$\langle E_{gaus} \rangle$	$\Delta E_{langaus}$	χ^2	dof	ΔE_{total}	$\Delta E'_{total}$
5	107.80	117.72	1.08	610	57	9.97	32.63
10	226.27	231.29	1.28	115	26	5.19	10.91
15	369.63	371.84	1.73	92	11	2.81	8.13
20	511.04	489.83	13.89	6	7	25.35	23.47
25	651.96	635.60	13.43	1	1	21.17	21.17
35	921.68	939.87	9.27	8	31	20.42	10.37
50	1378.77	1397.12	8.33	6	1	20.16	49.38
75	2029.58	2041.74	24.16	1	3	27.04	15.61
100	2949.91	2950.80	25.46	5	3	25.48	32.89

Table 4.4 Hcal response (live energy, error on mean and chi-square) – analog mode

E_π	$\langle E_{langaus} \rangle$	$\langle E_{gaus} \rangle$	σ_{stat}	χ^2	dof	ΔE_{total}	$\Delta E'_{total}$
5	394.54	330.90	1.95	130	27	63.67	139.70
10	868.37	786.99	9.22	153	45	81.90	151.01
15	1365.08	1183.81	13.37	385	43	181.76	543.87
20	1731.91	1543.68	16.21	326	90	188.93	359.58
25	2245.95	2005.73	21.18	160	68	241.15	369.91
35	3171.89	2957.02	35.35	42	73	217.76	165.17
50	4609.02	4370.31	28.42	361	94	240.40	471.10
75	6938.65	6773.38	76.03	92	45	181.91	260.11
100	9493.83	8930.12	19.58	374	70	564.04	1303.77

Table 4.5 Total response (corrected energy, error on mean and chi-square) – analog mode

E_π	$\langle E_{langaus} \rangle$	$\langle E_{gaus} \rangle$	σ_{stat}	χ^2	dof	ΔE_{total}	$\Delta E'_{total}$
5	146.71	134.19	1.67	431	35	12.63	44.33
10	339.95	291.14	5.73	119	41	49.14	83.72
15	494.97	440.01	2.03	362	34	54.99	179.44
20	497.48	472.94	7.41	259	54	25.63	56.12
25	562.03	599.75	6.88	143	51	38.35	64.21
35	801.81	871.00	14.92	72	67	70.78	73.37
50	1396.71	1317.58	7.42	435	86	79.48	178.75
75	2142.34	2111.91	6.58	1238	59	31.13	142.59
100	2898.04	2800.35	19.15	288	80	99.55	188.88

Table 4.6 Energy resolution (converted energy, sigma, errors on mean and sigma and chi-square) – analog mode

E_π	$\langle E_{langaus} \rangle$	$\langle E_{gaus} \rangle$	$\langle \Delta E_{langaus} \rangle$	χ^2	dof	$\sigma_{<E/langaus>}$	$\Delta\sigma_{<E/langaus>}$	$\sigma_{<E/gaus>}$
5	4.15	3.79	0.03	649	86	1.21	0.02	1.60
10	12.77	10.63	0.09	417	89	3.85	0.04	3.63
15	17.15	15.58	0.14	488	42	6.07	0.13	4.43
20	18.59	17.71	0.13	581	73	6.57	0.08	5.45
25	20.79	22.22	0.37	503	50	7.39	0.26	6.12
35	34.66	31.72	0.17	386	64	11.27	0.13	8.28
50	49.45	48.62	0.35	360	74	15.39	0.26	12.27
75	79.12	76.14	0.47	268	49	25.24	0.37	21.07
100	106.83	100.83	0.42	411	84	31.62	0.31	24.54

CHAPTER 5

GEM DIGITAL CALORIMETER PERFORMANCE STUDY

5.1 Purpose of the Study

The purpose of the study is to understand the behavior of the digital technique for GEM based calorimeter for different incident pion energies by counting the number of cells with a minimum energy deposit above the threshold. The digital study is similar to the analog study except that instead of measuring the mean energy $\langle E_{hcal} \rangle$ deposited in Hcal, the mean number of cells hit in Hcal, N_{hcal}, is used to calculate the total energy deposited in the calorimeter.

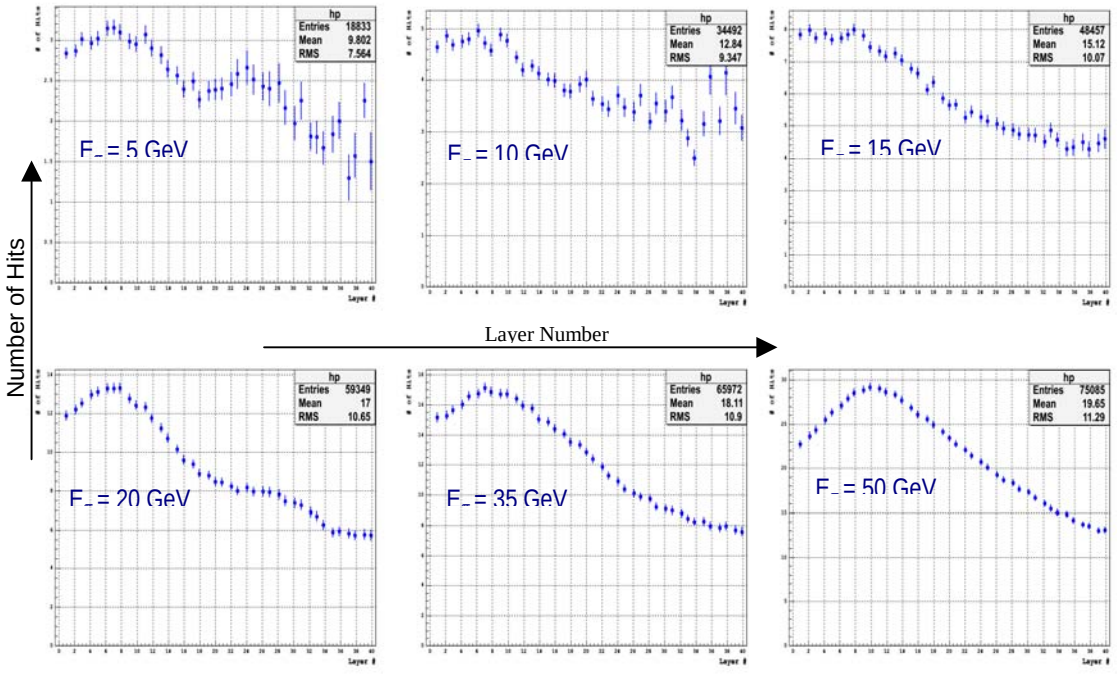

Fig. 5.1 Shower Profile in the Calorimeter for different values of incident energy

It is necessary to determine the response of the digital calorimeter and ascertain that it is linear. To understand the behavior of the calorimeter for different incident pion energies, it is important to study the shower profiles. The number of cells hit is proportional to the number of shower particles in a hadronic shower. The number of shower particles increases linearly as a function of incident pion energy. Therefore it is desirable that the numbers of cells hit also increase linearly with incident pion energy. The longitudinal shower profiles for different incident pion energies are plotted in Fig. 5.1. These plots clearly illustrate that the particle shower penetrates deeper in the calorimeter as the incident particle energy increases.

5.2 Determination of Threshold values using mips

To understand the average behavior of energy deposited in a cell, it is necessary to evaluate the mean energy deposited per cell per event by an energetic pion.

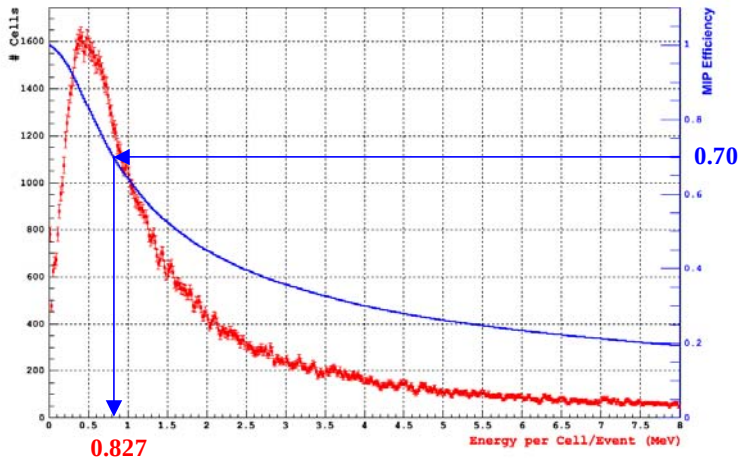

Fig. 5.2 Cell energy deposit (with intrinsic gain included) per cell per event for a 10 GeV pion is shown in red. The plot also shows the mip efficiency curve in blue.

Figure 5.2 illustrates the energy deposited in a cell per event for a 10 GeV pion traversing the Hcal. The distribution of energy lost by the pion per cell is Landau like (shown in red), with a most probable value at (MPV ~ 0.45 MeV) for each cell per event. The pion behaves like a mip. If we measure all the energy deposited in a cell by a charged pion, the threshold is defined to be zero and 100% of the mip information is retained. However, to evaluate the threshold value that corresponds to a certain fraction of the mip information (for example 70% of mip information, 85% of mip information etc.,) one has to determine the threshold energy value in MeV for a cell above which the cell is considered hit. The efficiency curve (shown in blue) can be used to determine this value. The curve is the integral of the Landau distribution normalized to 1.0 (to denote 100% of mip information). The scale on the right axis of the plot shows the mip efficiency. To determine the cutoff value to retain, say, 70% of the mip information, the value of 0.70 is chosen on the scale and the energy corresponding to that value is 0.827 MeV/cell/event, which is the corresponding threshold energy. The digital study can be performed without threshold or with different values of thresholds. Both types of studies are performed in this thesis. The purpose of applying a threshold is to optimize the digital study. Applying a threshold decreases the number of readout cells and thereby readout cost, while keeping only the data that is above noise and background. The threshold values chosen and the corresponding energy cutoff values for this analysis are summarized in Table 5.1

Table 5.1 Threshold values for various mip efficiencies

X, % of MIP Efficiency	Threshold, MeV/cell/event
100	0.000
98	0.103
95	0.222
90	0.330
85	0.470
70	0.827

5.3 Conversion from Number of Hits to Energy

Figure 5.3 shows the relationship between N_{hcal} vs. incident pion energy. The relationship between N_{hcal} and incident pion energy (E_{π}) makes it possible to calculate the energy of the particles if the information of number of cells hit is available. Digital study comprises of counting the number of cells with energy deposited above a threshold value to calculate the energy of the incident particles, knowing that the energy is proportional to the number of cells hit. The scatter plot in Fig. 5.3 shows the number of cells hit in a given event as a function of the incident pion energy. The following observations can be made. Over a certain range, the total number of cells hit in an event increases linearly with incident pion energy. The number of hits for a given incident energy of the pion then reaches a saturation point and flattens out. The saturation effect (also referred to as plateau effect) can be understood by observing that at higher energies the number of cells hit is not directly proportional to the energy deposited, but instead reaches a constant value.

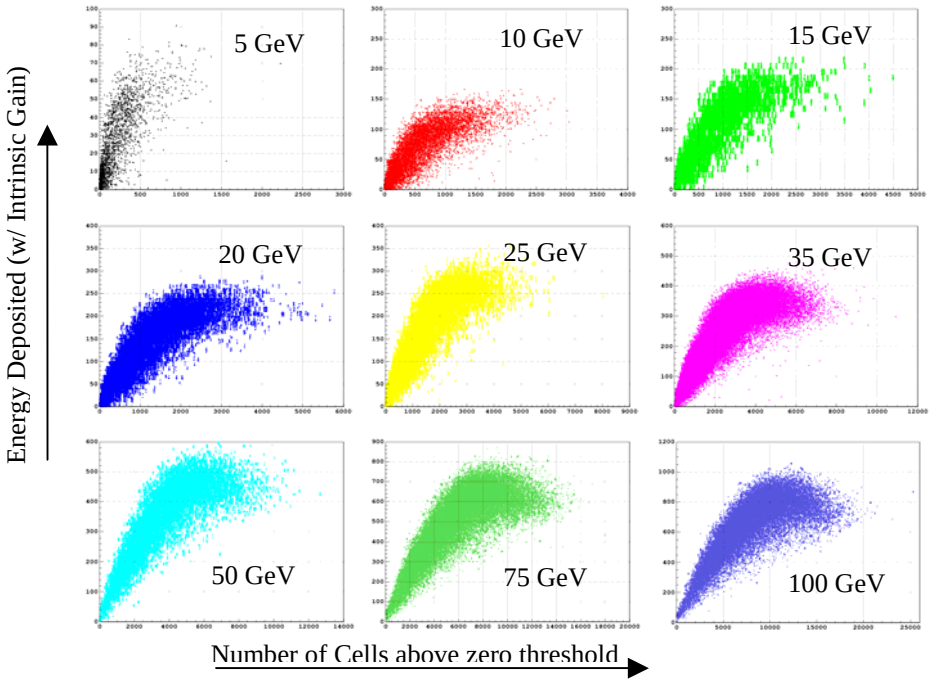

Fig. 5.3 Hits distribution as a function of energy deposited for various values of energy

A given detector has a fixed number of cells and cell sizes in the active medium, and at higher energies some of the cells are hit multiple times by many shower particles. To convert the number of cells hit into a corresponding energy deposit for an event, we can superimpose the scatter plots in Fig. 5.3 and arrive at a measure of the energy dependence of the number of hits. Such a plot is shown in Fig. 5.4. The plot shows the number of hits for all incident energies ranging from 5GeV to 100GeV.

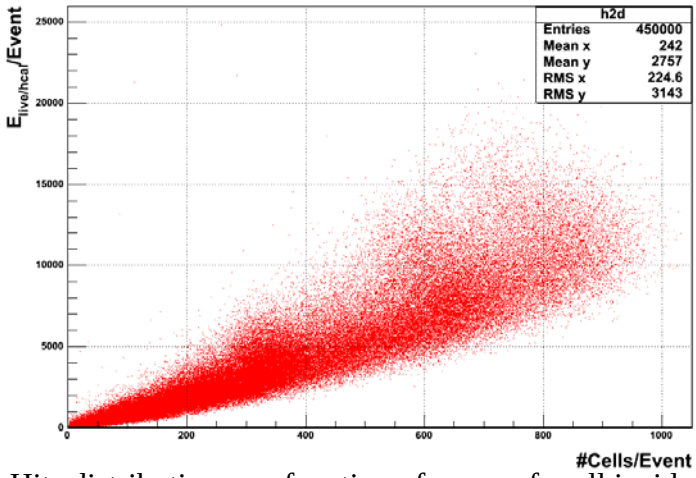

Fig. 5.4 Hits distribution as a function of energy for all incident pion energies.

Two methods are explored to determine the average number of hits. One method considers the plateau effect and the other method does not. If the plateau effect is ignored, a simple linear relation between the average number of hits and energy deposited can be established (although it will not be valid at high cell multiplicity) and the conversion from hits to energy can be calculated in the following manner:

The average energy deposit per cell hit can be determined from the slope. That gives us a measure for converting hits to energy. Linear dependence can be expressed as given in Eq. 5.1.

$$\langle E_{live} \rangle = \frac{dE}{dN} \cdot N_{hcal} \qquad 5.1.$$

where $\langle E_{live} \rangle$ is the average energy deposited in the calorimeter, dE/dN is the slope and N_{hcal} is the number of hits above threshold value in the calorimeter.

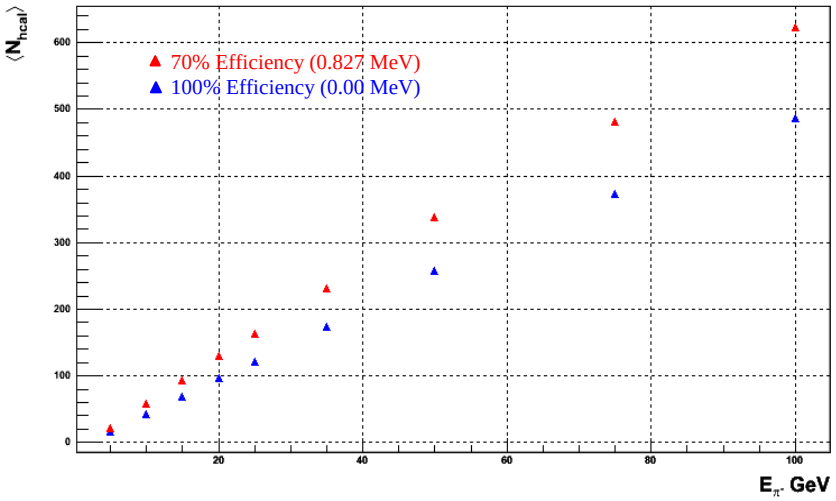

Fig. 5.5 Number of hits as a function of incident energy for two different values of threshold (red: 70% efficiency and blue: 100% efficiency)

The number of hits decreases with the increase in threshold. Figure 5.5 shows this behavior for two different values (70 % and 100 % efficiency) of threshold. We expect the live energy that is measured in the Hcal, to be the same for any given value of threshold. Therefore we expect the value of dE/dN to increase with increasing values of threshold. This is also indicated in Fig. 5.5. As the values of threshold increases, the number of cells above threshold decreases and the factor dE/dN increases. The linear dependence of energy with hits works well only for lower values of energy per cell in a given event. As the energy deposited per cell increases, the plateau effect dominates and the linear dependence of energy with hits is no longer valid. For the digital study in this thesis, this effect is considered and the following

energy dependent parameterization is chosen to compute the energy deposited in a given event using the number of cells hit.

$$\left\langle E_{live/HCAL} \right\rangle = \frac{dE}{dN} \cdot N_{hcal} + \frac{d^2E}{dN^2} \cdot N_{hcal}^2 \qquad 5.2.$$

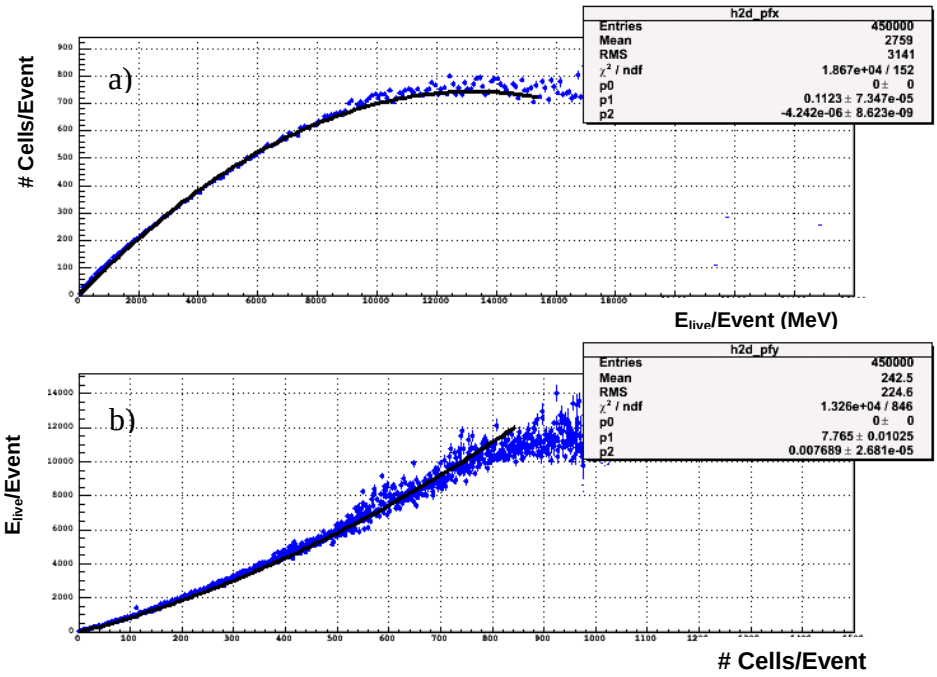

Fig. 5.6 a) Profile plots of Number of Hits vs. Energy and b) Energy vs. Number of Hits. The slope of this plot is used to determine dE/dN and d^2E/dN^2

The slope from Fig. 5.6 b) is obtained from the fit parameters. The fit is constrained to have the functional form given in Eq. 5.2, where the constant term is zero, since there is no electronic noise in the simulation. The profile plot in Fig. 5.6 b) indicates the values of dE/dN and d^2E/dN^2 with the errors for the case of 100% efficiency (with no threshold). The hits to energy parameterization can be written in the form given in Eq. 5.3

$$\left\langle \mathrm{E}_{\mathrm{live/HCAL}} \right\rangle = \left(\mathrm{p}_1 \pm \Delta\mathrm{p}_1\right) \cdot \mathrm{N}_{\mathrm{hcal}} + \left(\mathrm{p}_2 \pm \Delta\mathrm{p}_2\right) \cdot \mathrm{N}_{\mathrm{hcal}}^2 \qquad 5.3.$$

where $p_1 \pm \Delta p_2 = 7.765 \pm 0.010$ and $p_2 \pm \Delta p_2 = 0.0077 \pm 0.00003$.

5.4 Effect of Landau Fluctuation

The first step in the digital analysis is the determination of dE/dN and d^2E/dN^2, where E is the energy deposited in a cell and N is the number of cells. The total deposited energy is then calculated using Eq. 5.3.

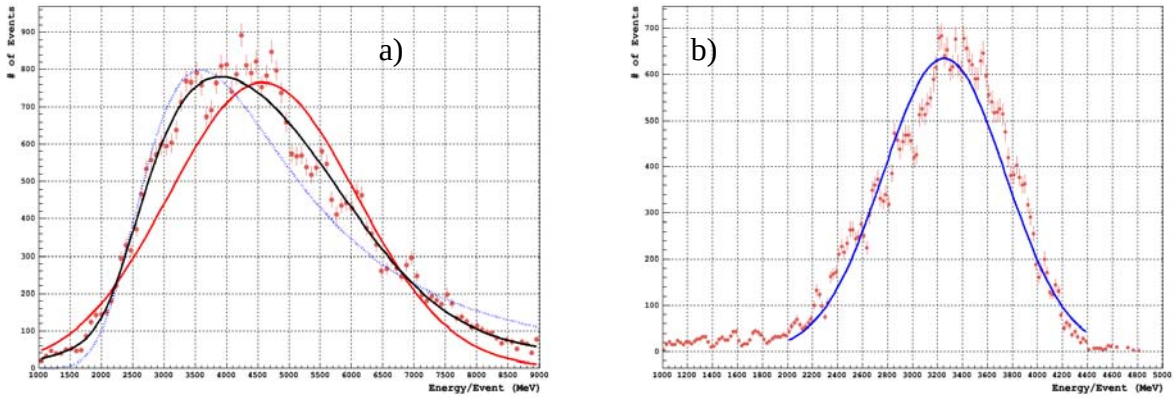

Fig 5.7. (a) Hcal live energy deposit for a 50 GeV pion – analog mode
(b) Hcal live energy deposit for a 50 GeV pion – digital mode

The effect of primary and secondary ionization in the gas volume of GEM based detector is an important factor to consider for digital studies. It is observed that in the digital study, the Landau tail that is observed using the analog approach (caused by statistical fluctuation) is absent. The types of processes that can occur in a gas subjected to an electric field helps us understand the reason for the lack of Landau fluctuation in the digital approach. The particle traversing through a gas medium of GEM detector (Ar: $C0_2$, 70:30 by volume) loses energy by elastic scattering, by excitation and by ionization of the gas atoms or molecules. The energy loss due to elastic scattering is so

small that it does not play a significant role in the operation of the detector. The energy loss due to excitation of the atoms or molecules to higher energy levels occurs, but is also insignificant [47]. So the primary reason for energy loss in GEM is ionization. When an ionizing radiation passes through the gaseous medium, it causes the electrons to be liberated from the atoms or molecules of the medium, thereby leaving positive ions and electrons. The ionization cross-section increases sharply from a threshold value to a peak, and decreases thereafter with increasing incident pion energy [48, 49]. The primary ionization is defined as the number of ionizing collisions per unit length inflicted by the incident pion. Some of the ionized electrons may have sufficient energy to cause further ionization (secondary ionization) when they are accelerated by the electric field in the gas gap. These secondary ionization electrons cause an avalanche effect through the GEM holes, contributing to a large gain factor in the measured signal. In analog study (see Chapter 4 for details), the total energy deposited in a cell is the net charge amplified by the intrinsic gain factor. The total specific ionization, which is the total number of ion-electron pairs that are actually created per unit length, statistically fluctuates and follows the Landau distribution [50]. The amplification causes Landau fluctuation in the total energy deposited in a cell to be broader. Hence we observe a Landau like fluctuation in the total energy deposited in the detector as shown in Fig. 5.7 a). The tail for energy deposit stretches out beyond 9 GeV for a 50 GeV pion. In the digital study, the net electric charge due to all the ionization electrons in a given cell is determined and considered as one hit if it exceeds some threshold. We observe the saturation effect for all incident pion energies and hence the large energy Landau tail is

suppressed, as shown in Fig. 5.7 b). For the same 50GeV incident pion energy, the distribution shows a dramatic cut off at 4GeV. Further, a sufficiently large number of cells are hit over the entire calorimeter to minimize the non-gaussian effect. Counting hits minimizes the large energy deposit that is still left over. At the lower energy end, however, the tail is preserved in both analog and digital studies.

5.5 Procedure for Digital Study

Once the number of hits is converted into energy, the remainder of the procedure for evaluating the energy response and resolution of the calorimeter is identical to that of the analog study (see Chapter 4), with minor modifications in the fitting procedure. A cell is counted as a hit when the energy deposited in the cell is above the threshold value, for different values of threshold. The events are categorized into Ecal and Hcal samples in the same manner as the analog study. For each value of threshold, the Ecal energy is identical, but the Hcal energy is different. If the electromagnetic fraction (f_{EM}) is larger than 85% the event is considered as predominantly EM, as opposed to predominantly hadronic events in which hadronic fraction (f_{HAD}) larger than 85%. Energy distributions are plotted for the EM and Hcal, and the relative weighting factor is determined and the weighting factor is used to compensate for difference in responses between the two detectors. The total energy is computed for each incident pion energy using Eq. 5.4.

$$E_{TOTAL} = \sum_j E_{EM/j} + W \sum_j G \cdot E_{HCAL/j} \qquad 5.4.$$

where G is the intrinsic gain factor and W is the weighting factor.

Systematic errors are determined for live Hcal distributions, detector response and resolution as follows. The total energy distribution for each incident pion energy is fit with only a gaussian to all the bins in the first iteration, unlike the combined Landau and gaussian fit that is used for the analog study. The bins corresponding to 15% of the peak of the above distribution is chosen as the fit range for the constrained gaussian fit in the second iteration. The central value for each incident pion energy is chosen as the mean of the constrained gaussian fit. The difference in the mean value of the energy deposit between the gaussian fit over complete bin range and the constrained gaussian fit is considered as the systematic error. The calorimeter response and energy resolution is obtained in a similar way as described in the analog study. The energy distribution for Hcal before and after the weighting factor is applied and the corrected energy distributions are presented in Appendix E. Figure 5.8 depicts the responses of Ecal and Hcal for a 100% efficiency digital study (with no threshold applied).

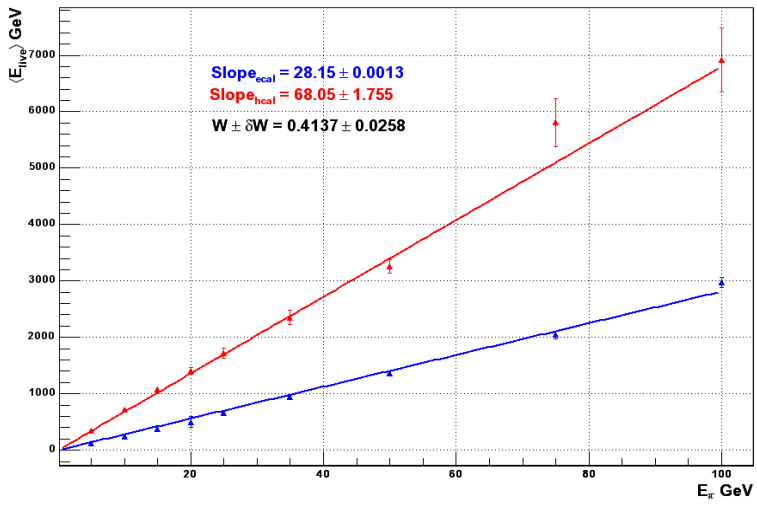

Fig. 5.8 Weighting factor is determined using Ecal and Hcal response.

5.6 Digital Study with Threshold

Application of threshold is an important consideration in keeping the digital readout cost of a calorimeter at a manageable level, since it significantly reduces noise in the readout. Several values of thresholds spanning a wide range of mip efficiencies are chosen in this study. Threshold values and the mip efficiencies corresponding to these threshold values are listed in Table 5.1. The performance of the calorimeter in digital mode is measured. The energy resolution is plotted in Fig. 5.9 shows the performance of the calorimeter in digital mode and no threshold (100% efficiency). The functional form given in Eq. 4.19 is used in fitting the resolution data. The functional form obtained for the fit is given in Eq. 5.5.

$$\frac{\sigma}{E} = \frac{(75.36 \pm 3.25)\%}{\sqrt{E}} + (3.96 \pm 0.54)\% \qquad 5.5.$$

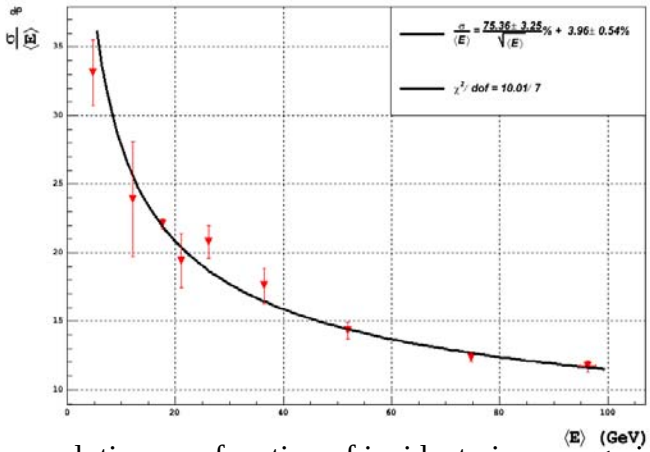

Fig. 5.9 Energy resolution as a function of incident pion energy in digital mode with no threshold applied.

The resolution improves marginally by the application of the threshold. However, increasing the threshold beyond a certain value results in the loss of

information, and the resolution deteriorates. Figure 5.10 summarizes the performance of the calorimeter and lists the energy resolution using various threshold studies performed.

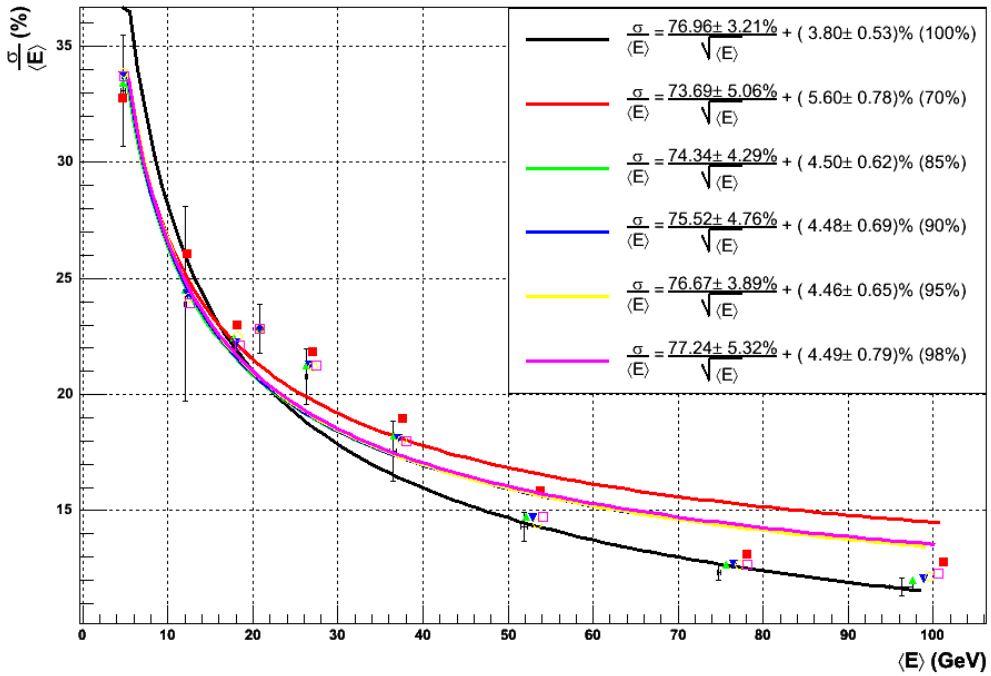

Fig. 5.10 Energy Resolution in a digital mode using various threshold values. The legend indicates the parameters in the fit for various mip efficiencies.

We determine the sampling terms and the constant terms in the resolution and observe the following. The sampling term improves with the value of threshold up to a certain value of threshold and then deteriorates. Further increase in threshold results in an increase of fluctuation, at the lower end of the energy measured, and hence, the sampling term becomes worse. The constant term on the other hand is expected to remain constant, since it describes the overall behavior of the detector at all energies, independent of the incident energy of the pion. Since the detector characteristics remain constant, the constant term in the resolution remains constant. Based on the functional

parameters listed in the legend in Fig. 5.10, it is suggested that a threshold of 98% be used for further digital studies, since the sampling term and the constant term are marginally better than those due to other thresholds.

The energy resolution obtained for each threshold is compared with other studies in analog and digital modes. The resolution in the digital technique is observed to be better than the analog version owing to the reduction of the high-end Landau fluctuations. The resolution studies for TESLA TDR, GEM in analog and digital mode is compared with the K_L^0 studies performed [50] as shown in Fig. 5.11.

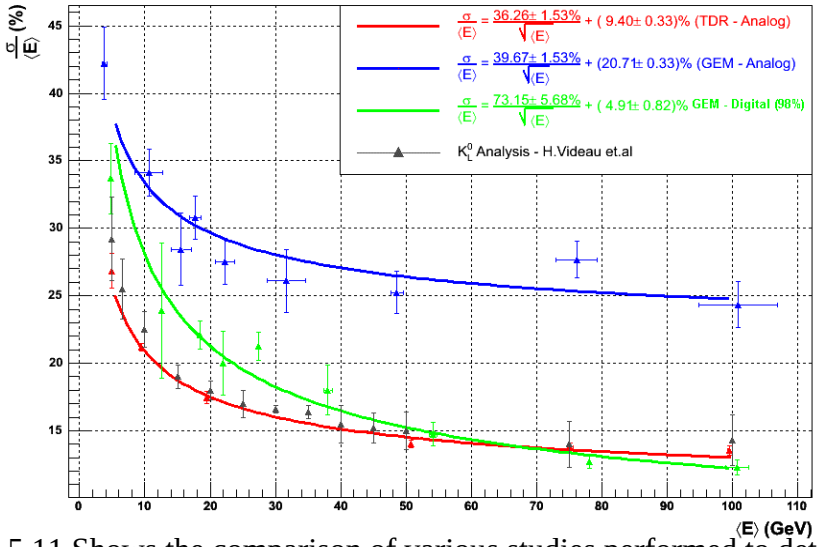

Fig. 5.11 Shows the comparison of various studies performed to determine the calorimeter resolution with TESLA TDR detector, GEM detector in analog and 98% threshold digital mode and K_L^0 analysis of H.Videau et. al.

5.7 GEM- Analog Study with Threshold

The application of a threshold for the analog case is an interesting study to perform to determine how the resolution changes with threshold. A value of threshold was chosen (85%) and the analog threshold study is performed in the following manner.

Instead of counting the average number of hits for a given threshold value in an event, the live energy measured for the same in that event is chosen for the study. This gives us an idea about the fluctuation of energy for a given value of threshold. Once the live energy is obtained, the remainder of the procedure to determine the relative weighting factor, detector response and resolution remain the same as in analog study described previously. The study results are summarized in Tables 5.2 – 5.5.

Table 5.2 Ecal response (live energy, error on mean and chi-square) – digital mode

E_π	$\langle E_{langaus} \rangle$	$\langle E_{gaus} \rangle$	σ_{stat}	χ^2	dof	σ_{total}	$\sigma_{total} \cdot \sqrt{\chi^2/dof}$
5	107.80	117.72	1.08	610	57	9.97	32.63
10	226.27	231.29	1.28	115	26	5.19	10.91
15	369.63	371.84	1.73	92	11	2.81	8.13
20	511.04	489.83	13.89	6	7	25.35	23.47
25	651.96	635.60	13.43	1	1	21.17	21.17
35	921.68	939.87	9.27	8	31	20.42	10.37
50	1378.77	1397.12	8.33	6	1	20.16	49.38
75	2029.58	2041.74	24.16	1	3	27.04	15.61
100	2949.91	2950.80	25.46	5	3	25.48	32.89

In Table 5.2, for incident pion energies corresponding to 35, 50 and 75 GeV pions, due to the lack of statistics at higher energies, the chi-square is not very good (indicated in blue). The number of events that correspond to 85% of energy in the EM fraction decreases with increasing energy of pion.

Table 5.3 Hcal response (live energy, error on mean and chi-square) – digital mode

E_π	$\langle E_{langaus} \rangle$	$\langle E_{gaus} \rangle$	σ_{stat}	χ^2	dof	σ_{total}	$\sigma_{total} \cdot \sqrt{\chi^2/dof}$
5	394.54	330.90	1.95	130	27	63.67	139.70
10	868.37	786.99	9.22	153	45	81.90	151.01
15	1365.08	1183.81	13.37	385	43	181.76	543.87
20	1731.91	1543.68	16.21	326	90	188.93	359.58
25	2245.95	2005.73	21.18	160	68	241.15	369.91
35	3171.89	2957.02	35.35	42	73	217.76	165.17
50	4609.02	4370.31	28.42	361	94	240.40	471.10
75	6938.65	6773.38	76.03	92	45	181.91	260.11
100	9493.83	8930.12	19.58	374	70	564.04	1303.77

Table 5.4 Total response (corrected energy, error on mean and chi-square) – digital mode

E_π	$\langle E_{langaus} \rangle$	$\langle E_{gaus} \rangle$	σ_{stat}	χ^2	dof	σ_{total}	$\sigma_{total} \cdot \sqrt{\chi^2/dof}$
5	146.71	134.19	1.67	431	35	12.63	44.33405
10	339.95	291.14	5.73	119	41	49.14	83.72373
15	494.97	440.01	2.03	362	34	54.99	179.4422
20	497.48	472.94	7.41	259	54	25.63	56.1234
25	562.03	599.75	6.88	143	51	38.35	64.21515
35	801.81	871.00	14.92	72	67	70.78	73.37108
50	1396.71	1317.58	7.42	435	86	79.48	178.7497
75	2142.34	2111.91	6.58	1238	59	31.13	142.5992
100	2898.04	2800.35	19.15	288	80	99.55	188.879

Table 5.5 Energy resolution (converted energy, sigma, errors on mean and sigma and chi-square) – digital mode

E_π	$\langle E_{langaus} \rangle$	$\langle E_{gaus} \rangle$	$\langle \Delta E_{langaus} \rangle$	χ^2	dof	$\sigma_{<E/langaus>}$	$\sigma_{<E/gaus>}$	$\Delta\sigma_{<E/langaus>}$
5	4.15	3.79	0.03	649	86	1.21	1.60	0.02
10	12.77	10.63	0.09	417	89	3.85	3.63	0.04
15	17.15	15.58	0.14	488	42	6.07	4.43	0.13
20	18.59	17.71	0.13	581	73	6.57	5.45	0.08
25	20.79	22.22	0.37	503	50	7.39	6.12	0.26
35	34.66	31.72	0.17	386	64	11.27	8.28	0.13
50	49.45	48.62	0.35	360	74	15.39	12.27	0.26
75	79.12	76.14	0.47	268	49	25.24	21.07	0.37
100	106.83	100.83	0.42	411	84	31.62	24.54	0.31

CHAPTER 6

ENERGY FLOW ALGORITHM DEVELOPMENT

6.1 Motivation

One of the physics goals for future high energy physics experiments is to significantly improve the jet energy resolution. Improvement in jet energy measured using conventional calorimeters requires higher granularity of calorimeter cells, making their read out cost prohibitive. For hadronic jets (or showers), the energy and position resolution are limited by several phenomena as discussed in section 3.2.4. One way to achieve the goal of improved hadronic jet energy resolution is the use of Digital Calorimetry [51] in conjunction with a technique developed by the ALEPH [52] collaboration called the Energy Flow Technique.

To elucidate with an example, consider the jet energy measurement from decay of Higgs particle involving final state jets as illustrated in Fig. 6.1.

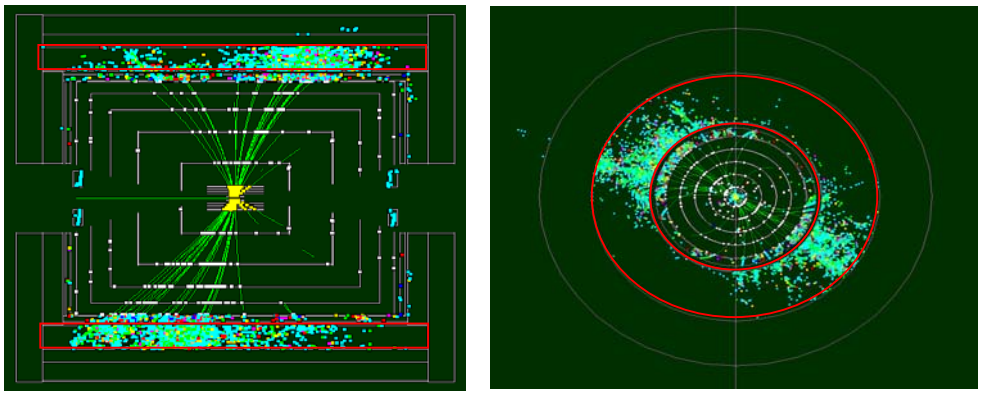

Fig 6.1 Simulated event representing $e^+e^- \rightarrow h\,Z \rightarrow bbcc$ 4-jet final state with M_h=115 GeV/c^2 and $\sqrt{s}$ =500 GeV. The hadronic calorimeter is highlighted in red in the side view (left) and end view (right). Courtesy of H.Videau et al. [53]

The final state of the e^+e^- interaction is the presence of four jets. The Z vector boson undergoes hadronic decay mode into two c-quark jets and the Higgs decays into two b-quark jets. To reconstruct the mass of the Z with sufficient accuracy and distinguish it from the mass of the W boson, the dijet mass must be measured to a precision of ~3 GeV or, in terms of jet energy resolution it can be expressed in the form of Eq. 6.1:

$$\sigma(E) \approx 0.3\sqrt{E} \qquad 6.1.$$

where E is expressed in GeV. This low a value of jet energy resolution has not been achieved in any existing calorimeter [53]. Using a Digital Hadron Calorimeter (DHCal) to measure jet energy in conjunction with the Energy Flow Technique could be an economical solution to achieve good energy resolution for future experiments. Section 6.1.1 describes the basic concept of energy flow technique.

6.1.1 Energy Flow Concept

The basic concept of the Energy Flow Algorithm for jet energy measurement is to use the tracking detectors for the measurement of charged particle momenta and the calorimeter for neutral particle energy measurement. It is therefore essential to identify energy deposition in the calorimeter arising from individual particles in the jet. The first prerequisite for this is to build a calorimeter with fine enough segmentation to separate the particle showers. The next is the ability to associate the hit cells in the calorimeter into clusters, which can then be identified with the particles in the jet. If we denote the

energy of a jet (E_{jet}) to be the sum of the energy of clusters that are in the calorimeter ($\sum_j E_{c/j}^{cal}$) it can be represented as Eq. 6.2.

$$E_{jet} = \sum_j E_{c/j}^{cal} \qquad 6.2.$$

There are a number of existing approaches to construct a cluster, for example JADE [54,55], Durham [56], which are very successful in reconstructing jets. However, the energy flow approach is slightly different from these. The energy (E_{jet}) of a jet is written as a sum of its components as shown in Eq. 6.3.

$$E_{jet} = \sum_j \vec{p}_{j/ch} + \sum_j E_{neu/j}^{cal} \qquad 6.3.$$

where $\sum_j \vec{p}_{j/ch}$ represents vector sum of the momenta of the charged tracks measured in the tracker and $\sum_j E_{neu/j}^{cal}$ represents the remainder of the energy which is due to the neutral particles measured in the calorimeter. The argument for doing so is as follows. The particles in the jet are typically comprised of charged hadrons (about 60% of the jet energy), neutral hadrons (about 10% of jet energy) and EM particles (about 30% of the jet energy). If the track reconstruction using the tracking device is efficiently performed, the remainder of the task is to efficiently cluster related calorimeter cells and associate them with the particle, which initiated the shower. The energy of the calorimeter clusters that are associated with charged particles in the tracking device can be subtracted and replaced with momenta measured in the tracker, since the tracking detectors measure their momenta better. Only clusters unassociated with charged tracks

will be used in the jet finding algorithm to measure remaining neutral particle energy. In principle, these will only be due to EM particles and neutral hadrons. The EM particles are well measured in the EM calorimeter. Reconstructing the energy deposits originating from neutral hadrons is the most difficult task, and even though this class of particle represents a small fraction of the jet's energy, it represents an important part of the systematic uncertainty in the jet energy reconstruction.

6.2 Analysis of $e^+e^- \to t\bar{t} \to 6\,jets$

A good example to study multi-jet final state events in the e^+e^- collisions is the production of top pair, which may decay into 6-jet final state. The purpose of studying multi-jet final state events is to characterize a typical jet by defining its typical particle composition and the distribution of energy of the particles in a jet. This leads us to define a few parameters in a typical Energy Flow Algorithm (EFA) like the size of a cone (if the algorithm uses a cone based), relative separation of particles in a jet, the average energy of the particles and their types etc., The parameters can then be used in developing the EFA. Appendix F shows an example program to generate the events of specific interest for the EFA study.

6.2.1 Jet Definition

The results of the hadronization of a system of partons that result from fragmentation of the primary quark are a combination of photons, leptons and colorless hadrons, which can be considered as a jet to a first approximation. As the first step, it is necessary to identify one of the primary quarks that result in a jet. The event record contains information about the particles produced in the current event: flavors,

momenta, event history and production vertices. So the primary task is to associate the final state particles in a given event with a quark from which they originated. This can be done by using the event history and tracing back all final state particles to their respective parent quarks. Once this is done, the final state particles corresponding to a given quark form the jet. This can be very tedious task. In real events, unlike Pythia MC events, there is no way to associate every particle with its parent quark. For the study conducted in this thesis, the jet is defined by a simple cone of a given size (ΔR_{qf}) around the quark as given in Eq. 6.4.

$$\Delta R_{qf} \leq \sqrt{\left(\eta_q - \eta_f\right)^2 + \left(\varphi_q - \varphi_f\right)^2} \qquad 6.4.$$

ΔR_{qf} is the separation of the final state particle (denoted by subscript *f*) with a quark (denoted by subscript *q*) in the angular space and is also called the radius of the cone. If the value of ΔR_{qf} is specified, (ΔR_{qf} = 0.5 for this analysis), the final state particle is included in the jet if it is deposited within this cone. The cone center is defined as $C_q \equiv \left(\eta_q, \varphi_q\right)$ and all particles that belong to the cone satisfy the condition given in Eq. 6.5.

$$C_f \equiv \left(\eta_f, \varphi_f\right) \in C_q \quad iff \quad \Delta R_{qf} \leq 0.5 \qquad 6.5.$$

Once a jet is defined, the energy distribution and the angular separation of the particles in a jet can be determined. The energy distribution in an event can also be plotted as a function of angular variables (η, φ) as an event display.

6.2.2 Energy Distribution of Particles in a Jet

The jet typically consists of neutral and charged hadrons and electromagnetic particles. In the reaction $e^+e^- \to t\bar{t} \to 6\,jets$ at $\sqrt{s} = 1.0\,TeV$, the energy distribution of various particles in the jet is shown in Fig. 6.4. Charged pions are the majority of the particles. The average energy of the charged pions is measured to be 7.5 GeV.

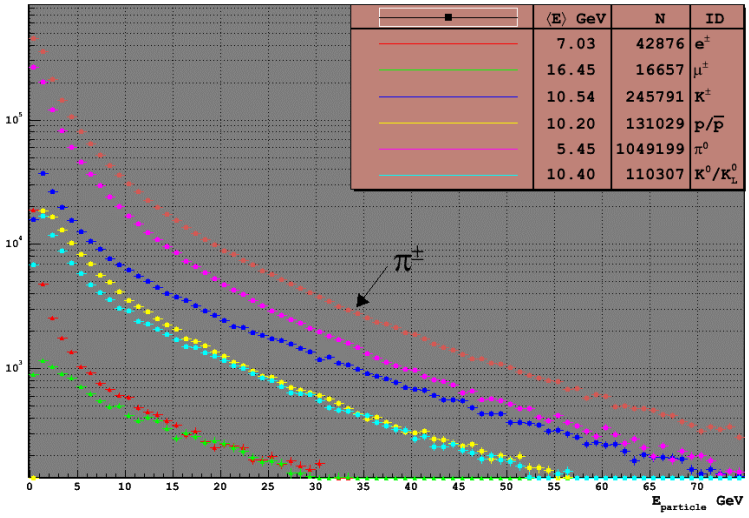

Fig 6.4 Energy distribution of particles in a jet is shown. The particle IDs, mean energy and number of particles are shown in the legend.

The study of particle composition of the jet is important for EFA. Hadronic showers are more complicated than electromagnetic showers. Complication arises due to many processes that can occur at the particle level because of the strong interaction between the incident hadron and the matter in the calorimeter. Some of the processes that are produced in the hadronic cascade, in particular π^0s and ηs, decay through electromagnetic interaction primarily into photons: $\pi^0, \eta \to \gamma\,\gamma$. On an average, ~ 30% of the energy is the electromagnetic component [57].

Figure 6.5 shows an event display for the reaction $e^+e^- \to t\bar{t} \to 6\,jets$ for two events chosen at random among the three thousand events that were generated. The peaks correspond to shower particles.

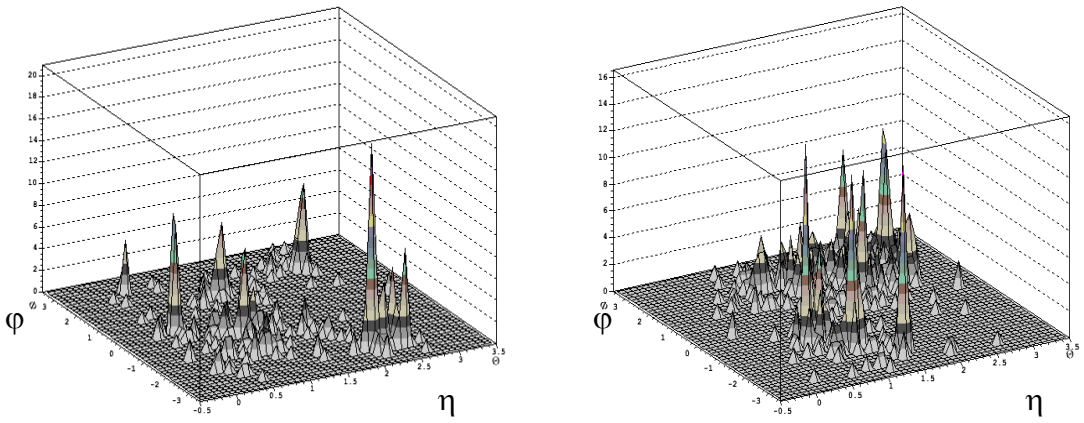

Fig 6.5 Event display of $e^+e^- \to t\bar{t} \to 6\,jets$ for two different events.

The event display gives the reader an idea about the number of jets that may occur in that event and their behavior. Jets consist of EM and hadronic particles, which deposit energy through the process of showering. The hadronic showers tend to be more spread out, and vary largely from event to event.

6.2.3 Fractional Energy Distribution of Particles in a Jet

The fraction of energy contained in the EM particles, the neutral hadrons and the charged hadrons are shown in Fig. 6.6. The plot shows that about 70% of the jet energy is carried by charged hadrons. The EM particles carry about 27% of the energy. Only a small fraction of the energy (~ 3%) is carried by the neutral hadrons that are measured in the hadronic calorimeter.

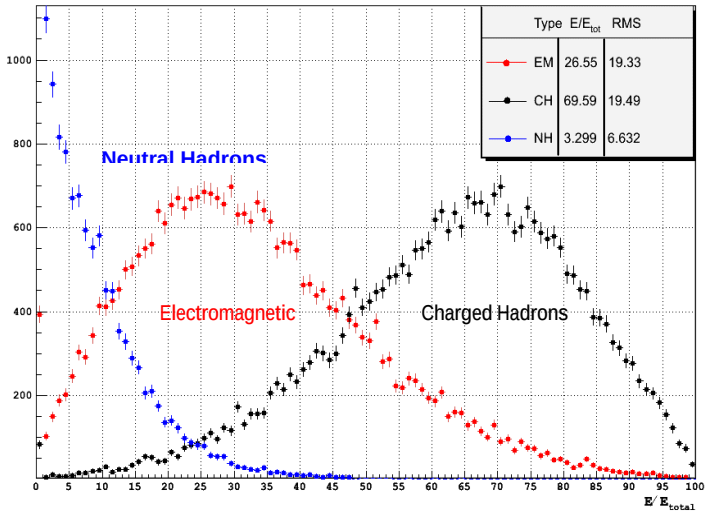

Fig. 6.6 Fractional Energy Distribution of particles in a jet as a fraction of the total energy of the jet.

6.2.4 Angular Separation of Particles in a Jet

Another measure that is useful in the EFA is the average angular separation of the particles within a jet relative to each other. Since the cone size is chosen to be 0.5 for the study, the relative separation shows a drop, at the cone boundary, as expected. This is shown in Fig. 6.7. It also gives us the average particle separation for the design of the algorithm. The average particle separation for a jet in this case is $\langle \Delta R \rangle \sim 0.25$. The plot also shows that angular separation rises rapidly down to $\Delta R \sim 0.05$ and drops quickly as ΔR reduces. This drop in the ΔR is due to an artificial cut off for the fragmentation and hadronization in the Pandora-pythia event generation.

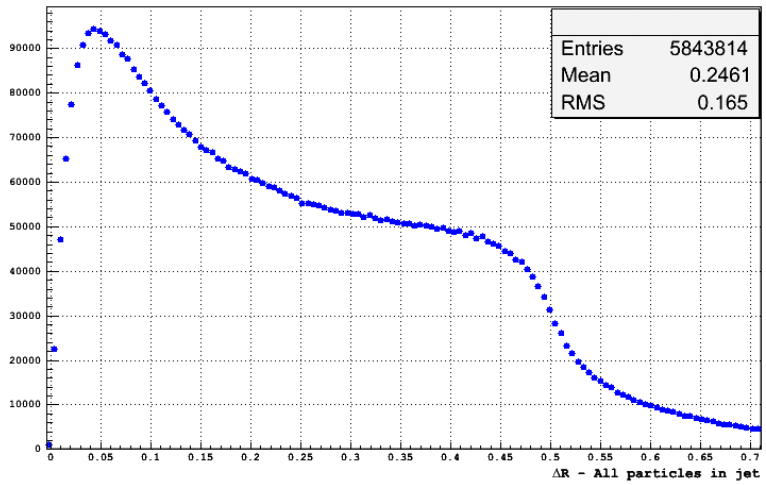

Fig. 6.7 Average separation of particles in a jet.

6.3 Energy Flow Study with Single Pion Events

The hadronic component of a jet primarily consists of pions, kaons, neutrons and protons. Negatively charged pion with $\langle E_\pi \rangle = 7.5\,GeV$ is chosen for the study based on the study described in section 6.2, and one thousand event samples were generated using Mokka [29] single particle gun utility. Details of event generation using the particle gun utility in Mokka can be found in Appendix F.

The goal of this study is to associate the charged energy cluster in the Hcal with the track in the tracker for subsequent energy subtraction. Since a single charged pion is chosen, all the energy deposited in the calorimeter is due to that pion and a performance measure can be established by how well the association is made. Three methods are

chosen to study the association of the charged energy cluster with the charged track. These methods are explained in section 6.3.1.

6.3.1 Performance of Cluster Centroid Finding

The pion shower proceeds in the lateral and longitudinal directions in the calorimeter. The method aims at finding the centroid of the shower and extrapolating the fit for the centroid of the shower in the calorimeter to the tracking chamber. The charged particle leaves a track and the information regarding the momentum and the position of the particle in the tracking system is available. For the performance measure, the difference between the extrapolated calorimeter cluster and the position of the charged track in the last layer of the tracker is chosen.

The centroid is measured in the calorimeter as follows. The hit distribution in each layer is inspected. The position of the hits in each cell in a layer is weighted by the energy deposition in the cell and the energy-weighted center for each layer is computed using Eq. 6.2. The energy-weighted center is defined in Eq. 6.6. $C_{ij} \equiv (\theta_{ij}, \phi_{ij}, E_{ij})$ is the position and energy deposited in cell *j* in layer *i*.

$$\left.\begin{array}{ll} \overline{\theta_i} = \dfrac{\sum_{j=1}^{n} E_{ij}\theta_{ij}}{\sum_{j=1}^{n} E_{ij}} & \overline{\phi_i} = \dfrac{\sum_{j=1}^{n} E_{ij}\phi_{ij}}{\sum_{j=1}^{n} E_{ij}} \\ & 1 \le \mathrm{j} \le \mathrm{n},\ \mathrm{n} > 1 \\ & \mathrm{n}: \text{Number of hits in layer i} \\ & 1 \le \mathrm{i} \le 40\ (\text{Forty layers in Hcal}) \end{array}\right\} \qquad 6.6.$$

For each layer of the calorimeter, the standard deviation based on energy-weighted centers are determined using Eq. 6.7.

$$\sigma_{\overline{\theta_i}} = \sqrt{\frac{\sum_{j=1}^{n}\left(\overline{\theta_i} - \theta_j\right)^2}{n-1}} \qquad \sigma_{\overline{\phi_i}} = \sqrt{\frac{\sum_{j=1}^{n}\left(\overline{\phi_i} - \phi_j\right)^2}{n-1}} \tag{6.7.}$$

If Poisson statistics are assumed for the hit-distribution in each layer, the error on the energy-weighted center can be expressed as Eq. 6.8.

$$\Delta\overline{\theta_i} = \frac{\sigma_{\overline{\theta_i}}}{\sqrt{n}} \qquad \Delta\overline{\phi_i} = \frac{\sigma_{\overline{\phi_i}}}{\sqrt{n}} \tag{6.8.}$$

The energy-weighted center in each layer is fit using the functional forms given in Eqs. 6.9 and 6.10 to obtain the centroid of the shower.

$$\overline{\theta_i} = \left(a \pm \Delta a\right) \cdot R_i + \left(b \pm \Delta b\right) \tag{6.9.}$$

$$\overline{\phi_i} = \left(c \pm \Delta c\right) \cdot R_i + \left(d \pm \Delta d\right) \tag{6.10.}$$

where R_i is the radial distance of layer i from the center of the detector. $\left(a \pm \Delta a\right), \left(b \pm \Delta b\right), \left(c \pm \Delta c\right)$ *and* $\left(d \pm \Delta d\right)$ are the parameters obtained from the fit. The centroid is extrapolated to the last layer of the tracking chamber using these parameters. The difference in the position of the track and the extrapolated centroid determines the precision with which the matching is done. This method can be treated as the analog method of finding the centroid, since we are using the energy deposited in each cell into account. The hits-weighted centroid can similarly be defined as the numerical average of the hit positions in each layer and is given in Eq. 6.11.

$$\overline{\theta_i} = \frac{\sum_{j=1}^{n}\theta_{ij}}{n} \qquad \overline{\phi_i} = \frac{\sum_{j=1}^{n}\phi_{ij}}{n} \tag{6.11.}$$

The hits-weighted method can be treated as a digital approach, since the energy deposited in a cell is not used to compute the center. In the digital approach, we can also define the density of each cell as a measure of identifying the energy clusters in a given layer. If a cell that is hit has many neighbors that are close to it, then its density is higher than a cell, which has neighbors distant from it. The density of a hit-cell can be defined as being inversely proportional to the sum of the distance of that cell from all the neighboring hit-cells in that layer. The density-weighted center is computed and used to compare its position with that of the track in the tracking chamber. If d_i is the density of cell *i* and $R_{ij} = \sqrt{(\theta_i - \theta_j)^2 + (\varphi_i - \varphi_j)^2}$ is the distance between cell *i* and cell *j* that are hit in that layer, the density and the density-weighted center can be defined by Eq. 6.12.

$$d_i = \sum_{j=1, j\neq i}^{n} \frac{1}{R_{ij}} \quad \overline{\theta_i} = \frac{\sum_{j=1}^{n} d_{ij}\theta_{ij}}{n} \quad \overline{\phi_i} = \frac{\sum_{j=1}^{n} d_{ij}\phi_{ij}}{n} \qquad 6.12.$$

The results of the matching of the track with the extrapolated centroid are shown in Fig. 6.6. The values of $\Delta\theta = \theta_{tpc} - \theta_{cal}$ *and* $\Delta\phi = \phi_{tpc} - \phi_{cal}$ determine how precise the matching is done. The values of Δθ and Δϕ for the three methods are summarized in Table 6.1.

Table 6.1 Comparison of Δθ and Δϕ for different methods to determine centroid.

	Hits-weighted	Energy-weighted	Density-weighted
$\langle\Delta\theta\rangle$	(1.24 ± 0.29) 10^{-3}	(4.38 ± 0.20) 10^{-3}	(-7.55 ± 0.38) 10^{-4}
$\langle\Delta\phi\rangle$	(-2.93 ± 0.57) 10^{-4}	(-6.34 ± 0.86) 10^{-4}	(1.23 ± 0.11) 10^{-4}

The density-weighted method gives a better value of $\Delta\theta$ and $\Delta\phi$ compared to the energy-weighted method and the hits-weighted method. This method is chosen for analysis of two pions using EFA.

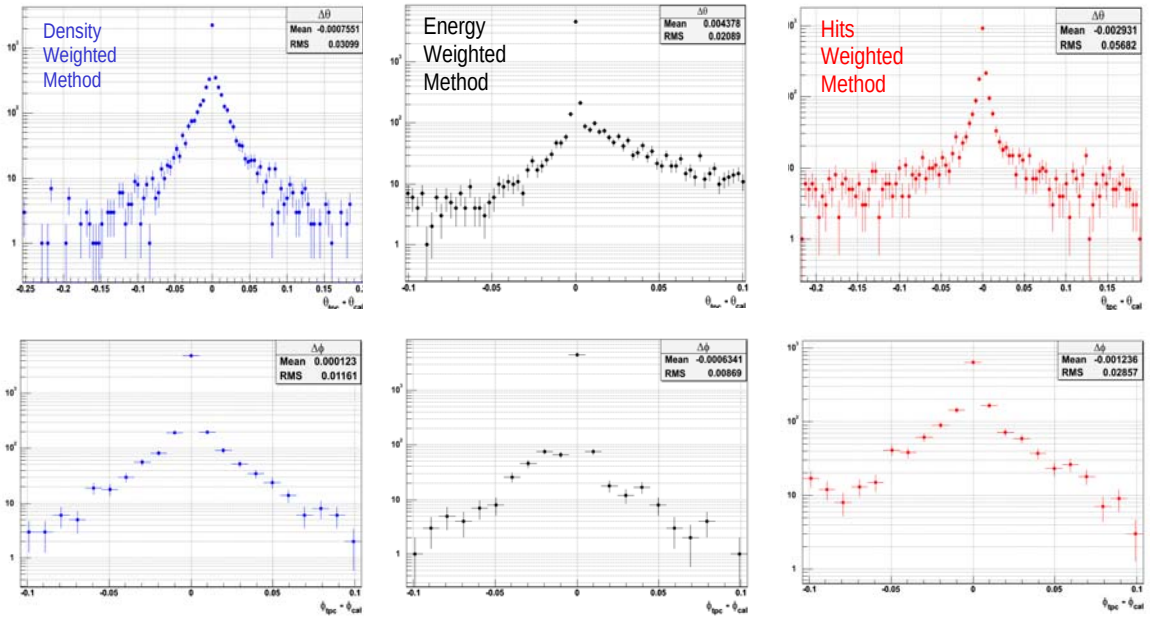

Fig. 6.6 Centroid using 1) Density-weighted Method 2) Energy-weighted Method and 3) Hits-weighted Method matched with the tracker hit position.

6.4 Generation of Two - Pion Events

For the performance study using two charged pions, the separation between the pions was chosen to be half the average distance between the particles in a jet with R=0.25 being the average separation (see section 6.2.3). The two pions are separated by a distance of R=0.12 and each had a momentum of 7.5 GeV for the study. One thousand events with two negatively charged pions are generated for the study. The density-

weighted method is chosen as the procedure for evaluating the centroid of the pions. The EFA is outlined in section 6.6.

6.5 EFA Procedure for Two - Pion Case

The procedure to evaluate the associated energy corresponding to a charged track in the two-pion case is explained in this section. The algorithm can be divided into two iterations. The following procedure is followed for each pion for every event:

First Iteration:

1. In a given event, scan the tracking hits information from the tracking output and identify the hits layer by layer (for more details of the tracking hits format, refer section 4.2.3. and section 4.4). The tracking hits information for both the pions is stored in the output. Since the pions have a small separation ($\Delta R \sim 0.12$) between them, it is possible uniquely identify hits and associate it with a particular pion in the tracker using particle ID information.

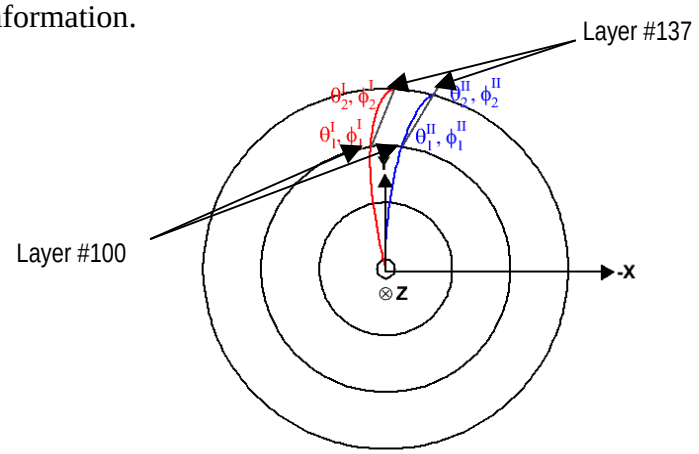

Fig. 6.7 Path of the two pions in the tracker and the hits corresponding to two layers.

Since the negatively charged pions are projected along +Y direction in a magnetic field, B = 5 Tesla along +Z direction (refer Appendix F for details of particle gun utility), they experience a force and are deflected in the transverse (XY) plane along –X direction. This is shown in Fig. 6.7. The $(\theta,\varphi)_{tpc}$ corresponding to the hits in layers - #100 and #137 are evaluated. Figure 6.7 also shows the $(\theta,\phi)_{tpc}$ for the two pions. The superscripts (I and II) indicate the identity of the pions and the subscripts indicate the position of the measured track (1 for layer #100 and 2 for layer #137). The next step is to extrapolate the track. An approximate way to do this is to parameterize the hits in the two layers using a straight-line fit. The functional form chosen to express the relationship between the radius measured from the center of the detector to a given layer in the tracker (R_{tpc}) and the $(\theta,\phi)_{tpc}$ can be expressed as given in Eq. 6.13

$$\left.\begin{aligned}\theta &= \left(A_1 \pm \Delta A_1\right)\cdot R_{tpc} + \left(B_1 \pm \Delta B_1\right)\\ \phi &= \left(A_2 \pm \Delta A_2\right)\cdot R_{tpc} + \left(B_2 \pm \Delta B_2\right)\end{aligned}\right\} \qquad 6.13.$$

The separation distance between the two pions is computed using Eq. 6.14 and half the separation distance (r_c^{tpc}) is used as a measure to initially separate the pion showers in the calorimeter.

$$r_c^{tpc} = \Delta R_{tpc}/2 \quad \Delta R_{tpc} = \sqrt{\left(\theta_1^{tpc} - \theta_2^{tpc}\right)^2 + \left(\varphi_1^{tpc} - \varphi_2^{tpc}\right)^2} \qquad 6.14.$$

For each layer in the calorimeter, the hits position (X, Y, Z) of each cell in that layer is expressed as (θ,ϕ) and the density of each cell is computed using

Eq. 6.12. The track from the tracker is extrapolated to each layer in the calorimeter using the functional form of Eq. 6.13. The highest density cell in each layer is identified and associated with the extrapolated track. The highest density cell belongs a given pion if its relative distance from the extrapolated track position is less than the separation distance (r_c^{tpc}).

2. The average calorimeter position for each pion is computed based on the highest density information associated with that pion. The average calorimeter position is denoted as $\left(\langle\Theta\rangle,\langle\Phi\rangle\right)_{cal}$ and is given by Eq. 6.15.

$$\langle\Theta\rangle_{cal} = \frac{\sum_{i}^{M_1} \theta_{ij}^{\max}}{M_1} \qquad \langle\Phi\rangle_{cal} = \frac{\sum_{i}^{M_1} \varphi_{ij}^{\max}}{M_1} \qquad \text{Eq. 6.15}$$

The numerical average computed using Eq. 6.15 is considered as the calorimeter centroid for the first iteration. This step marks the end of first iteration of the algorithm.

Second Iteration:

3. Using the centroid information from the first iteration, separation between the centroids for the two pions, r_c^{cal} , is computed. The distance measure is defined as half the distance of separation between the centroids and is expressed in Eq. 6.16. It forms the radius of the cone for associating hits into clusters.

$$r_c^{cal} = \Delta R^{cal}/2 \text{ , where } \Delta R^{cal} = \sqrt{\left(\Theta_1^{cal} - \Theta_2^{cal}\right)^2 + \left(\Phi_1^{cal} - \Phi_2^{cal}\right)^2} \qquad 6.16.$$

As a second pass through the calorimeter layers, the density-weighted center for both the pions is computed using r_c^{cal} as the cone radius and $\left(\langle\Theta\rangle,\langle\Phi\rangle\right)_{cal}$ as the center of the cone and including all the hits within the cone to compute the density-weighted center.

4. The error on the density-weighted center in each layer is computed in a similar manner as was computed in the single pion EFA, using Eqs. 6.7 and 6.8 and for each pion, a functional form similar to the Eq. 6.9 is evaluated by fitting a straight line through the density-weighted centers to obtain the centroid.
5. The cone radius (r_2^{cal}) is recomputed with the new centroids obtained from the second pass using Eq. 6.16. The hits are grouped into clusters based on their distance from a centroid. The distance of a cell from a centroid (which corresponds to a pion) is computed and if it is smaller than r_2^{cal}, the cell is marked as belonging to that pion. If the cell does not belong to either of the pions based on this criteria, then it is considered as a leftover. For each event the number of hits for both pions and the leftover hits are stored for further analysis.
6. Using the centroid information obtained from step 5, and using a similar approach, the hits corresponding to the first and second pions and the leftover hits is computed for the electromagnetic calorimeter. This step marks the end of the second iteration.

Conversion of calorimeter hits to energy using digital approach.

7. The digital approach to conversion of hits to energy is explained in section 5.4. The energy corresponding to a given number of hits can be evaluated if the following parameters are known:

    - W: The weighting factor as the ration of response of Ecal to Hcal.
    - G: The intrinsic gain factor for the Hcal.
    - dE/dN and d^2E/dN^2 to convert hits to energy (see section 5.3 and Eq. 5.2 for detailed explanation of these parameters)
    - SF, the sampling fraction to obtain the converted energy

    These parameters can be obtained from the analysis of the calorimeter in a digital mode with a given threshold. For this analysis, the parameters that are chosen are given in Table. 6.2.

Table 6.2 Input parameters for digital study

W	G	dE/dN	d^2E/dN^2	SF	Efficiency
0.3927	3500	9.432	0.004	27.95	98%

The live energy is obtained from the Eq. 6.17

$$E_{live/hcal} = \sum_j E_{Ecal}^j + W \cdot \sum_j G \cdot E_{hcal}^j \qquad 6.17.$$

$E_{live/hcal}$ is the live energy measured for a given pion in the calorimeter

$\sum_j E_{Ecal}^j$ is the live energy measured in the Ecal.

$\sum_j E_{Hcal}^j$ is the total energy measured in the Hcal

The live energy measured in the Ecal and Hcal can be obtained using Eqs. 6.18 and 6.19. The number of hits with in the cone for a given pion in Ecal and Hcal are denoted as $N_{j/ecal}$ and $N_{j/hcal}$ respectively.

$$\sum_j E_{Ecal}^j = \{dE/dN\}N_{j/ecal} + \{d^2E/dN^2\}N_{j/ecal}^2 \qquad 6.18.$$

$$\sum_j E_{hcal}^j = \{dE/dN\}N_{j/hcal} + \{d^2E/dN^2\}N_{j/hcal}^2 \qquad 6.19.$$

6.6 EFA with Two - Pions - Performance Summary

6.6.1 Track Matching using Calorimeter Centroid from First Iteration

The calorimeter centroid obtained in the first iteration is extrapolated to the tracking chamber and the results of the track match are shown in Fig. 6.8.

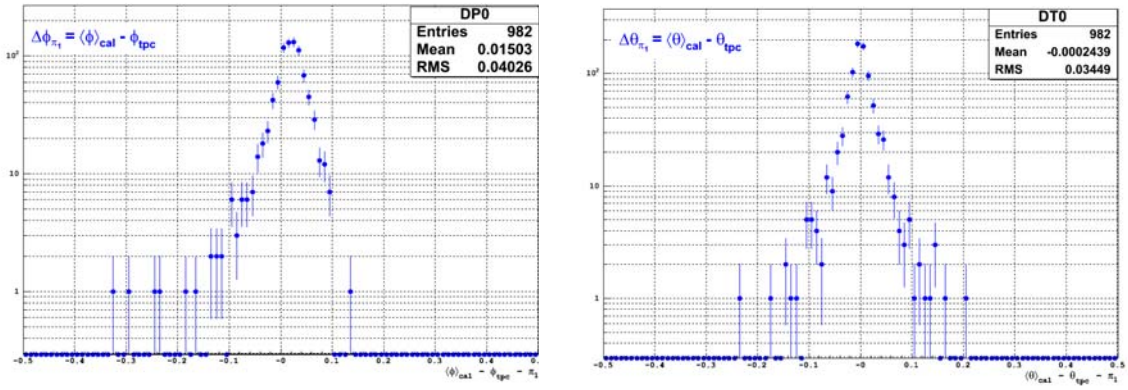

Fig. 6.8 The track match with the calorimeter centroid using density-weighted method.

The values of $\Delta\theta = \langle\Theta\rangle_{cal} - \theta_{tpc}$ *and* $\Delta\phi = \langle\Phi\rangle_{cal} - \phi_{tpc}$ determine how precise the matching is done. The $\Delta\phi$ for the track match can be improved, if the deflection of the pions in the transverse plane is treated with more precision by using a parameterization that treats the deflection of the pions in the magnetic field more precisely. In this study a linear approximation using two nearby layers near the exit point of the tracking chamber is chosen as explained in Step 1 (Eq. 6.13).

6.6.2 Energy of the Calorimeter Cluster for a Pion after Second Iteration

The converted energy for the cone for a pion after applying the digital method described in Step 7 is illustrated in Fig. 6.9. The plot shows that the converted energy of one of the pions is 7.4 ± 0.3 GeV which is comparable with the incident energy of the pion which is 7.5 GeV. The converted energy for the other pion is 6.2 ± 0.4 GeV, which is less than the expected value. The converted energy obtained is subtracted fro the calorimeter and is replaced by the track momentum in the EFA.

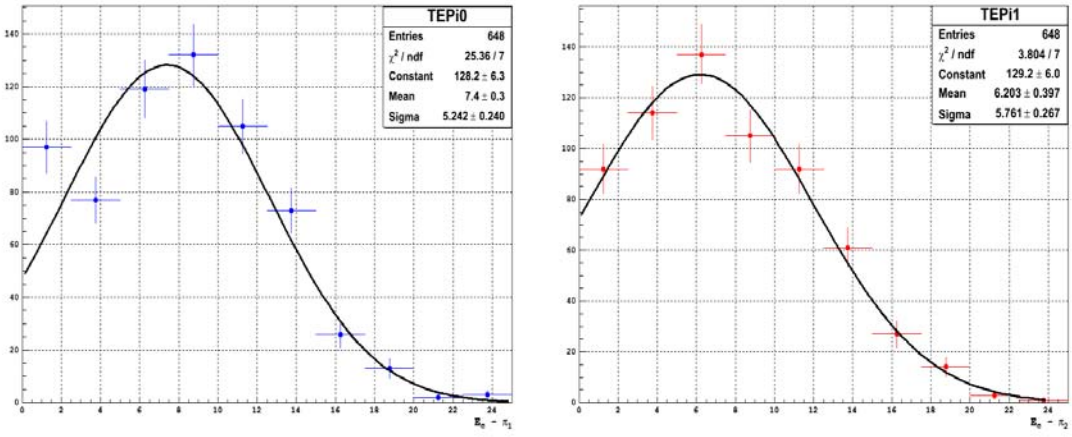

Fig. 6.9 Energy Subtracted for each pion form the calorimeter using digital mode with 98% threshold. The gaussian fit to the data is also shown.

6.6.3 Left-over Energy in the Calorimeter after Second Iteration

The leftover energy from the leftover hits is a measure of the performance of the algorithm. If the algorithm successfully subtracts the energy of the charged particle, the remainder of the energy should be negligible in this study, since only two charged pions were chosen for the study and no neutral particles are present. The leftover energy is shown in Fig. 6.10. The most probable value (MPV) of the Landau curve shows that the energy left over is 1.271 ± 0.072 GeV which is about 8.5% of the total energy of the two pions. The algorithm can be improved to perform better by considering the shower shape fluctuation. By varying the cone size on an event by event basis to subtract the energy, the algorithm may perform better. For this study, a fixed cone size is chosen.

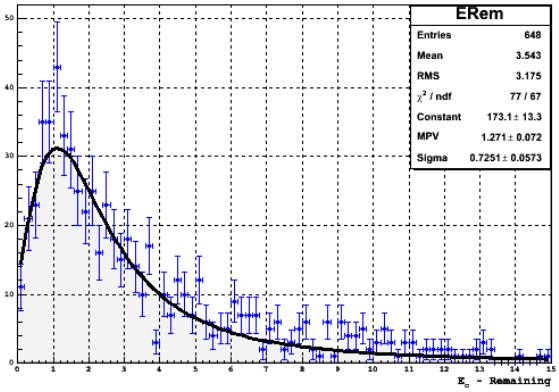

Fig. 6.10 The remainder of the energy after subtraction in the calorimeter is fit with a Landau curve.

The energy of the two clusters associated with the pions and the leftover energy are shown in the scatter plot in Figs. 6.11 (a), (b) and (c) respectively. Fig. 6.11 d) shows the number of highest-density cells associated with a pion in anti-correlation to the number of highest density cells associated with the other pion in Hcal. The total

number of highest density cells that are associated with either pion cannot exceed the maximum number of layers (forty layers) the calorimeter

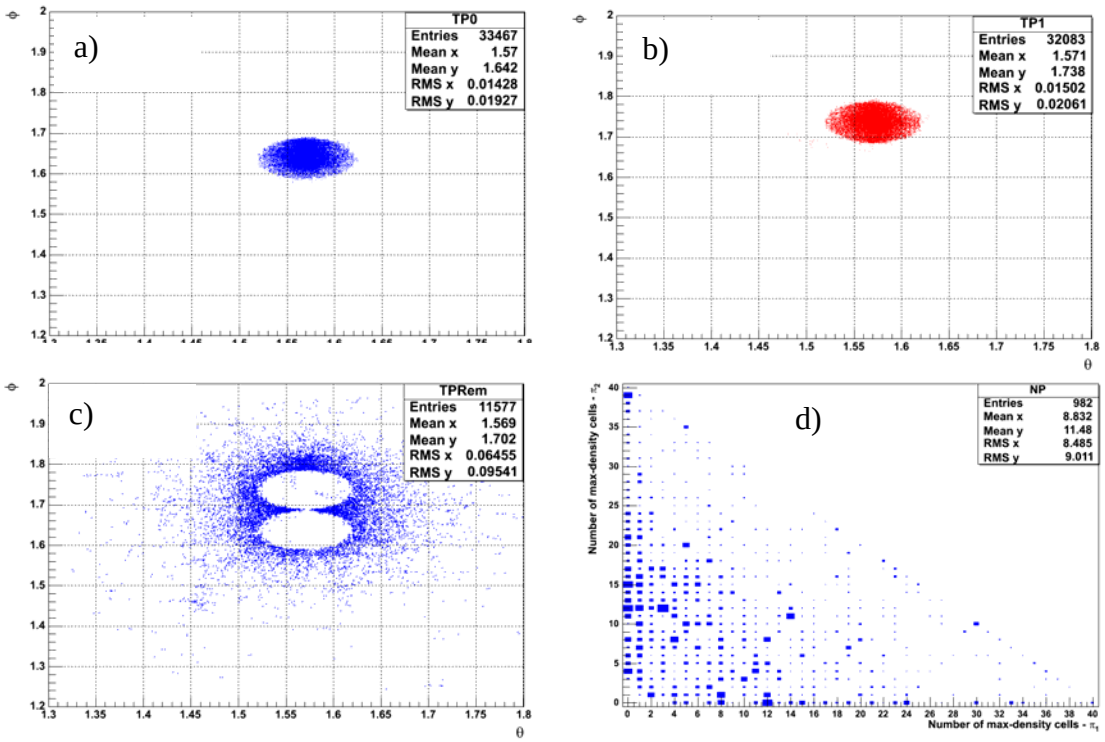

Fig 6.11 Energy Subtracted and the leftover energy is shown in a) b) and c). The anti-correlation between the highest-density cells associated with the pions in the first iteration is shown in d).

CHAPTER 7

CONCLUSIONS

This thesis presents the simulation studies of the performance of a digital hadron calorimeter using GEM and initial results in the development of the Energy Flow Algorithm. This thesis is a preliminary investigation and will provide a foundation for improvement of the algorithm and an efficient way to utilize it in tandem with digital calorimetric measurement to improve the energy resolution and to be able to achieve the physics goals of next generation linear colliders.

Detector simulation software is developed for the hadron calorimeter utilizing GEM as the sensitive gap. Calorimeter performance studies are performed using simulation data. The results are compared with other studies in analog and digital modes. The resolution in the analog mode is measured to be a bit worse than that of the TESLA-TDR [31] detector and other similar studies performed due to large Landau like fluctuation in the gas medium. The resolution in the digital technique is observed to be better than the analog version owing to the reduction of the high-end Landau fluctuations. The energy resolution in digital mode (with and without threshold) has the parameters comparable to TESLA-TDR and other similar studies. Application of threshold dramatically reduces noise in the readout. Several values of thresholds that span a wide range of mip efficiencies are chosen for digital studies. The resolution improves marginally by the application of the threshold since there is no electronic

noise in the simulation. However, increasing the threshold beyond a certain value results in the loss of information, and the resolution deteriorates. Table 7.1 summarizes the performance of the calorimeter and lists the energy resolution using various studies performed. Based on Table 7.1, it is suggested that a threshold of 98% be used for further digital studies, since the sampling term and the constant term are marginally better than those due to other thresholds.

Table 7.1 Fit parameters for Energy Resolution using Analog and Digital Method.

Detector Technology	Readout Method	Resolution $\sigma/E = A\%/\sqrt{E} + B\%$	
		(A ± ΔA)%	(B ± ΔB)%
TESLA TDR	Analog	36.26 ± 1.53	9.40 ± 0.33
GEM DHCAL	Analog	39.67 ± 1.53	3.78 ± 0.33
GEM DHCAL	Digital (100%)	75.36 ± 3.25	3.96 ± 0.54
GEM DHCAL	Digital (98%)	73.15 ± 5.68	4.91 ± 0.82
GEM DHCAL	Digital (95%)	75.63 ± 3.90	4.55 ± 0.65
GEM DHCAL	Digital (90%)	73.10 ± 4.83	4.73 ± 0.69
GEM DHCAL	Digital (85%)	74.57 ± 4.13	4.48 ± 0.61
GEM DHCAL	Digital (70%)	77.75 ± 5.01	5.20 ± 0.78

Energy Flow Algorithm is a solution for improving the jet energy resolution. Since it requires high granularity, digital technique is thought to be a solution for cost effectiveness. The initial results of track matching with calorimeter centroid using

Table 7.2 Comparison of $\Delta\theta$ and $\Delta\phi$ for different methods to determine centroid.

	Hits-weighted	Energy-weighted	Density-weighted
$\langle \Delta\theta \rangle$ (rad)	$(1.24 \pm 0.29) \times 10^{-3}$	$(4.38 \pm 0.20) \times 10^{-3}$	$(-7.55 \pm 0.38) \times 10^{-4}$
$\langle \Delta\phi \rangle$ (rad)	$(-2.93 \pm 0.57) \times 10^{-4}$	$(-6.34 \pm 0.86) \times 10^{-4}$	$(1.23 \pm 0.11) \times 10^{-4}$

single pion events are performed. The three methods explored and the study results are tabulated in Table 7.2. A preliminary result on the development of Energy Flow Algorithm to resolve two charged pions incident with half the average separation ($\Delta R = \sqrt{\Delta\theta^2 + \Delta\phi^2} \sim 0.12$) between two particles in typical jet events is carried out. The density-weighted method is used to identify the showers in the calorimeter and to determine the centroids, since this method shows the best track matching performance. The centroids are then extrapolated to the tracker, and track-cluster association is performed using $\Delta\theta$ and $\Delta\phi$ between the tracker and calorimeter as the parameters for comparison using single cone algorithm. The energy subtraction of typical pion showers is usable a level enough to replace the energy with the momentum of the charged track with some accuracy. The observation of the remainder of the energy after the subtraction shows that a small but non-negligible amount of energy is left over.

The future study can be aimed at understanding the remaining energy after subtraction, and determination of the extrapolated track from the tracking chamber taking into account the full magnetic field effects for better energy subtraction. Further study is needed to understand the shape of the showers in the calorimeter to develop a measure to arrive at the adequate amount of energy to be subtracted especially in the

case of overlapping showers, or complicated showering processes. For example, effects such as a single shower in the calorimeter with two matching tracks in the tracking chamber can be a tricky problem to resolve. Showers may overlap if a charged particle and neutral particle both deposit energy in the calorimeter with a close proximity. Association of the energy of charged particle for subtraction is a difficult task in this case because the neutral particles do not leave tracks in the tracking chamber. If particles start the showering process deeper in the calorimeter, they can manifest as a single shower. Measures such as the size of the energy cluster, unlike the simple cone, can be incorporated into the algorithm. There is room for improvement of the algorithm to make it more sophisticated, viable and realistic to reproduce consistent results. Dr. Hahn (a visiting professor) and Mr. Jacob Smith (a physics undergraduate student) are currently involved in development of EFA to sophisticate the algorithm.

APPENDIX A

SUBROUTINE TO CONVERT HEPEVT BINARY TO ASCII FORMAT

The FORTRAN subroutine that is used to represent an event in the HEPEvt format for use in detector simulation is listed in Fig. A.1. The FORTRAN subroutine converts the HEPEvt event structure into ASCII format. The input to the detector simulation is in ASCII format. In this format, the first line of each primary event is an integer, which represents the number of the following lines of primary particles. Each line in an event corresponds to a particle in the /HEPEVT/ common block. Each line has ISTHEP, IDHEP, JDAHEP(1), JDAHEP(2), PHEP(1), PHEP(2), PHEP(3), PHEP(5) where the meaning each variable is as follows:

ISTHEP: status code, with the following meanings:

= 0: null entry

=1: an existing entry, which has not decayed or fragmented. This is the main class of entries, which represents the 'final state' given by the event generator.

=2: an entry which has decayed or fragmented and is therefore not appearing in the final state, but is retained for event history information.

=3: a documentation line, defined separately from event history. This could include the two incoming reacting particles, etc.

=4-10: undefined, but reserved for future standards

IDHEP: particle identity, according to the Particle Data Group (PDG) standard.

JDAHEP(1): pointer to the position of the first daughter. If an entry has not decayed, this is zero.

JDAHEP(2): pointer to the position of last daughter. If an entry has not decayed, this is zero. It is assumed that the daughters are stored sequentially, so that the whole range (JDAHEP(1)-JDAHEP(2)) contains daughters.

PHEP(1): momentum in the x direction, GeV/c.

PHEP(2): momentum in the y direction, GeV/c.

PHEP(3): momentum in the z direction, GeV/c.

PHEP(4): energy, in GeV.

PHEP(5): mass, in GeV/c^2.

```
************************************************************
     SUBROUTINE HEP2G4
*
* Convert /HEPEVT/ event structure to an ASCII file
* to be fed by G4HEPEvtInterface
*
************************************************************
PARAMETER (NMXHEP=2000)
COMMON/HEPEVT/NEVHEP,NHEP,ISTHEP(NMXHEP),IDHEP(NMXHEP),
>JMOHEP(2,NMXHEP),JDAHEP(2,NMXHEP),PHEP(5,NMXHEP),VHEP(4,NMXHEP)
DOUBLE PRECISION PHEP,VHEP
*
WRITE(6,*) NHEP
DO IHEP=1,NHEP
WRITE(6,10)
                ISTHEP(IHEP),IDHEP(IHEP),JDAHEP(1,IHEP),JDAHEP(2,IHEP),
                PHEP(1,IHEP),PHEP(2,IHEP),PHEP(3,IHEP),PHEP(5,IHEP)
                        FORMAT(4I10,4(1X,D15.8))
ENDDO
*
RETURN
END
```

Fig. A.1 HEP2G4 Subroutine in Fortran represents an event in HEPEvt format

Table A.1 lists a few lines of an event represented in ASCII format, according to the HEPEvt standard.

Table A.1 Event listing for a few lines in an event in HEPEvt format.

315							
3	11	0	0	0.00000000E+00	0.00000000E+00	0.50000000E+03	0.00000000E+00
3	-11	0	0	0.00000000E+00	0.00000000E+00	-0.50000000E+03	0.00000000E+00
2	-5	51	51	0.15005162E+01	0.53383238E+02	0.19289955E+02	0.48000000E+01
2	21	51	51	0.10270549E+01	0.61677551E+01	0.25037135E+01	0.00000000E+00
1	2212	0	0	0.11488370E+01	0.75547861E+00	-0.40581867E+00	0.93827000E+00
1	-211	0	0	0.19901677E+00	0.77510907E-01	-0.78429871E+00	0.13957000E+00

APPENDIX B

GEM DENSITY CALCULATION AND REPLACING THE DETAILED GEM WITH SIMPLE GEM GEOMETRY

The simple-GEM replaces the detailed GEM and is a solid material that reproduces the properties of detailed GEM. For the purpose of implementation of simulation geometry using Mokka, it is necessary to measure the thickness of the simple-GEM and specify its density. Table B.1 lists the summary of the detailed GEM and the density of each material used. The densities of these materials are obtained from the atomic and nuclear properties of materials, which are listed in the Particle Data Group (PDG) Tables [59]. A cross sectional area of 1 mm^2 for all the materials in the sensitive gap is assumed in the calculations. A thickness of 3.1 mm is obtained for the solid material that replaces the detailed GEM. Therefore, the gas gap for the remainder of the sensitive gap is 3.4 mm, since the sensitive gap per layer is 6.5 mm. The density of simple-GEM is calculated to be 2.208 g/cm^3.

The simple-GEM geometry implementation is data driven at execution time. In this approach, the user is able to compose several detector models as sub detector subsets. The data for implementation of geometry is obatained from the geometry database, and a choice of several subdetector models is available. The database consists of the description of a detector model, the subdetector model and a relationship is established between them. At execution time, all the geometry drivers Mokka needs to build a given detector model are invoked. In the present study, the HcalFeRPC (consists of Iron absorber material and RPCs in the sensitive gap) subdetector model is chosen for the TESLA TDR detector model. Changes are made to the geometry driver and database to replace the sensitive gap with simple-GEM.

Table B.1 Summary of the properties of materials in the sensitive gap of a double GEM geometry and calculation of density of simple-GEM that replaces the detailed geometry.

Sl	Material	Density (g/cm^3)	Volume (mm^3)	# Layers	Mass X 10^{-3} (g)	Comment
1	*Copper*	*8.96*	*1 X 1 X 0.005*	*4*	*0.1792*	*Copper layers on Kapton*
2	*Copper*	*8.96*	*1 X 1 X 0.05*	*4*	*1.792*	*Copper layers on G10*
3	*G10*	*1.7*	*1 X 1 X 1.4*	*2*	*4.76*	*Two layers of G10*
4	*Kapton*	*1.42*	*1 X 1 X 0.04*	*2*	*0.1136*	*Double layers of Kapton*
	Total		*3.1*	*12*	*6.8448*	*Total Solid Material*
5	*ArCO2 gas (70:30)*	*1.84 X 10^{-3}*	*1 X 1 X 3.4*	*All gaps*	*0.92 X 10^{-3}*	*Gas volume*
				Total	*0.92 X 10^{-3}*	*Total Mass of Gas*

Density of Solid GEM layer : 6.8448 / 3.1 = 2.208 g/cc

APPENDIX C

THE EFFECTIVE NUCLEAR INTERACTION LENGTH OF A HCAL MODULE

The Hcal module consists of 40 layers of Iron as the absorber, (each 18 mm thick) and 40 layers of GEM sensitive material (each 6.5 mm thick). Therefore the total thickness of the Hcal module is given by Eq. C.1.

$$L = (18 + 6.5)\frac{mm}{layer} \times 40\ layers = 980\ mm \qquad \text{C.1}$$

The effective nuclear interaction length (λ_0) of a mixture can be calculated using Eq. C.2 and that of a compound using Eq. C.3.

$$\frac{1}{\lambda_0} = \sum_i \frac{V_i}{\lambda_i} \qquad \text{C.2}$$

$$\frac{1}{\lambda_0} = \sum_i \frac{m_i}{\lambda_i} \qquad \text{C.3}$$

V_i and m_i are the volume by fraction and mass by fraction of the *i*th component of the mixture and compound respectively. λ_i is the interaction length of the *i*th component. The composition in a layer of Hcal can be divided into three distinct categories each of which have an effective interaction length.

- Mixture of Argon and Carbon-dioxide in the ratio 70:30 by volume (l_1 =3.4 *mm*)
- The compound material of simple-GEM (l_2 = 3.1 *mm*)
- The Iron absorber material (l_3 = 18 *mm*)

The ratio of these substances by volume is 3.4/3.1/18 (mm) = 12.7/13.9/73.4 (%) assuming a cross section of 1 mm^2 for these materials.

The mass ratio of different materials of simple-GEM is as follows:

$Copper/Copper/G10/Kapton: 0.1792(2.62\%)/1.792(26.2\%)/4.76(69.54\%)/0.1136(1.62\%)$ [Refer Appendix B].

The atomic and nuclear properties of materials are listed in the Particle Data Group (PDG) tables [59]. The nuclear interaction length for these materials obtained from these tables are listed in Table C.1:

Table C.1 Density and Nuclear Interaction length of various materials in GEM

Material	Density (g/cm^3)	λ (g/cm^2)	λ (cm)
Copper (Cu)	8.96	134.9	15.1
Iron (Fe)	7.87	131.9	16.8
Kapton	1.42	85.8	60.4
G10	1.7	90.2	53.1
Ar (gas)	1.78 (g/l)	117.2	65.8
CO_2 (gas)	1.56 (g/l)	89.7	57.4

For the Ar-CO_2 Eq. C.4 gives mixture the effective interaction length.

$$\frac{1}{\lambda_1} = \frac{70}{65.8} + \frac{30}{57.4}\left(\frac{\%}{cm}\right) \qquad \text{C.4}$$
$$\lambda_1 = 63\,cm$$

For simple-GEM, the interaction length is given by Eq. C.5

$$\frac{1}{\lambda_2} = \frac{2.62}{15.1} + \frac{26.2}{15.1} + \frac{69.54}{53.1} + \frac{1.64}{60.4}\left(\frac{\%}{cm}\right) \qquad \text{C.5}$$
$$\lambda_2 = 30.8\,cm$$

For Iron absorber, the interaction length is given in Eq. C.6

$$\lambda_3 = 16.8\,cm \qquad \text{C.6}$$

Therefore, effective interaction length of one layer of Hcal is:

$$\frac{1}{\lambda_{eff}} = \frac{12.7}{30.8} + \frac{13.9}{63} + \frac{73.4}{16.8}\left(\frac{\%}{cm}\right) \qquad \text{C.7}$$

$$\lambda_{eff} = 20.0\,cm = 200\,mm$$

Therefore the Hcal module is (980/200) ~ 5 interaction lengths longitudinally.

APPENDIX D

ERROR CALCULATION FOR ENERGY RESOLUTION

$$\left(\frac{\sigma}{E}\right) = A \cdot \left(\frac{1}{\sqrt{E}}\right) + B$$

Let $Y = \frac{\sigma}{E}$ *and*

$$X = \frac{1}{\sqrt{E}}$$

$\therefore \quad Y = A \cdot X + B$

To find the error in X *and* Y*, consider*

$$\Delta Y = \Delta\left(\frac{\sigma}{E}\right)$$

$$= \Delta\sigma \oplus \Delta E$$

$$= \sqrt{\left(\frac{\partial Y}{\partial \sigma}\right)^2 (\Delta\sigma)^2 + \left(\frac{\partial Y}{\partial E}\right)^2 (\Delta E)^2} \quad (\because \sigma \text{ and } E \text{ are independent})$$

$$\frac{\partial Y}{\partial \sigma} = \frac{1}{E} \quad \text{and}$$

$$\frac{\partial Y}{\partial E} = -\frac{\sigma}{E^2}$$

$$\therefore \Delta Y = \sqrt{\left(\frac{1}{E}\right)^2 (\Delta\sigma)^2 + \left(-\frac{\sigma}{E^2}\right)^2 (\Delta E)^2}$$

$$= \left(\frac{\sigma}{E}\right) \cdot \sqrt{\left(\frac{\Delta\sigma}{\sigma}\right)^2 + \left(\frac{\Delta E}{E}\right)^2} \quad \text{which can also be written as}$$

$$\frac{\Delta Y}{Y} = \sqrt{\left(\frac{\Delta\sigma}{\sigma}\right)^2 + \left(\frac{\Delta E}{E}\right)^2}$$

Similarly

$$\Delta X = \Delta\left(\frac{1}{\sqrt{E}}\right)$$

$$= \left|\frac{\partial X}{\partial E} \cdot \Delta E\right|$$

$$\frac{\partial X}{\partial E} = \frac{1}{2 \cdot E \cdot \sqrt{E}}$$

$$\Delta X = \frac{1}{2 \cdot E \cdot \sqrt{E}} \cdot \Delta E$$

APPENDIX E
PLOTS FOR ENERGY RESPONSE AND RESOLUTION WITH 98% THRESHOLD

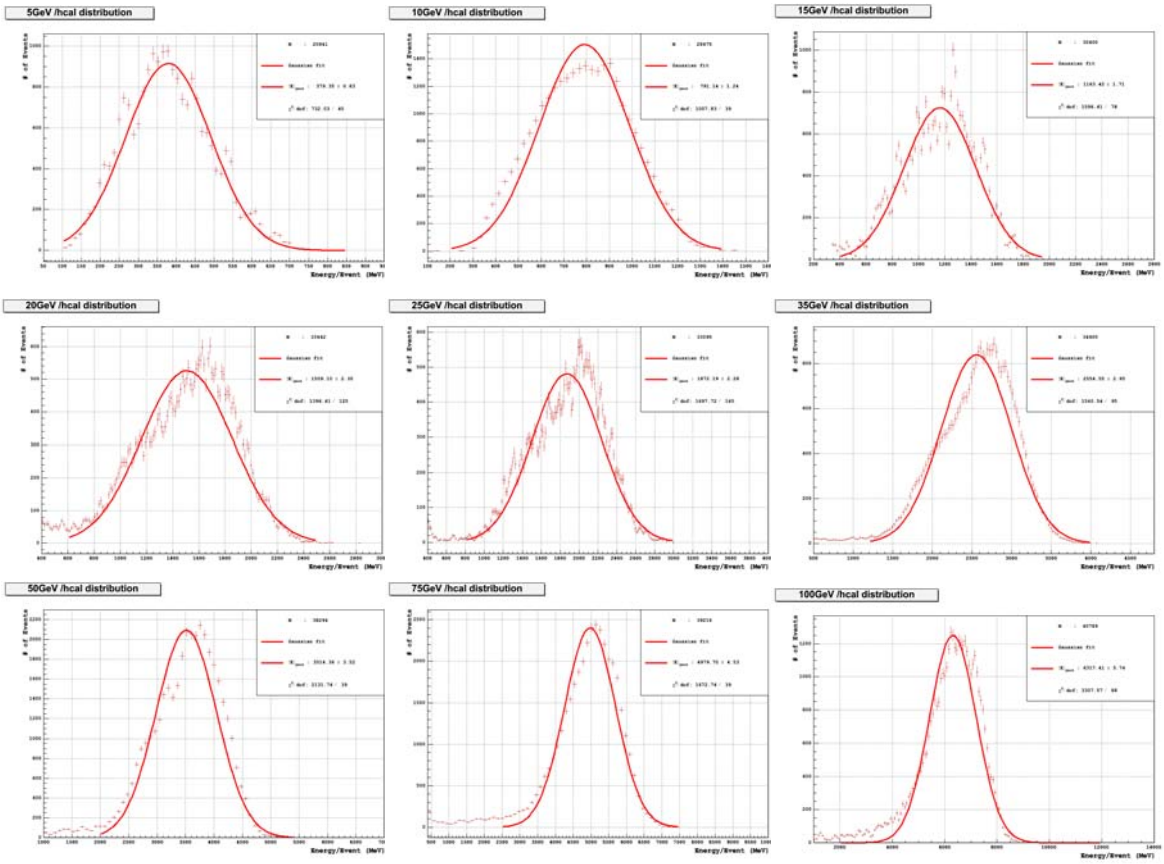

Fig. E.1 Hcal response for different values of incident energy in digital mode with 98% threshold. The data is fit with a gaussian.

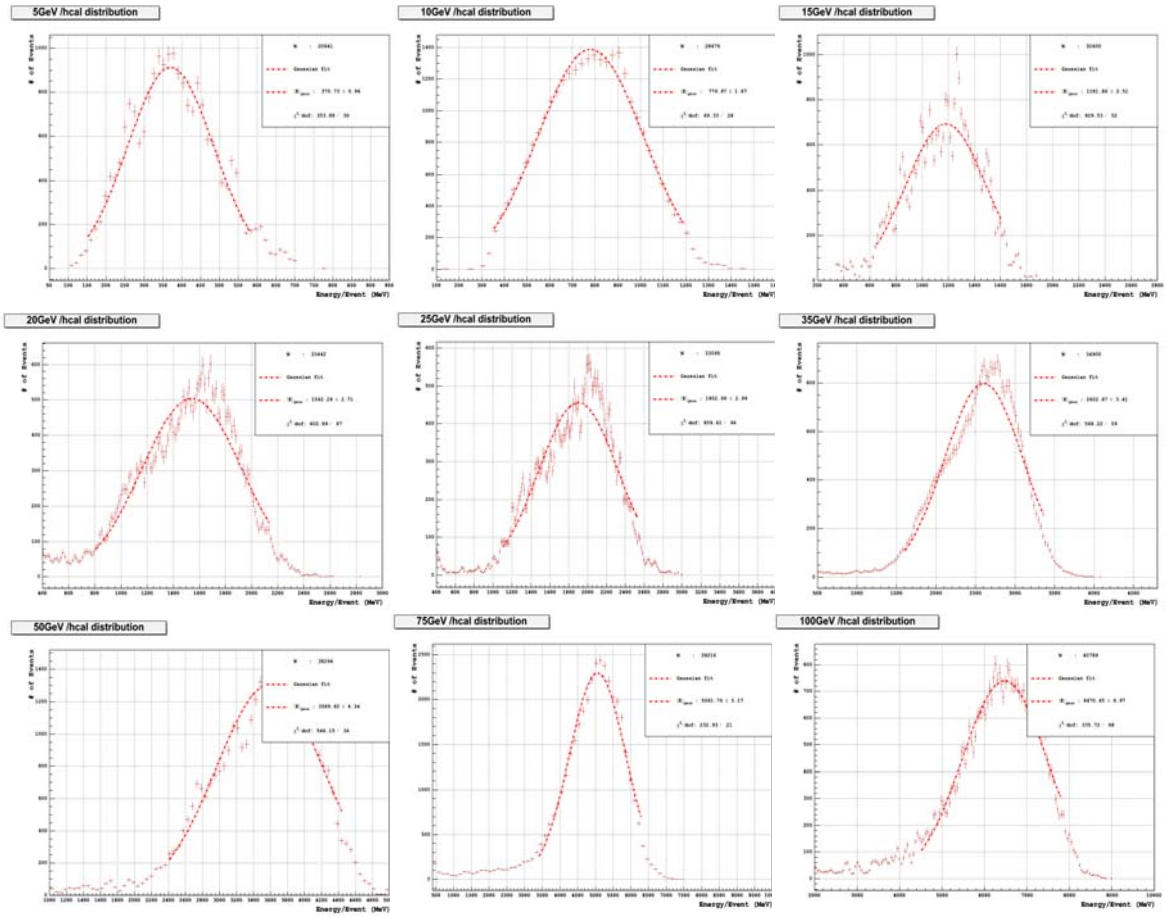

Fig. E.2 Hcal response with constrained gaussian fit to obtain the systematic errors for different values of incident energies.

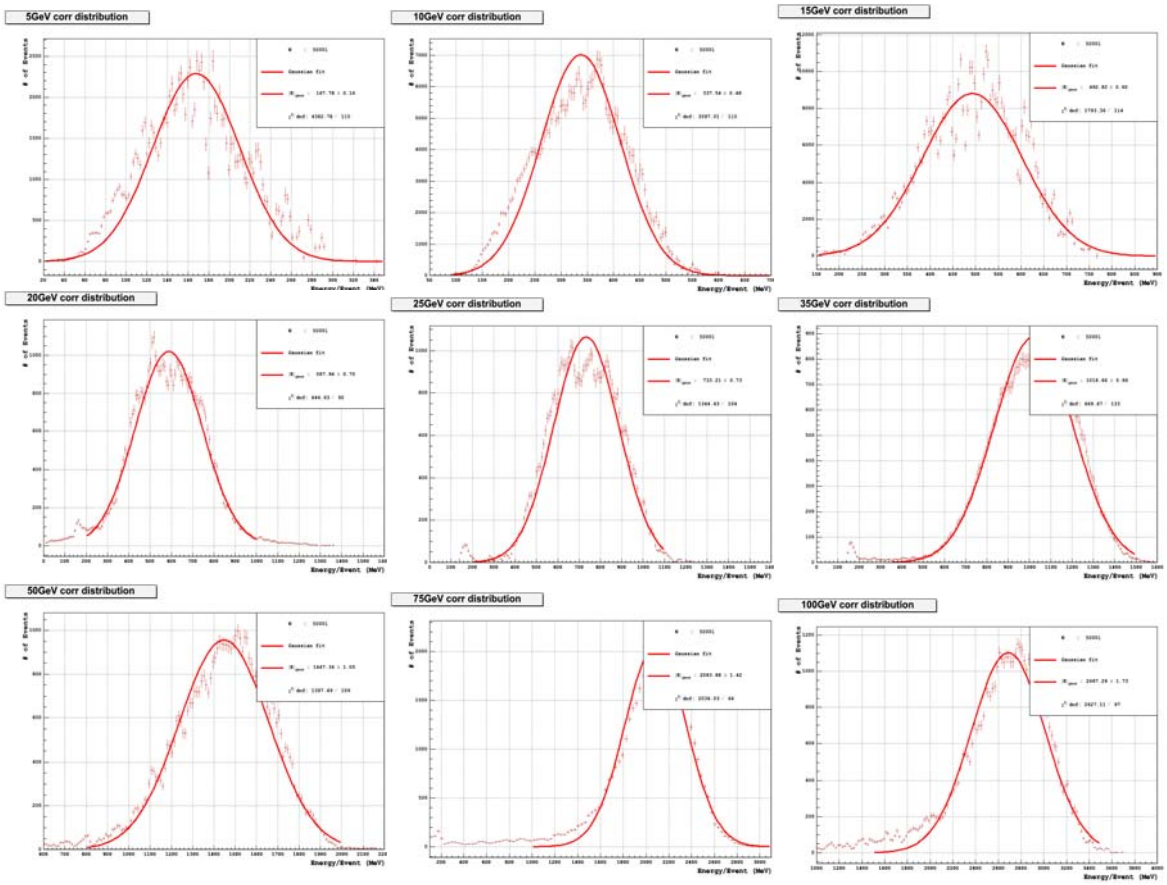

Fig. E.3 Total response to determine the weighting factor for different incident energies.

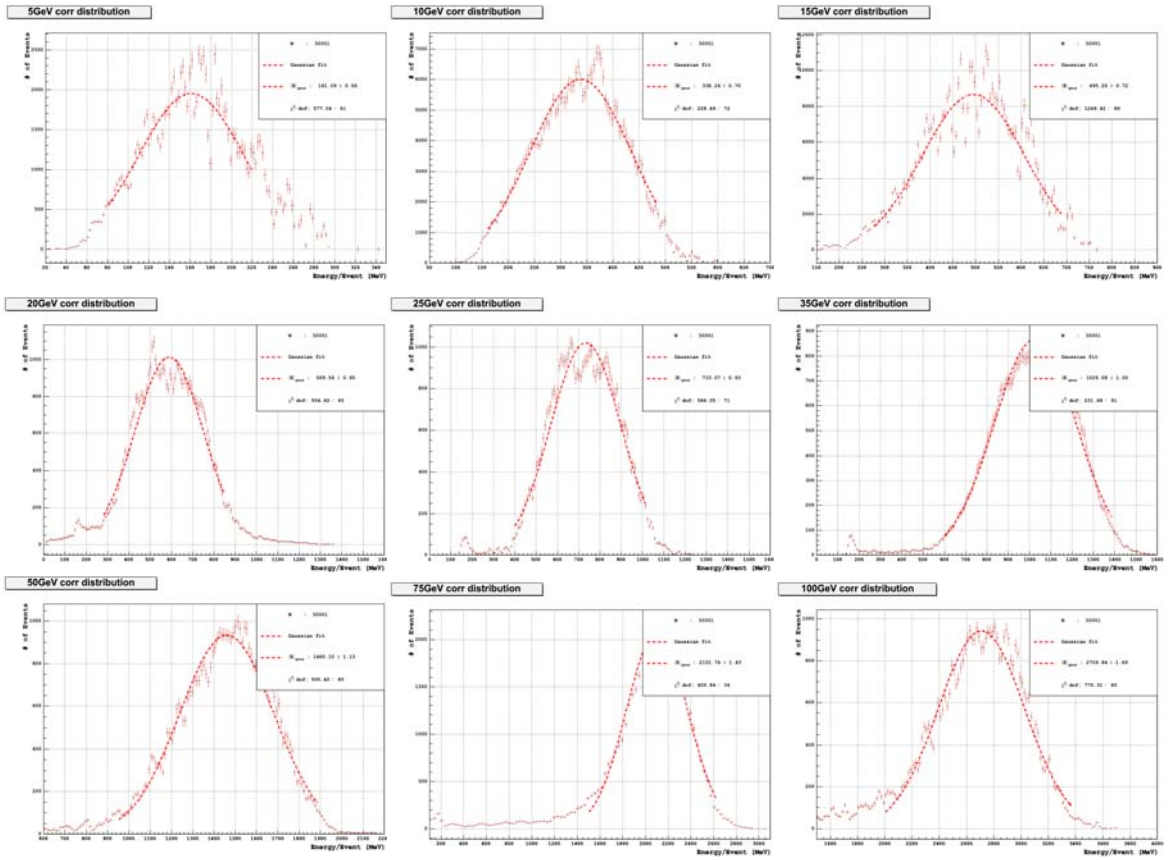

Fig. E.4 Total response with constrained gaussian fit to obtain systematic errors for energy response.

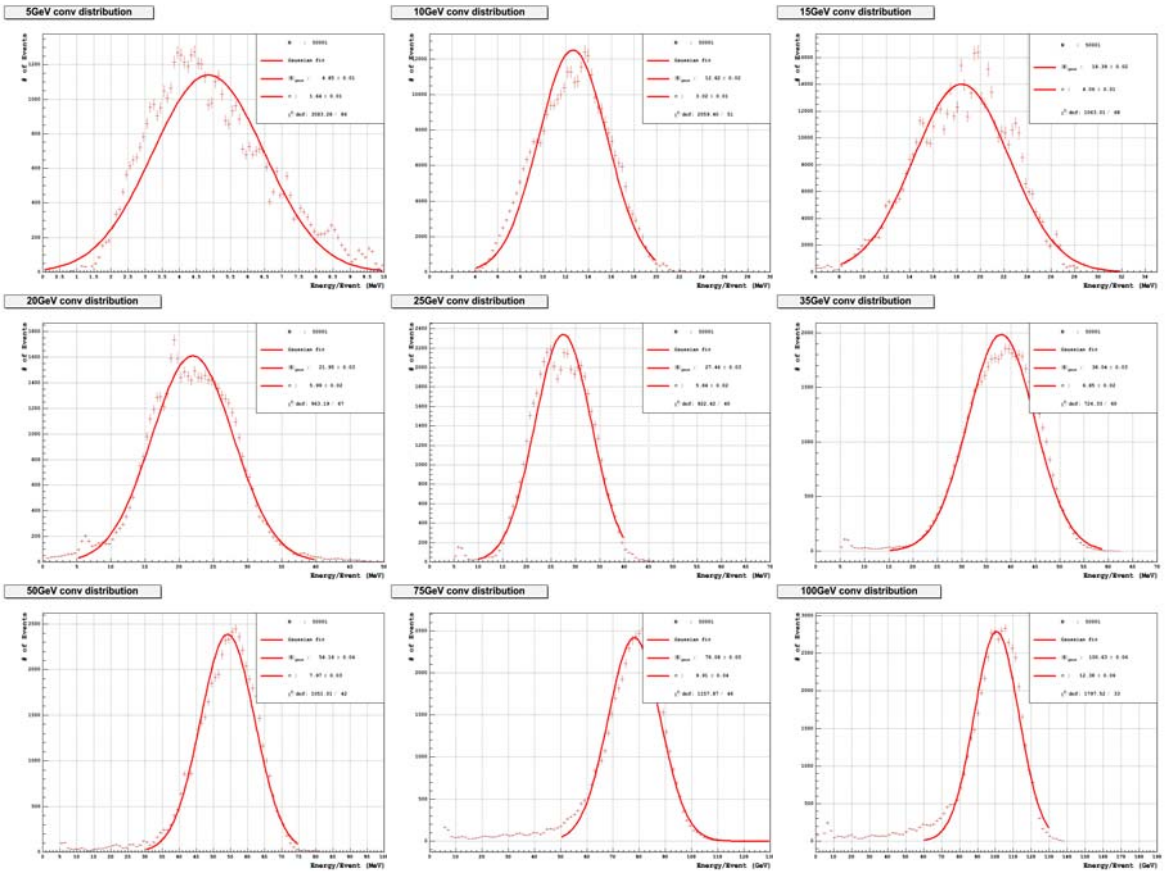

Fig. E.5 Converted energy after the sampling factor is applied to obtain resolution.

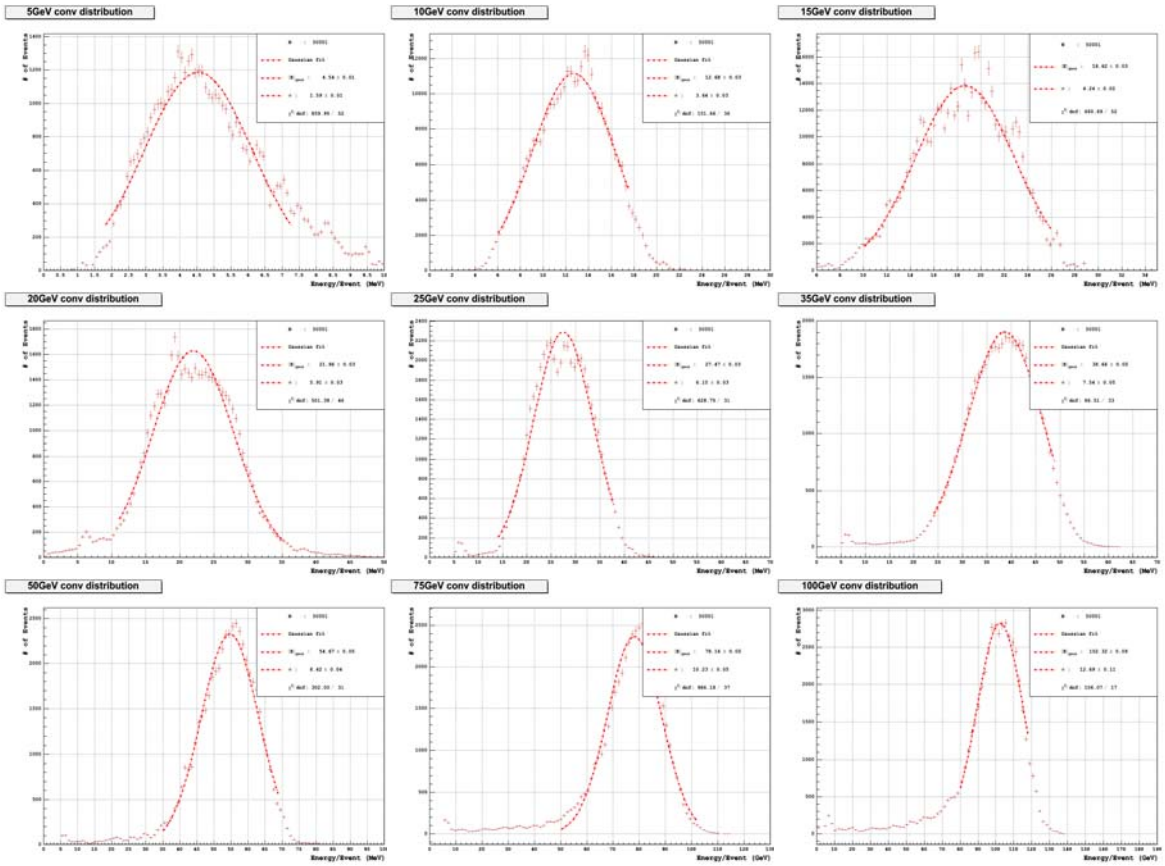

Fig. E.6 Converted energy with constrained gaussian fit to obtain systematic errors for energy resolution.

APPENDIX F
PROGRAM TO GENERATE EVENTS FOR EFA

The event generation is carried out using modified Pandora-Pythia event generator to generate ASCII output format as described in Appendix A.

The reaction that is of interest is shown in Fig F.1.

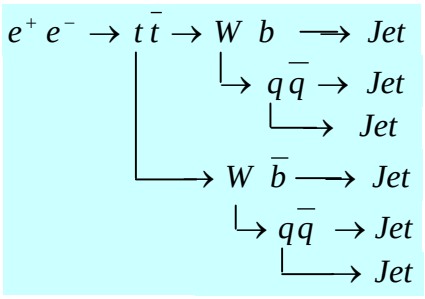

Fig. F.1 The six jet final state reaction.

In this reaction, the e^+e^- collides to form a $t\bar{t}$ pair, which decay into a pair of W (which decays into a pair of quarks) and b. Each quark then produces a jet after hadronization. Therefore there are six jets in the final state. To generate the final state of six jets, the program has to be modified. Fig. F.2 shows the program that is used to generate the above process. The event generator can be tuned to generate the desired final state. Some of the parameters can be set to generate a specific set of final states. Lines 2-8 define the input variables to the program. The input includes the number of events to be generated and the output file where the events in HEPEvt format are to be stored. Lines 10-12 define the properties of the two beams that collide. Lines 13-16 are used to initialize the beams. Lines 17-18 specify the sub process (eetottbar pr) and decay mode of the sub process (to generate quarks only). Lines 21-22 are used to specify the ASCII output format. Lines 23-26 initiate the Pythia generator and terminate it when done. The event generation leads to an output file that contains the four-momenta of particles and energy of particles that result in the hadronization, as described in section 2.2.1. The

status code corresponding to each of the particles in the given event is known. So for the analysis, the final state particles (with no daughters) are chosen in a given event and are analyzed as given in the following sub sections.

```
1.   int main(int argc, char* argv[]) {

2.   int   nEvent    = 0;
3.   char* outfile   = 0;
4.   int   iseed_pan = 1;  // default pandora initial seed

5.   if (!argv[1]) { printf(" Enter # events to be generated \n"); return 0; }
6.   nEvent  = atoi(argv[1]);
7.   if (argc > 2) outfile   = argv[2];
8.   if (argc > 3) iseed_pan = atoi(argv[3]); // Seed number should > 0

9.   /*    define the pandora event selection in this space     */

10.  double ECM  =  1000.; // Energy at Center of Mass
11.  double PolE =  0.0; // Polarization Electron
12.  double PolP =  0.0; // Polarization Positron

13.  ebeam b1(ECM/2.0, PolE, electron, electron);
14.  b1.setup(NLC500); // Define the electron beam and initialize it

15.  ebeam b2(ECM/2.0, PolP, positron, positron);
16.  b2.setup(NLC500); // Define the positron beam and initialize it

17.  eetottbar pr; // Process is ee to ttbar
18.  pr.onlyDecay(quarksOnly, quarksOnly); // Decay to quarks only

19.  pandora P(b1,b2,pr);
20.  pandorarun  PR(&P, nEvent, iseed_pan);

21.  int LUN = 20;
22.  PR.SetASCII(LUN); // Define ASCII output format

23.  PR.initialize(outfile);
24.  PR.getevents();
25.  PR.terminate();
26.  }
```

Fig. F.2 A Simple Pandora program. This program is used generate $e^+e^- \rightarrow t\bar{t} \rightarrow 6\,jets$ final state events.

The listing to generate the events using particle gun utility in Mokka is given in Fig. F.3. Line 1 defines the type of generator used (particle gun). Lines 2-5 indicate its position (0,0,0 mm, the center of the detector), the direction in which the gun is pointed (0, 1, 0 is the +Y direction), the energy of the particle (7.5 GeV) and its ID (π^-). Line 6 indicates the number of events to be generated (1000 events).

```
1. /generator/generator particleGun
2. /gun/position 0 0 0 mm
3. /gun/direction 0 1 0
4. /gun/energy 7.5 GeV
5. /gun/particle pi-
6. /run/beamOn 1000
```

Fig. F.3 Program to generate single pion events using Mokka.

REFERENCES

[1] C. N. Yang and T.D. Lee, *Phys. Rev.*, **96**:191 (1954)

[2] J. Arnaud, J. M. Boé, L. Chusseau, and F. Philippe, *Am. J. Phys.*, **67**:215-221 (1999)

[3] E. Fermi, *Z. Phys.*, **88**:161 (1934)

[4] S. Glashow, *Nucl. Phys.*, **22**:579 (1961)

S. Weinberg, *Phys. Lett.*, **12**:132 (1967)

A. Salaam, *Elementary Particle Physics, N. Svartholm ed.*, 367, (1968)

[5] F. J. Hasert *et.al. Phys. Lett.*, **46B**:138 (1973)

[6] F. J. Hasert *et.al. Nucl. Phys.*, **B73**:1 (1974)

[7] G. Arnison *et.al. Phys. Lett.*, **122B**:103 (1983)

[8] M. Banner *et.al. Phys. Lett.*, **122B**:476 (1983)

[9] G. Arnison *et.al. Phys. Lett.*, **126B**:398 (1983)

[10] P. Bagnaia *et.al. Phys. Lett.*, **129B**:130 (1983)

[11] M.C. Crowley-Milling, *Rep. Prog. Phys.*, 46:51 **(**1983)

[12] FNAL Public pages (2003)
Web: http://www.fnal.gov/pub/inquiring/physics/accelerators/00-635D.jpg
Search: “Accelerator pictures at FNAL”

[13] Report of the Linear Collider Technical Review Committee report (2003)
Web: http://www.slac.stanford.edu/xorg/ilc-trc/2002/2002/report/03rep.htm
Search: “Linear Collider Report”

[14] F. Mandl and G. Shaw, *Quantum field theory*, John Wiley & Sons. (1984)

[15] F. James, *Rep. Prog. Phys.*, **43**:1145 (1980)

[16] T. Sjöstrand, *et. al., Pythia 6.2., Physics and Manual*, [arXiv:hep-ph/0108264] LU TP 01-21 (Second ed.,) (2002)

[17] GEometry ANd Tracking (GEANT)
S. Agostinelli *et. al., Nucl. Instr. Meth.,* A506:250-303 (2003)
Web: http://wwwasd.web.cern.ch/wwwasd/geant4/geant4.html
Search: "Geant4 home page"

[18] WWW Interactive Remote Event Display (WIRED)
Web: http://www.slac.stanford.edu/BFROOT/www/Computing/Graphics/Wired/
http://wired.freehep.org/
Search: "WIRED, event display, SLAC"

[19] Drawer for Academic WritiNgs, (DAWN), a PostScript Renderer
Web: http://geant4.kek.jp/~tanaka/
Search: "DAWN renderer"

[20] R. Brun, *et. al., ROOT- An Object Oriented Data Analysis Framework*. (1997)
Web: http://root.cern.ch
Search: "ROOT analysis"

[21] T. Johnson., *et. al., Java Analysis Studio*., SLAC, Stanford (2002)
Web: http://jas.freehep.org/
Search: "Java Analysis Studio"

[22] T. Ohl, *Comput. Phys. Commun.*, **101**, 269 (1997) [arXiv:hep-ph/9607454]

[23] G. Corcella *et al.*, JHEP **0101**:010 (2001) [arXiv:hep-ph/0011363]

[24] S.Jadach *et al.*, TAUOLA: *Comput. Phys. Commun.*, **76:**361 (1993)

[25] M. Iwasaki., Event Generation for Linear Collider Physics., (2002)

[26] T. Sjöstrand *et. al., 'Z Physics at LEP 1',* **3**:143 (CERN 89-08 Geneva) (1989)

[27] Geant4 Users guide for Application Developers, see *G4HEPEvtInterface*
Web:
http://geant4.web.cern.ch/geant4/G4UsersDocuments/UsersGuides/ForApplicationDeveloper/html/Fundamentals/eventGenerator.html
Search: "Geant4 Users guide"

[28] Pandora-Pythia Manual Online
Web:
http://wwwldnt.slac.stanford.edu/nld/new/Docs/Generators/PANDORA_PYTHIA.htm

Search: “Pandora Pythia”

[29] H. Videau *et. al., Mokka – A detailed simulation of a detector for the Next Linear Collider*., (2001)
Web: http://polywww.in2p3.fr/geant4/tesla/www/mokka/mokka.html#design
Search: “Mokka detector simulation”

[30] TESLA – The International Linear Collider and X-ray Laser Project
Web: http://tesla.desy.de/
Search: “TESLA project”

[31] T. Behnke *et al., TESLA - Technical Design Report* (2001)
Web: http://tesla.desy.de/new_pages/TDR_CD/PartIV/detect.html
Search: “TESLA Technical Design Report”

[32] C. Fabjan, T. Ludlam, *Ann. Rev. Nucl. Part. Sci.,* **32**:335-389 (1982)

[33] D. Acosta *et al. Nucl. Instr. Meth.,* **A320**:128 (1992)

[34] B. Rossi, *High-Energy Particles* (Englewood Cliffs, N.J: Prentice Hall) (1952)

[35] J. A. Bakken *et al. Nucl. Instr. Meth.,* **A254**:535 (1987)

[36] A. Anderson *et al. Nucl. Instr. Meth.,* **A290**:95 (1990)

[37] T. Akesson *et al. Nucl. Instr. Meth.,* **A262**:243 (1987)

[38] E. Bernardi *et al. Nucl. Instr. Meth.,* **A262**:229 (1987)

[39] K. Pinkau, *Phys. Rev.,* **139B**:1548 (1965)

[40] R. Wigmans, *Nucl. Instr. Meth.,* **A259**:389 (1987)

[41] R. Wigmans, *Calorimetry, Energy Measurement in Particle Physics,* (Clarendon Press: Oxford ed.,) (2000)

[42] C.W. Fabjan, *Experimental Techniques in Nuclear and Particle Physics,* T. (Ferbel ed., World Scientific) (1991)

[43] J.E. Brau, *Hadron calorimetry - Optimizing performance, in: Calorimetry in High Energy Physics, International Conference at Fermilab Oct. 1990,* proceedings edited by D.F. Andersen *et al.,* World Scientific (1990)

[44] R. Wigmans, *Ann. Rev. Nucl. Part. Sci.,* **41**:133 (1991)

[45] F. Sauli, *Nucl. Instrum. and Meth.,* **A386**:531 (1997)

[46] S. Habib, *Simulation Studies of a New Digital Hadron Calorimeter, Using Gas Electron Multipliers (GEM),* MS Thesis, (UTA-HEP/LC0001) (2003)

[47] A. von Engel, *Ionized Gases,* London:Oxford (1955)

[48] V. Davidenko *et. al., Nucl. Instr. Meth.,* **67**:325-30 (1969)

[49] P. Rice-Evans, *Spark, Streamer, Proportional, and Drift Chambers,* London: Richelieu, (1974)

[50] H. Videau et. K_L^0 Analysis, Presented at Santa Cruz LCRD Workshop (2002)
Web: http://www.slac.stanford.edu/xorg/lcd/calorimeter/talks/SCruz02/videau.ppt
Search: "K long Analysis using Mokka"

[51] S. R. Magill. *Comparison of Simulated Analog Versus Digital Energy Measurement in a Finely-Segmented Hadron Calorimeter, ANL,* (2003)

[52] D. Buskulic *et al. Nucl. Instr. Meth.,* **A360**:481-506, (1995)

[53] J. C. Brient, H. Videau, *The American Research on LC Calorimetry* hep-ex/0202004 (2004)

[54] W. Bartel *et. al., Phys. Lett.,* **B213**:235 (1988)

[55] W. Braunschweig *et.al., Phys. Lett.,* **214B**:286 (1988)

[56] S. Catani *et. al., Phys. Lett.,* **B269**:432 (1991)

[57] T. A. Gabriel. *et. al., Nucl. Instr. Meth.,* **A338**:336 (1994)

[58] Tesla Technical Design Report
Web: http://tesla.desy.de/new_pages/TDR_CD/PartIV/partIV.pdf
Search: "TESLA – TDR"

[59] D. E. Groom, *Atomic and Nuclear Properties of Materials,* LBNL (2000)
Web: http://pdg.lbl.gov/2000/atomicrppbook.pdf
http://pdg.lbl.gov/AtomicNuclearProperties
Search: "Atomic and nuclear properties LBNL"

[60] Dr. Mark Sosebee, Private Communications (2002-04)

[61] Mr. Barry Spurlock, Private Communications (2002-04)

[62] Ms. Shahnoor Habib, Private Communications (2002-04)

BIOGRAPHICAL INFORMATION

Venkatesh Kaushik obtained his bachelors degree with honors in mechanical engineering in 1998 from Bangalore University, India. In 1999, he came to the University of Texas at Arlington, USA to pursue his master's degree in computer science and engineering, which he completed successfully in 2002. He obtained his master's degree in Physics in 2004. His research interests include calorimetry for future linear colliders, energy flow algorithm development and Higgs searches in the field of high energy physics. He is currently pursuing his doctoral program in Physics.